

Combined spectroscopic and electronic transport characterization of doped graphene

I n a u g u r a l - D i s s e r t a t i o n

zur

Erlangung des Doktorgrades

der Mathematisch-Naturwissenschaftlichen Fakultät

der Universität zu Köln

vorgelegt von

Herr Dipl.-Phys. Martin Gordon Hell

aus

Rosenheim

Köln, 2019

Berichterstatter: Prof. Dr. Alexander Grüneis

Prof. Dr. Klas Linfors

Vorsitzender: Prof. Dr. Achim Rosch

Tag der letzten mündlichen Prüfung: 15.07.2019

For my family

Contents

	Page
1 Introduction	1
1.1 Purpose of this thesis	1
1.2 Experimental setup	3
1.3 Electronic structure of graphene	6
1.4 Photoemission spectroscopy	12
1.5 Raman spectroscopy	15
1.6 Transport properties of graphene	19
2 Publications	21
2.1 Resonance Raman spectrum of doped epitaxial graphene at the Lifshitz transition	21
2.2 Origin of the flat band in heavily Cs doped graphene	34
2.3 Combined ultra high vacuum Raman and electronic transport characterization of large-area graphene on SiO ₂	72
3 Further publications	79
3.1 Facile preparation of au(111)/mica substrates for high-quality graphene nanoribbon synthesis	79
3.2 Semiconductor-to-Metal Transition and Quasiparticle Renormal- ization in Doped Graphene Nanoribbons	84
4 Bibliography	I
5 Abstract	V
6 Zusammenfassung	VII

7	Own contributions to publications	IX
8	Selbständigkeitserklärung	XI

Chapter 1

Introduction

1.1 Purpose of this thesis

The spectroscopic and electronic characterization of air-sensitive two-dimensional materials is a scientific and technical challenging task. This thesis is motivated by the investigation of the Raman response of heavily doped graphene using a ultra-high vacuum (UHV) Raman spectrometer in tandem with the characterization of the graphene band structure if the Fermi level approaches the saddle point of the van Hove singularity using photoemission spectroscopy. A further motivation is the electronic characterization of pristine and doped graphene. This required the realization of an experimental setup for electronic transport measurements in ultra-high vacuum, which is shown in this thesis. We started to dope epitaxially grown graphene on Ir(111) with Cs and combined in-situ Raman spectroscopy in tandem with angle-resolved photoemission spectroscopy (ARPES) to describe the modification of the electronic band structure. By analyzing the evolution of the doping-dependent Raman spectrum from pristine epitaxially grown graphene to a heavily Cs doped state, we were able to establish a fully experimental relation between the energy shift and Fano [4] asymmetry parameter of the Raman G band versus carrier concentration obtained by ARPES[Chapter 2.1]. The energy shift could be explained by the effects of phonon renormalization due to the removal of the Kohn anomaly [5] and the lattice expansion [6], resulting in a phonon upshift and downshift respectively.

Further doping led to a new technique for inducing a flat band in the band

structure of graphene by sandwiching a graphene monolayer in between two alkali metal (Cs) layers. The obtained trilayer system was investigated by ARPES and we could explain the origin of the doping induced flat band at the M point of the Brillouin zone by zone folding and hybridization of the graphene bands with partially filled alkali metal bands[Chapter 2.2].

The characterization by in-situ transport measurements required the transfer of graphene from an Iridium single crystal to SiO₂. Therefore a water promoted transfer technique [7] was applied for the first time to graphene on Ir(111) and an in-situ transport setup was constructed. The highly sensitive transport measurements in combination with Raman spectroscopy led to a comprehensive characterization of transferred graphene from a pristine to a highly doped state. The existing measurement system paves the way for detailed in-situ characterization of air-sensitive materials by electronic transport under UHV conditions and low temperatures.

1.2 Experimental setup

Figure 1.2 depicts a schematic drawing of the setup, combining in-situ Raman spectroscopy and transport measurements at ultra-high vacuum (UHV) conditions. It consists of a preparation chamber where samples can be prepared or functionalized chemically and an analytical chamber in which Raman spectroscopy and transport measurements are performed..

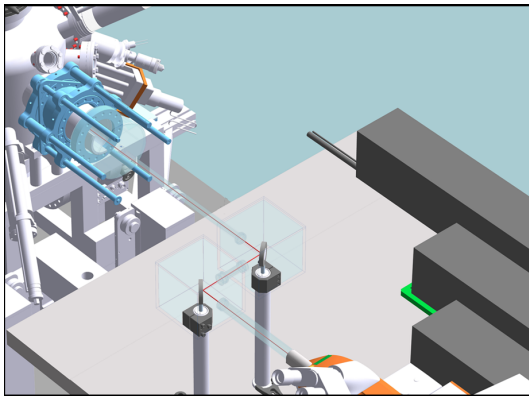
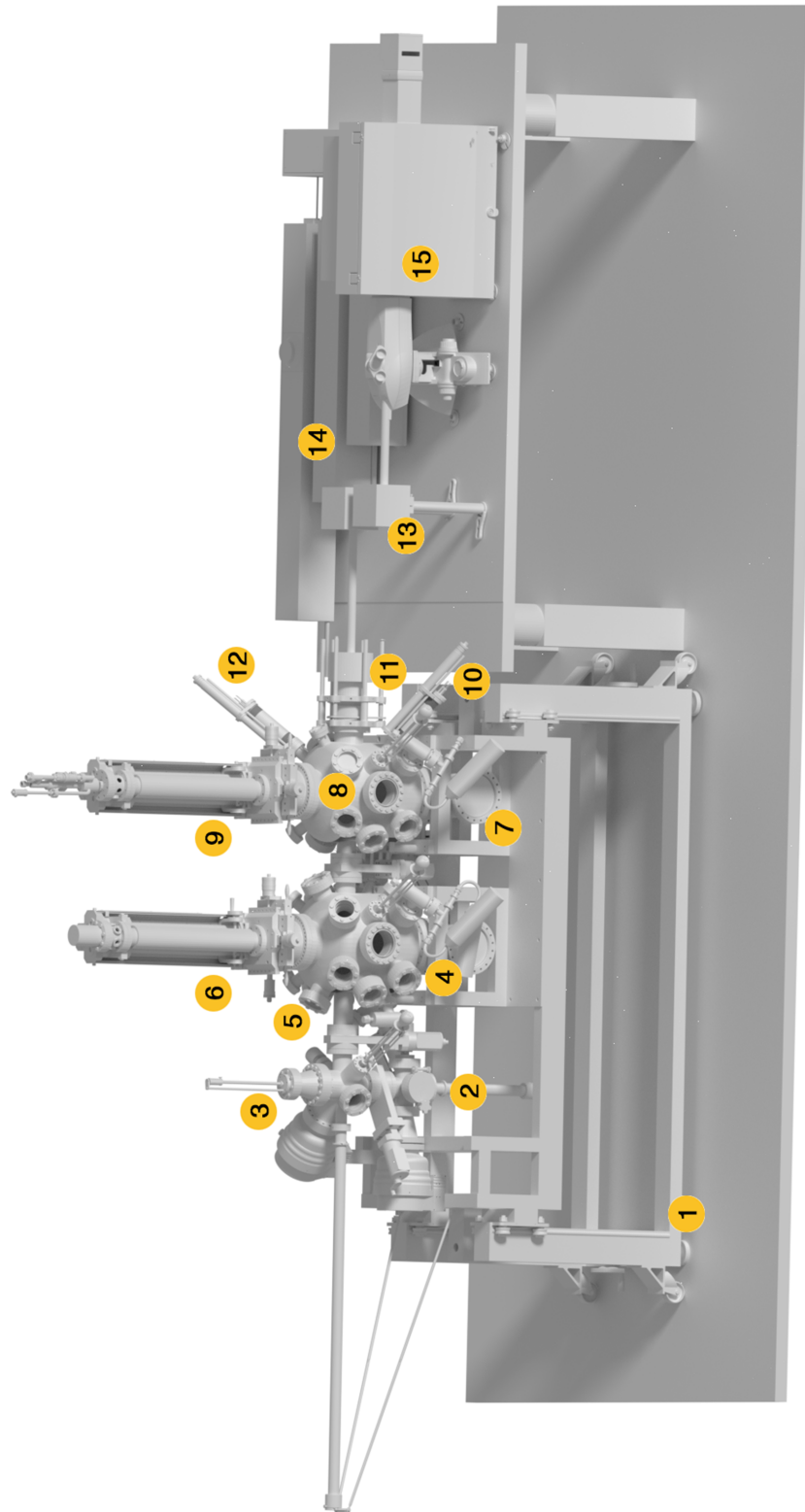


Figure 1.1: Laser path between the Raman spectrometer and the UHV system with an acrylic glass casing to decouple the laser path from the environment.

The spectrometer is a customized Renishaw inViaTM system with four lasers of different wavelength (332, 442, 532 and 633 nm). The collimated light from the spectrometer is directly coupled onto the sample in the chamber and allows a characterization without exposing samples to air. The laser path is separated from the environment by an argon flooded acrylic glass casing (Figure 1.1) with a laser beam focused on to the sample by a microscope objective in a specially designed optical flange on the chamber. Two actuators on the manipulator regulate the precise motion of the sample along two axes. This allows the detection of small samples in combination with a camera and the option to measure Raman maps with a spatial resolution of the Raman system of $4\mu m$. The UHV system is supported by a frame on air loaded anti-shock pads and provides a load lock for inserting samples, a storage, a preparation chamber with different gas lines, evaporators and a LEED analyzer. This is followed by an analytical chamber to measure the synthesized samples under low temperatures without any exposure to ambient conditions. A liquid helium cryostat allows permanent cooling to 4 K, a quartz crystal microbalance and linear transfer devices for alkali metal getters and other substrate evaporators for a functionalization of the measured materials round off the setup.



1. Air suspension, 2. Load lock, 3. Storage, 4. Gas lines, 5. LEED(backside), 6. Manipulator, 7. Turbo molecular pumps, 8. Analytical chamber, 9. LHe-cryostat, 10. Quartz crystal microbalance, 11. Raman objective, 12. Getters, 13. Argon gas line, 14. Lasers, 15. Raman spectrometer

Figure 1.2: Complete measurement setup with the UHV system and Raman spectrometer.

The average pressure in the chambers is in the range of $\approx 2 \times 10^{10}$ mbar produced by a serial connection of turbo molecular and membrane pumps.

To perform electrical transport measurements in UHV a home-made sample carrier with a corresponding sample receptor, shown in Figure 1.3, was designed and constructed. Commercial molybdenum sample plates can be additionally equipped with five Au covered and spring loaded pin connectors, held by a teflon block to have stable electric contacts from the sample to the sample receptor on the cryostat. The samples can be contacted by using five $50\ \mu\text{m}$ thick Au wires, glued by Ag paste to the spring pin connectors. The quantity

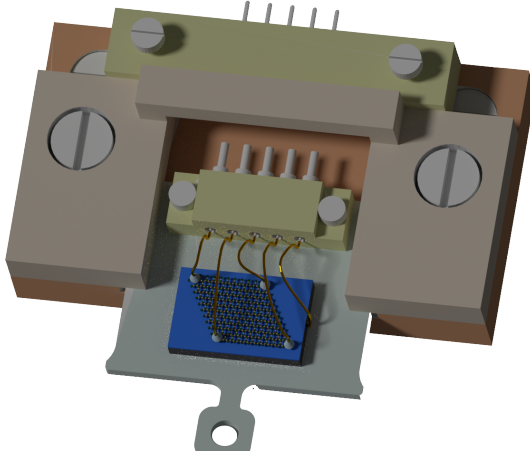


Figure 1.3: CAD drawing of the sample carrier with the corresponding sample receptor for electric transport measurements.

of the connectors was chosen by the motivation to measure 4-point resistance with a further opportunity to gate the samples at the same time. The corresponding sample receptor, permanently attached to the cryostat, was made of CuBe to ensure a high thermal conductivity. Au covered nail pins, embedded in a teflon block, act as a counterpart for the spring pin connectors on the sample plate. When the sample carrier is pushed into the receptor, the compressed spring connectors present a reliable method for transport measurements even under UHV conditions. Two screws additionally press the sample plate onto the sample holder, to stabilize the latter and increase the thermal contact to the cryostat. Au wires lead from the receptor to an electric feedthrough on top of the cryostat and various multimeters in combination with a lock-in amplifier complete the setup.

1.3 Electronic structure of graphene

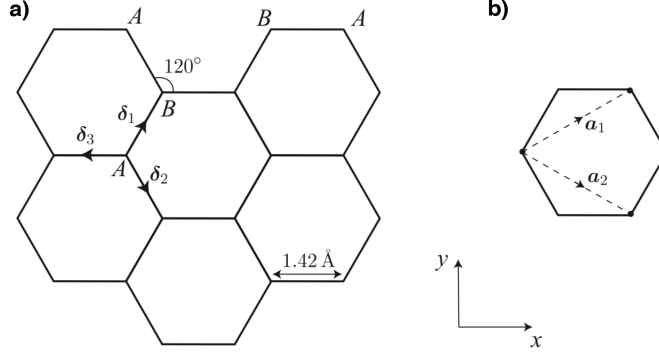


Figure 1.4: a) Graphene lattice with carbon atoms A and B, nearest neighbor distance vectors δ_{1-3} , a_{cc} as the distance between two carbon atoms and the corresponding primitive lattice vectors $\mathbf{a}_1, \mathbf{a}_2$.

The electronic structure of an isolated carbon atom is given by: $(1s)^2(2s)^2(2p)^2$. The 2s and 2p electrons can hybridize and form a tetrahedral structure with four sp^3 orbitals, formally known as diamond, which is a very good insulator (band gap $\approx 5 \text{ eV}$). An alternative possibility is to form three sp^2 orbitals, leaving over a more or less pure p-orbital. Here the natural tendency for the sp^2 orbitals is to arrange in a plane at 120° angles, giving a lattice in a honeycomb pattern shape named graphene. The structure of graphene is not a Bravais lattice but it can be seen as a triangular lattice with two atoms per unit cell. This lattice consists of two inequivalent sublattices A and B, shown in Figure 1.4, with the environments of the corresponding atoms being mirror images of one another. The corresponding primitive lattice vectors $\mathbf{a}_1, \mathbf{a}_2$ can be written as:

$$\mathbf{a}_1 = \frac{a_{cc}}{2} (3, \sqrt{3}), \quad \mathbf{a}_2 = \frac{a_{cc}}{2} (3, -\sqrt{3}) \quad (1.1)$$

where a_{cc} is the nearest-neighbor carbon-carbon distance ($\approx 1.42 \text{ \AA}$). The reciprocal lattice vectors $\mathbf{b}_1, \mathbf{b}_2$ defined by the condition $\mathbf{a}_i \cdot \mathbf{b}_j = 2\pi\delta_{ij}$ are then

$$\mathbf{b}_1 = \frac{2\pi}{3a_{cc}} (1, \sqrt{3}), \quad \mathbf{b}_2 = \frac{2\pi}{3a_{cc}} (1, -\sqrt{3}). \quad (1.2)$$

The first Brillouin zone (BZ) of the reciprocal lattice is defined by the planes bisecting the vectors to the nearest reciprocal lattice points. This gives the first Brillouin zone (FBZ) of the same form as the original hexagons of the honeycomb lattice, but rotated by $\pi/2$. The six points at the corners of the

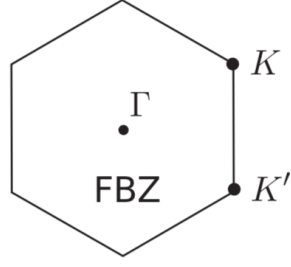


Figure 1.5: First Brillouin zone with the high symmetry points \mathbf{K} and \mathbf{K}' at the corners and the Γ -point in the center.

FBZ form two groups of three which are equivalent. Therefore there is only need to consider two equivalent corners labeled \mathbf{K} and \mathbf{K}' . Their positions in momentum space are given by

$$\mathbf{K} = \frac{2\pi}{3a_{cc}} \left(1, \frac{1}{\sqrt{3}} \right), \quad \mathbf{K}' = \frac{2\pi}{3a_{cc}} \left(1, -\frac{1}{\sqrt{3}} \right). \quad (1.3)$$

For an A-sublattice atom the three nearest-neighbor vectors in real space are given by

$$\delta_1 = \frac{a_{cc}}{2} (1, \sqrt{3}), \quad \delta_2 = \frac{a_{cc}}{2} (1, -\sqrt{3}), \quad \delta_3 = -a_{cc}(1, 0) \quad (1.4)$$

while those for the B-sublattice are the negatives of these.

Tight-binding

The electronic band structure can be described with a tight-binding model that uses either *ab-initio* calculation parameters [Grneis2008] or is fit to experimental values [Grneis2009]. The graphene unit cell has two carbon atoms where each consists of one $1s$, one $2s$ and three $2p$ orbitals, yielding to ten atomic orbitals all together. The $1s$ level is found 285 eV below the vacuum level and is not considered to contribute to the electronic properties. Six of the remaining eight orbitals form the high energetic in-plane σ bonds turning into six bands. The residual two orbitals make the weak out-of-plane π bonds and therefore the π and π^* bands, which will be considered in the electronic band structure in the following. Within the tight-binding approach, the eigenfunction $\Psi_l(\mathbf{k}, \mathbf{r})$ for a band with index l can be written as a linear combination of n Bloch wave functions $\Phi_m(\mathbf{k}, \mathbf{r})$ [Bostwick2009]:

$$\Psi_l(\mathbf{k}, \mathbf{r}) = \sum_{m=1}^n C_{lm}(\mathbf{k}) \cdot \Phi_m(\mathbf{k}, \mathbf{r}) \quad (1.5)$$

with

$$\Phi_m(\mathbf{k}, \mathbf{r}) = \frac{1}{\sqrt{N}} \sum_{\mathbf{R}_a}^N e^{i\mathbf{k} \cdot \mathbf{R}_a} \cdot \varphi_m(\mathbf{r} - \mathbf{R}_a). \quad (1.6)$$

\mathbf{R}_a denotes the atom position, φ_m is the atomic wave function in state m and the index N accounts for the N unit cells in the solid.

The coefficients C_{lm} of the eigenfunction $\Psi_l(\mathbf{k}, \mathbf{r})$ need to be determined by minimizing the eigenvalue E_l , which is a function of C_{lm} . This can be written as:

$$E_l(\mathbf{k}) = \frac{\langle \Psi_l | \hat{H} | \Psi_l \rangle}{\langle \Psi_l | \Psi_l \rangle} \quad \text{and} \quad \frac{\partial E_l}{\partial C_{lm}^*} = 0 \quad (1.7)$$

Inserting Ψ from (1.6) into (1.7) and minimizing the energy E_l leads to the expression for C_{lm} :

$$\sum_{m'}^N H_{mm'} C_{lm'}(\mathbf{k}) = E_l(\mathbf{k}) \sum_{m'}^N S_{mm'} C_{lm'}. \quad (1.8)$$

The integrals over the Bloch wave functions $H_{mm'}$ and $S_{mm'}$ are named transfer integral matrices and overlap integral matrices. By defining a column vector for $C_{lm'}$ the matrix form of the eigenvalue equation can be written as:

$$\hat{H}(\mathbf{k}) C_l(\mathbf{k}) = E_l(\mathbf{k}) \hat{S}(\mathbf{k}) C_l(\mathbf{k}). \quad (1.9)$$

The transposition of this equation leads to the secular form:

$$\det [\hat{H} - E \hat{S}] = 0. \quad (1.10)$$

If \hat{S} is neglected for the nearest neighbor approximation which allows the hopping between the atoms A and B $\hat{H} = \begin{pmatrix} H_{AA} & H_{AB} \\ H_{BA} & H_{BB} \end{pmatrix}$ and H_{AB} given by

$$H_{AB} = \langle \Phi_A | H | \Phi_B \rangle \quad (1.11)$$

leads to

$$H_{AB} = -t \sum_{i=1}^3 e^{i\mathbf{k} \cdot \delta_i} \quad (1.12)$$

with t as the hopping parameter. Therefore one can define:

$$f(\mathbf{k}) = -t(e^{-i\mathbf{k} \cdot \delta_1} + e^{-i\mathbf{k} \cdot \delta_2} + e^{-i\mathbf{k} \cdot \delta_3}) \quad (1.13)$$

and the tight-binding Hamiltonian can be written as:

$$\hat{H}(\mathbf{k}) = \begin{pmatrix} 0 & f(\mathbf{k}) \\ f^*(\mathbf{k}) & 0 \end{pmatrix} \quad (1.14)$$

To get the Hamiltonian around the \mathbf{K} -point a Taylor expansion around the \mathbf{K} -valleys is used. For the analytical calculation the vectors (1.4) and the definition of the \mathbf{K} and \mathbf{K}' points are used. The Taylor expansion of the functions $f(\mathbf{k})$ is given by:

$$T(\mathbf{k}) = f(\mathbf{K}) + \nabla f(\mathbf{k})|_{\mathbf{k}=\mathbf{K}/\mathbf{K}'} \cdot \underbrace{(\mathbf{k} - \mathbf{K})}_{\mathbf{q}} \quad (1.15)$$

where $f(\mathbf{K})$ is zero. Therefore only the second term needs to be calculated:

$$\nabla f(\mathbf{k})|_{\mathbf{k}=\mathbf{K}} = it (\delta_{\mathbf{x}_1} e^{-i\mathbf{k} \cdot \delta_1} + \delta_{\mathbf{x}_2} e^{-i\mathbf{k} \cdot \delta_2} + \delta_{\mathbf{x}_3} e^{-i\mathbf{k} \cdot \delta_3}) q_x \quad (1.16)$$

$$+ it (\delta_{\mathbf{y}_1} e^{-i\mathbf{k} \cdot \delta_1} + \delta_{\mathbf{y}_2} e^{-i\mathbf{k} \cdot \delta_2} + \delta_{\mathbf{y}_3} e^{-i\mathbf{k} \cdot \delta_3}) \cdot q_y \quad (1.17)$$

$$= it \left(\frac{a_{cc}}{2} (e^{(-i(2\pi/3))} + e^{-i(0)}) - a_{cc} e^{i(-2\pi/3)} \right) \cdot q_x \quad (1.18)$$

$$+ it \left(\frac{\sqrt{3}a_{cc}}{2} (e^{-i(2\pi/3)} - e^{-i(0)}) \right) \cdot q_y \quad (1.19)$$

$$= \frac{3ta_{cc}}{4} (\sqrt{3} + i)(q_x - iq_y). \quad (1.20)$$

For K' it follows:

$$\nabla f(\mathbf{k})|_{\mathbf{k}=\mathbf{K}'} = \frac{3ta_{cc}}{4} (\sqrt{3} + i)(q_x + iq_y) \quad (1.21)$$

To simplify the expression the pre-factor is written as $p = \frac{3ta_{cc}}{4}(\sqrt{3} + i)$ that gives the massless Dirac Hamiltonian

$$\hat{H}_{Graphene} = \begin{pmatrix} 0 & p(q_x + \tau iq_y) \\ p^*(q_x - \tau iq_y) & 0 \end{pmatrix} \quad (1.22)$$

where $\tau = \pm 1$ indicates whether the Hamiltonian is centered on the \mathbf{K} or \mathbf{K}' valley of the hexagonal Brillouin zone.

The eigenvalues E defined by $\hat{H}\mathbf{v} = \lambda\mathbf{v}$ are:

$$\det(\hat{H} - \mathbb{1}E) = E^2 - pp^*(q_x^2 + q_y^2) \quad (1.23)$$

$$\Rightarrow E = \pm \sqrt{pp^*(q_x^2 + q_y^2)} \quad (1.24)$$

$$= \pm \frac{3ta_{cc}}{2} \sqrt{q_x^2 + q_y^2} \quad (1.25)$$

Inserting those in $\hat{H} - \mathbb{1}E$ to solve the matrix problem $\hat{H} \cdot \mathbf{V}_{eigen} = \mathbf{0}$ leads to the eigenvectors:

$$\mathbf{V}_{eigen_1} = \frac{1}{\sqrt{2}} \begin{pmatrix} \frac{p(q_x - \tau i q_y)}{\sqrt{pp^*(q_x^2 + q_y^2)}} \\ 1 \end{pmatrix} \quad \mathbf{V}_{eigen_2} = \frac{1}{\sqrt{2}} \begin{pmatrix} \frac{-p(q_x - \tau i q_y)}{\sqrt{pp^*(q_x^2 + q_y^2)}} \\ 1 \end{pmatrix}. \quad (1.26)$$

Fermi velocity

Using the classical relation $\frac{dH}{dp} = \dot{q}$ with the momentum p and the velocity \dot{q} , the correspondence of $H \rightarrow E$, $p \rightarrow \hbar k$ and $\dot{q} \rightarrow v_F$ leads to the Fermi velocity in graphene as [8]

$$v_F = \frac{1}{\hbar} \frac{dE}{dk} = \frac{1}{\hbar} \frac{3ta_{cc}}{2} \quad (\approx 1 \times 10^6 \frac{m}{s}). \quad (1.27)$$

Bandstructure

The theoretical electronic dispersion of pristine graphene along three high-symmetry lines in the honeycomb lattice as shown in Figure 1.6(a) with the energy in units of t . A tight-binding model with nearest neighbor approximation describes the evolution of the graphene Fermi surface under exposure to Cs. Figure 1.6(b-e) shows the changes of the band structure starting from a slightly doped ($t = 0.1, 0.5$)(a-b) to a heavily doped state just before(c), at(d) and beyond(e) the Lifshitz transition [9, 10] ($t = 0.9, 0.99, 1.01$) and the Cs induced filling of unoccupied states. The two convex Fermi surfaces turn into one concave surface with a flat band at the M point of the Brillouin zone.

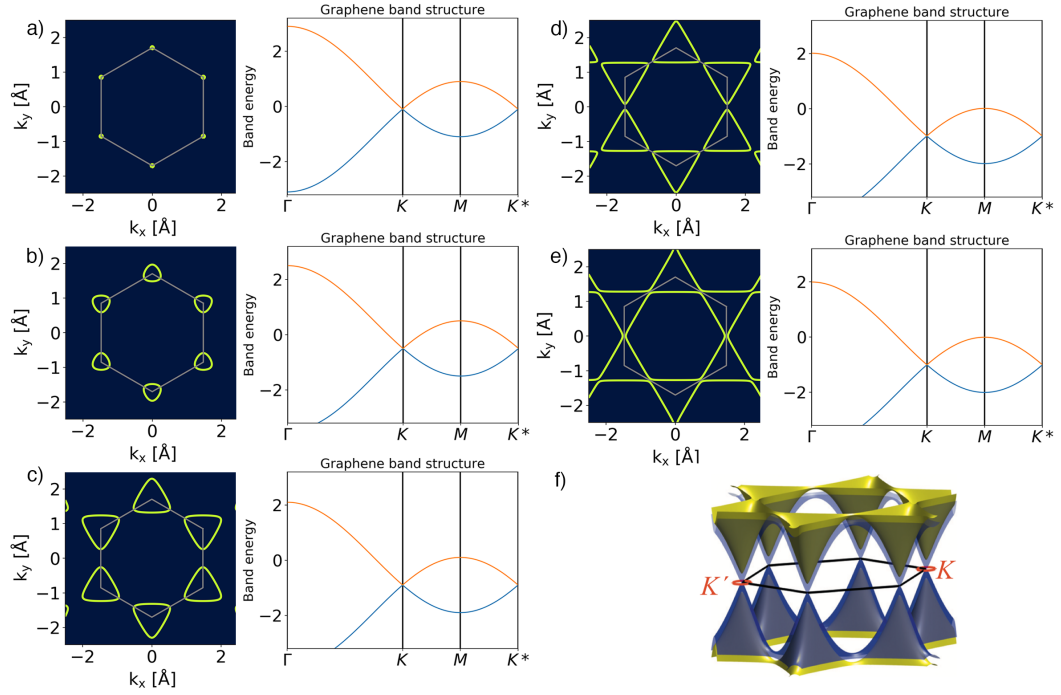


Figure 1.6: Evolution of the band structure and Fermi surfaces towards a Lifshitz transition in Cs doped graphene. a) pristine graphene, b-e) the evolution of the band structure with an increasing amount of Cs doping towards a Lifshitz transition, f) 3D view of e) adapted from [11].

Flat bands in graphene

A flat band in graphene can be induced by engineering the stacking order [12–15], the twist angle (1.1° in bilayer graphene) [16, 17] and the doping level [18]. In the case of doping, the flat band at the M point of the Brillouin zone can be induced by sandwiching a graphene monolayer between two Cs layers. This doping approach is a new technique to induce a flat band at E_F of epitaxial graphene, caused by the combined effects of zone folding, hybridization and the excess of Cs/C stoichiometry. Zone folding of energy bands occurs in the periodic potential of alkali atoms, and was studied for graphite intercalation compounds [19] and alkali-metal doped bilayer graphene [20]. The zone folding refers to the folding of graphene bands into a smaller supercell, leading to an increased number of bands in the folded Brillouin zone. It causes the graphene bands close to E_F to occupy a central region of the Brillouin zone. Since the alkali metal band is also located around the Brillouin zone center

for energies close to E_F , hybridization between the graphene bands and the Cs band is possible. Without the zone folding, no hybridization would be possible, because the bands of graphene and Cs do not cross. A condition for the hybridization is that the alkali metal band is partially filled, i.e. the alkali atom should not be fully ionized. The conflicting conditions of a high doping that leads to a flat band and a partially occupied alkali metal band are combined by using highly ordered Cs layers on top of graphene and underneath graphene[Chapter 2.2].

1.4 Photoemission spectroscopy

Photoemission spectroscopy measurements (PES) are based on the photo effect which was first observed by Hertz in 1887 [21] and later interpreted by Einstein in 1905 [22]. It allows the direct analysis of the electronic band structure and electron dispersion of solids.

$$E_{kin} = h \cdot \nu - \Phi - E_B \quad (1.28)$$

In Figure 1.8 the main principle of a light induced electron emission is shown. Electrons with a binding energy E_B are emitted from the valence band in the bulk surface when hit by photons with a specified energy $h \cdot \nu$ which is big enough to overcome the work function Φ of the solid. Following equation (1.28) the exited electrons enter the vacuum with a kinetic energy E_{kin} and a certain momentum k which is related to the emission angle ϑ . The emitted electrons are detected by a hemispherical analyzer and a photoemission spectrum is observed. By applying a sufficient photon energy PES it is possible to analyze the density of states of the valence bands as well as the core level states. The photoemission process describes an excitation of an N -electron system with the energy $E_i^N = E_i^{N-1} - E_B^k$ by a photon from a ground state to an excited state with $E_f^N = E_f^{N-1} + E_{kin}$ which should be ideally described in one step. For the interpretation of photoemission experiments, the so-called three-step model (Figure 1.8), describing the whole PES process in three separate steps, has been proven to be extremely useful [24]. In this model, the one-step process is divided into three independent and sequential steps that represent different aspects of the problem:

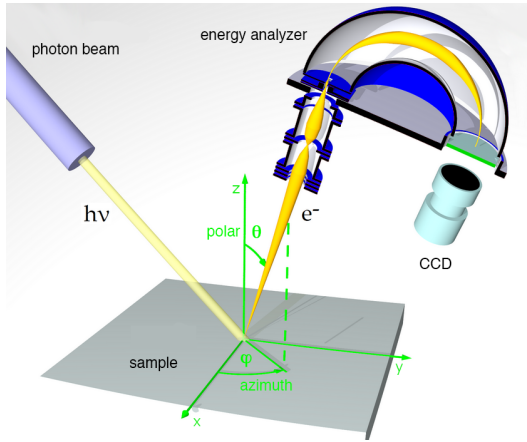


Figure 1.7: Schematic experimental setup for ARPES [23] depicting the photon beam to the sample and the analyzer with the two concentric hemispheres.

- (i) In the first step the photoionization takes place. A photon is absorbed locally and an electron is excited in the bulk of the solid.
- (ii) The second step describes the transport of the excited electron inside the bulk to the surface.
- (iii) The third step describes the escape of the photoelectron through the surface potential barrier into the vacuum, where it is detected.

The photoexcitation probability per unit time is described by Fermi's golden rule:

$$\omega_{fi} = \frac{2\pi}{\hbar} |\langle \Psi_f^N | H_{int} | \Psi_i^N \rangle|^2 \delta(E_f^N - E_i^N - h\nu). \quad (1.29)$$

The **excitation** process can be described as a transition of the electronic system from an initial to a final state. In the initial state, the electronic system of the solid is described by an N -electron wave function Ψ_i . After photoexcitation, the system is described by another N -electron wave function Ψ_f , comprising the $N-1$ electrons remaining in the solid plus the emitted photoelectron. During the **transport** through the solid, the electrons undergo elastic and inelastic scattering owing to the potential of the crystalline solid. The elastically scattered outgoing photoelectron waves are diffracted in the solid. This effect can be applied as a method to determine the geometrical environment of an emitting atom. Due to inelastic scattering, photoelectrons lose kinetic energy by exciting secondary electrons, plasmons, and phonons. This limits the escape depth of the photoelectrons, described by λ , the so-called inelastic-mean-free path. The intensity $I(d)$ of the emitted electrons is

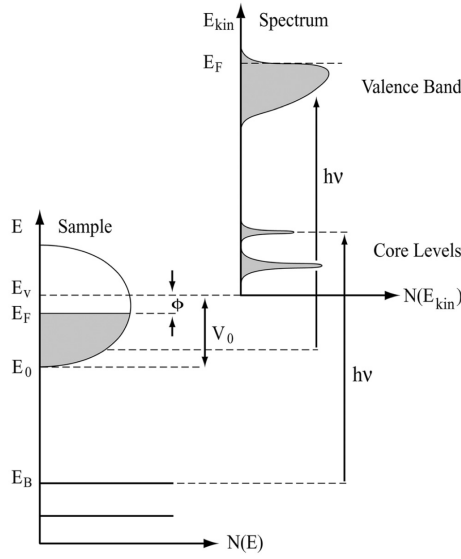


Figure 1.8: Simplified schematic for the photoemission spectroscopy of a metallic material. The core levels and the valence band in the solid lead to a corresponding kinetic energy distribution in the photoelectrons. [24]

given by

$$I(d) = I_0 e^{-\frac{d}{\lambda}} \quad (1.30)$$

where I_0 is proportional to the number of the excited electrons.

During the **escape** of electrons into the vacuum only the parallel component of the wave vector is conserved modulo a reciprocal surface wave vector due to the periodicity of the lattice potential parallel to the surface. Neglecting "umklapp"-processes \mathbf{k}_{\parallel} can be described with the kinetic energy and the emission angle ϑ by

$$\mathbf{k} = \mathbf{k}_{\perp} + \mathbf{k}_{\parallel} = \mathbf{p}/\hbar$$

$$|\mathbf{k}| = \sqrt{2 \cdot m \cdot E_{kin}}/\hbar \quad (1.31)$$

$$\mathbf{k}_{\parallel} = \frac{1}{\hbar} \sqrt{2 \cdot m \cdot E_{kin}} \cdot \sin(\vartheta)$$

Measuring E_{kin} and ϑ in PES experiments fixes \mathbf{k}_{\parallel} which is sufficient for surface states but not for bulk bands. To measure the band dispersion along a direction perpendicular to surface a variable photon energy source is necessary. Due to the discontinuity of the potential at the surface/vacuum interface, the perpendicular component of the electron wave vector is not conserved. The component normal to the surface is given by

$$\mathbf{k}_{\perp} = \frac{1}{\hbar} \sqrt{2 \cdot m \cdot (E_{kin} \cdot \cos^2(\vartheta) + V_0)} \quad (1.32)$$

A conventional energy analyzer (Figure 1.7) consists of a multi-element electrostatic input lens, a hemispherical deflector with entrance and exit slits, and an electron detector. The most important part of the analyzer is the deflector which consists of two concentric hemispheres of radius R_1 and R_2 . These hemispheres are kept at a potential difference ΔV . Only electrons within a narrow range centered at $E_{pass} = e\Delta V/(R_1/R_2 - R_2/R_1)$ reach the entrance slit with kinetic energy and will pass through this hemispherical capacitor, thus reach the exit slit and then the detector. Thereby it is possible to measure the kinetic energy of the photoelectrons with an energy resolution given by $\Delta E_a = E_{pass}(\omega/R_0 + \alpha^2/4)$; where $R_0 = (R_1 + R_2)/2$; ω is the width of the entrance slit, and α is the acceptance angle. Either synchrotron light or gas discharge lamps can be used as a light source. The disadvantage of gas discharge lamps is the limited photon energy of 21.2 eV or 40.8 eV but the costs are much lower compared to synchrotron light which is tunable regarding photon energy and features a much higher brilliance. The measurements in these thesis were taken at Elettra Synchrotron Trieste (Figure 1.9) in Italy at the beamline BaDElPh.



Figure 1.9: Elettra light source [25].

1.5 Raman spectroscopy

Scattered light can be thought of as a redirection of light that takes place when an electromagnetic wave encounters an obstacle. When the electromagnetic wave interacts with matter, the electron orbits within the constituent molecules are perturbed periodically with the same frequency as the electric field of the incident wave. The oscillation of the electron cloud results in

a periodic separation of charge within the molecules. This is called an induced dipole moment. The oscillating induced dipole moment manifests as an electromagnetic radiation source and therefore results in scattered light. The majority of the scattered light is emitted at the identical frequency of the

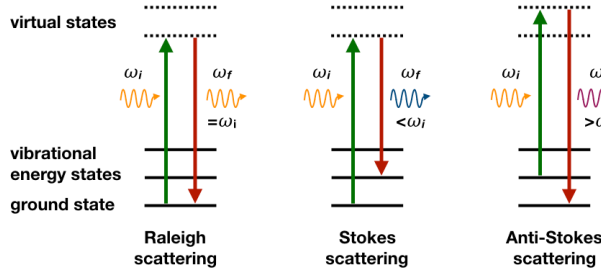


Figure 1.10: Schematic for Rayleigh and Raman (Stokes and anti-Stokes) scattering.

incident light. This process is due to elastic scattering. Additional light is scattered at different frequencies, which is referred to inelastic scattering and Raman scattering is one such example of inelastic scattering. When the incident electromagnetic wave induces a dipole moment during the light-material interaction, the strength of the induced dipole

moment, P , is given by [26]

$$P = \alpha \cdot \bar{E} \quad (1.33)$$

with α as the polarizability and \bar{E} is the strength of electric field of the incident electromagnetic wave. The polarizability is a material property and depends on the molecular structure and nature of the bonds. For the incident electromagnetic wave, the electric field can be expressed as

$$\bar{E} = E_0 \cos(2\pi\nu_0 t) \quad (1.34)$$

where ν_0 is the frequency of the incident wave ($\nu_0 = c/\lambda$). Substituting Eq. (1.34) into (1.33) gives the time-dependent induced dipole moment,

$$P = \alpha E_0 \cos(2\pi\nu_0 t). \quad (1.35)$$

For any molecular bond, the individual atoms are confined to specific vibrational (rotational) modes. The vibrational energy levels are quantized in a manner similar to electronic energies. The vibrational energy of a particular mode is given by $E_{vib} = (j + 1/2) h \nu_{vib}$ with j as the vibrational quantum number ($j = 0, 1, 2, \dots$), ν_{vib} as the frequency of the vibrational mode, and h is the Planck constant. The physical displacement dQ of the atoms about their

equilibrium position due to the particular vibrational mode can be described as:

$$dQ = Q_0 \cos(2\pi \nu_{vib} t). \quad (1.36)$$

Q_0 is then the maximum displacement about the equilibrium position. For small displacements, the polarizability can be approximated by a Taylor series expansion:

$$\alpha = \alpha_0 + \frac{\partial \alpha}{\partial Q} dQ \quad (1.37)$$

Here α_0 is the polarizability of the molecular mode at equilibrium position. Based on the vibrational displacement of Eq.(1.36), the polarizability is given by

$$\alpha = \alpha_0 + \frac{\partial \alpha}{\partial Q} Q_0 \cos(2\pi \nu_{vib} t). \quad (1.38)$$

Finally, Eq.(1.38) may be substituted into Eq.(1.35), which yields

$$P = \alpha_0 E_0 \cos(2\pi \nu_0 t) + \frac{\partial \alpha}{\partial Q} Q_0 E_0 \cos(2\pi \nu_0 t) \cos(2\pi \nu_{vib} t). \quad (1.39)$$

With use of a trigonometric identity, the relation can be recast as

$$P = \alpha_0 E_0 \cos(2\pi \nu_0 t) + \left(\frac{\partial \alpha}{\partial Q} \frac{Q_0 E_0}{2} \right) \{ \cos[2\pi (\nu_0 - \nu_{vib}) t] + \cos[2\pi (\nu_0 + \nu_{vib}) t] \}. \quad (1.40)$$

The induced dipole moments are created at three distinct frequencies, ν_0 , $(\nu_0 - \nu_{vib})$, and $(\nu_0 + \nu_{vib})$, resulting in scattered radiation at these three frequencies. The first scattered frequency relates to the incident frequency and is elastic scattering (Mie or Rayleigh) as depicted in Figure 1.10. The other frequencies are shifted to lower or higher wavenumbers and are hence inelastic processes. The scattered light in the latter two cases is the Raman scattering with the down-shifted frequency as Stokes scattering, and the up-shifted frequency as anti-Stokes scattering. The necessary condition for Raman scattering is that $\frac{\partial \alpha}{\partial Q}$ must be non-zero meaning that the vibrational displacement of atoms corresponds to a particular vibrational mode that result in a change in the polarizability.

To perform Raman spectroscopy a laser as the excitation source is generally used. The intense, collimated monochromatic light allows measurements of relatively small Raman shifts, while the intense beam improves the spatial resolution and signal-to-noise ratio. Usually, the Raman signal intensity is

orders of magnitude weaker than the stray light intensity caused by elastic scattering. Therefore spectrometers are used with notch filters or edge filters (sharp cut-off high pass filters) to separate the elastic scattering and Raman scattering signals and reject the elastically scattered light prior to entering the spectrometer.

Raman spectroscopy in graphene

A typical Raman spectrum of graphene is dominated by two bands, one at $\approx 1580 \text{ cm}^{-1}$ and another at $\approx 2700 \text{ cm}^{-1}$. The former is the G band, the only allowed first order Raman band. The second band is the result of a higher order process involving two phonons. This band has been referred to as 2D mode and originates from a double resonance process. The G mode originates from the E_{2g} in-plane phonon at the Γ point where the longitudinal optical (LO) and transverse optical (TO) branches touch each other whilst the 2D is a result of a double resonance enhanced two-phonon process and only zone-boundary phonons have proper frequencies for this. In fact, the 2D band originates from two TO phonons around the K point. Another band at $\approx 1350 \text{ cm}^{-1}$ and is called the D band which is a disorder induced band. The intensity of this band increases with increasing levels of disorder. This band is at half the frequency of the 2D band: the 2D is the overtone of the D band, which is noteworthy because the 2D band does not require any disorder. It is worth to note that there is also another band induced by disorder at $\approx 1620 \text{ cm}^{-1}$ called D' band. This band is very similar to the D band except that the phonons generating it are in the vicinity of the Γ point, not the K point [27, 28].

Electronic Raman scattering

In graphene, the shape and position of the Raman spectra can give a deep understanding of the electron energy dispersion [29], phonon energy dispersion [30], the Kohn anomaly [5], and structure characterization [31]. Especially the asymmetric Breit-Wigner-Fano (BWF) line shape, observed in the Raman spectra of graphite intercalation compounds [32] and metallic nanotubes [33], probes the interference between the continuum spectra with the discrete spectra [4]. The origin of the Fano line shape in graphene comes from the con-

tinuous single-particle electron-hole pair spectra, interfering with the discrete phonon spectra. The single-particle electron-hole pair spectra are referred to as the electronic Raman scattering (ERS) [34]. The Fano line shape can be fitted to the G band Raman spectra by using:

$$F(\omega) = I_0 \frac{(1 + \frac{\omega - \omega_0}{q\gamma/2})^2}{1 + (\frac{\omega - \omega_0}{\gamma/2})^2}. \quad (1.41)$$

Here ω , ω_0 , $1/q$ and γ and I_0 are the Raman shift, the spectral peak position, the asymmetric factor, the full-width at half-maximum and the maximum Raman intensity of the spectra, respectively. When $1/q = 0$ the equation (1.41) gives a Lorentzian line shape which represents a discrete phonon spectrum indicating no interference effect.

1.6 Transport properties of graphene

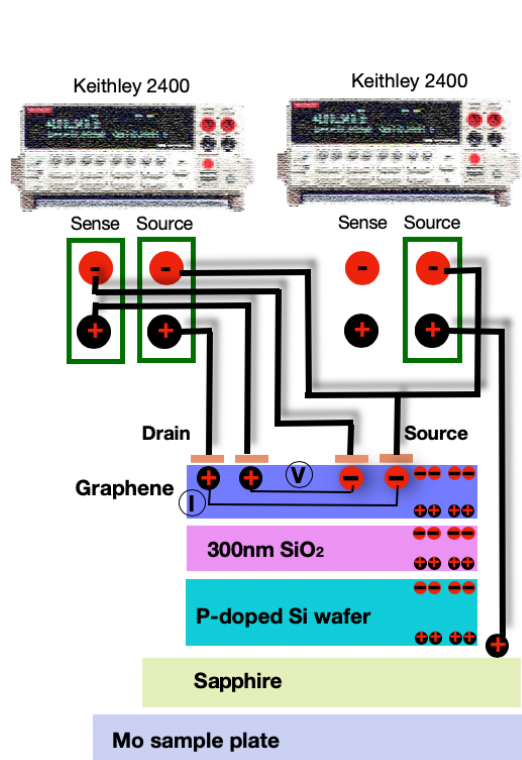


Figure 1.11: UHV transport setup

Transport measurements were taken under UHV conditions using a special sample carrier with the corresponding sample receptor, as shown in Figure 1.3. The measurement geometry is depicted in Figure 1.11 with the sample glued on a quartz or Al_2O_3 plate, insulating the sample from the molybdenum carrier. The setup features five contacts allowing the simultaneous measurement of resistance in a four-point geometry in combination with additional back-gating. For a geometry of an infinite graphene sheet with contacts within the graphene, the resistance is determined by:

$$R = \frac{2\pi}{\ln(2)} \cdot \frac{V}{I} \quad (1.42)$$

where V/I is the measured four point resistance for a four probe geometry on a square [35]. The sheet resistance given by the van der Pauw technique requires several conditions that must be satisfied:

1. The sample must be flat and have a uniform thickness.
2. The sample must have no isolated holes.
3. The sample must be isotropic and homogeneous.
4. All contacts must be located at the edge of the sample.

In addition to these conditions, the area of any of the contacts must be at least an order of magnitude smaller than the area of the entire sample. In the case of a ratio of contact to sample perimeter less than approximately 0.3, there is negligible correction to the ideal van der Pauw formula [36]. For this the four-point resistance is given by:

$$R = \frac{\pi}{\ln(2)} \cdot \frac{V}{I} \quad (1.43)$$

The calculation of doping induced charge carriers is analyzed by the shift of the resistance curve versus gate voltage. The charge carrier density n is estimated according to:

$$n = \frac{CV}{eA} \quad (1.44)$$

with $C = \epsilon\epsilon_0 \cdot A/d$ (here C is the sheet capacitance of the back gate, V_D the gate voltage of maximum sheet resistance, e is the elementary charge, $\epsilon_{(0)}$ the vacuum permittivity respectively for SiO_2 , and d the thickness of the oxide layer). For a 300 nm SiO_2 wafer we get $C = 11.5 \frac{nF}{cm^2}$ with $\epsilon = 3.9$ [37]. The quality of the transferred graphene can be estimated from the field effect mobility μ_{FE} which is given as:

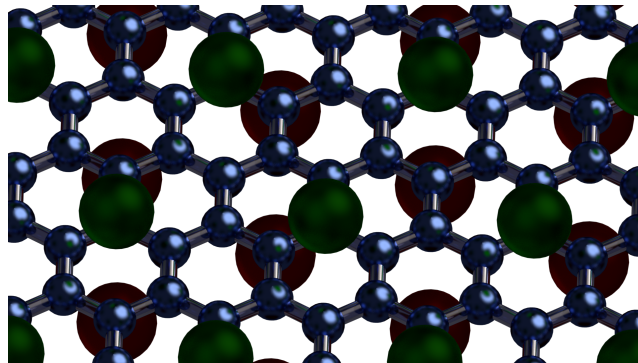
$$\mu_{FE} = \frac{1}{C} \cdot \frac{d(\frac{1}{R})}{dV}. \quad (1.45)$$

Here $\frac{d(\frac{1}{R})}{dV}$ is the derivative of the reciprocal sheet resistance with respect to the gate voltage V .

Chapter 2

Publications

2.1 Resonance Raman spectrum of doped epitaxial graphene at the Lifshitz transition



Resonance Raman Spectrum of Doped Epitaxial Graphene at the Lifshitz Transition

Martin G. Hell,[†] Niels Ehlen,^{†,‡} Boris V. Senkovskiy,^{†,§} Eddwi H. Hasdeo,^{†,§} Alexander Fedorov,^{†,||} Daniela Dombrowski,^{†,⊥} Carsten Busse,^{†,¶} Thomas Michely,[†] Giovanni di Santo,^{||} Luca Petaccia,^{||} Riichiro Saito,[‡] and Alexander Grüneis^{*,†,||}

[†]II. Physikalisches Institut, Universität zu Köln, Zùlpicher Strasse 77, 50937 Köln, Germany

[‡]Department of Physics, Tohoku University, Sendai 980-8578, Japan

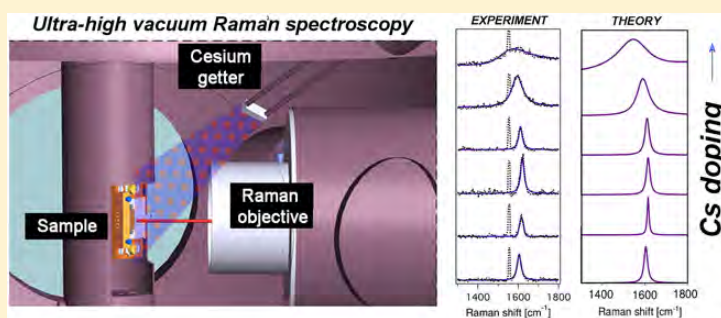
[§]Research Center for Physics, Indonesian Institute of Sciences, Kawasan Puspiptek Serpong, Tangerang Selatan 15314, Indonesia

[⊥]Institut für Materialphysik, Westfälische Wilhelms-Universität Münster, Wilhelm-Klemm-Str. 10, 48149 Münster, Germany

[¶]Fakultät IV Physik, Universität Siegen, Walter-Flex-Str. 3, 57072 Siegen, Germany

^{||}Elettra Sincrotrone Trieste, Strada Statale 14 km 163.5, 34149 Trieste, Italy

Supporting Information



ABSTRACT: We employ ultra-high vacuum (UHV) Raman spectroscopy in tandem with angle-resolved photoemission (ARPES) to investigate the doping-dependent Raman spectrum of epitaxial graphene on Ir(111). The evolution of Raman spectra from pristine to heavily Cs doped graphene up to a carrier concentration of $4.4 \times 10^{14} \text{ cm}^{-2}$ is investigated. At this doping, graphene is at the onset of the Lifshitz transition and renormalization effects reduce the electronic bandwidth. The optical transition at the saddle point in the Brillouin zone then becomes experimentally accessible by ultraviolet (UV) light excitation, which achieves resonance Raman conditions in close vicinity to the van Hove singularity in the joint density of states. The position of the Raman G band of fully doped graphene/Ir(111) shifts down by $\sim 60 \text{ cm}^{-1}$. The G band asymmetry of Cs doped epitaxial graphene assumes an unusual strong Fano asymmetry opposite to that of the G band of doped graphene on insulators. Our calculations can fully explain these observations by substrate dependent quantum interference effects in the scattering pathways for vibrational and electronic Raman scattering.

KEYWORDS: Alkali doping, graphene, UHV Raman, ARPES, Lifshitz

Raman spectroscopy is the most widely used characterization method for graphene.^{1–4} The electron and phonon systems of graphene are strongly coupled to each other by electron–phonon interactions.^{5,6} These interactions manifest as “kink” features in the electronic spectral function^{7–12} and as Kohn anomalies in the phonon dispersion relations around the Brillouin zone (BZ) center (Γ point) and corners (K points).^{5,6} As a consequence, the carrier concentration of graphene sensitively affects the position, line shape, and intensity of the first- and second-order Raman spectra corresponding to these phonon modes. The effects of phonon renormalization due to the removal of the Kohn

anomaly or lattice expansion on the phonon energy are quantitatively understood.⁵ Phonon renormalization results in a phonon upshift for Fermi level positions higher than half the phonon frequency (measured from the Dirac point) and lattice expansion results in a phonon downshift.^{5,6} Experimentally, phonon hardening has been observed in Raman measurements where the charge carrier concentration of graphene has been tuned by field effect gating^{6,13} or by ionic liquid gating.^{14–16}

Received: July 21, 2018

Revised: August 21, 2018

Published: August 29, 2018

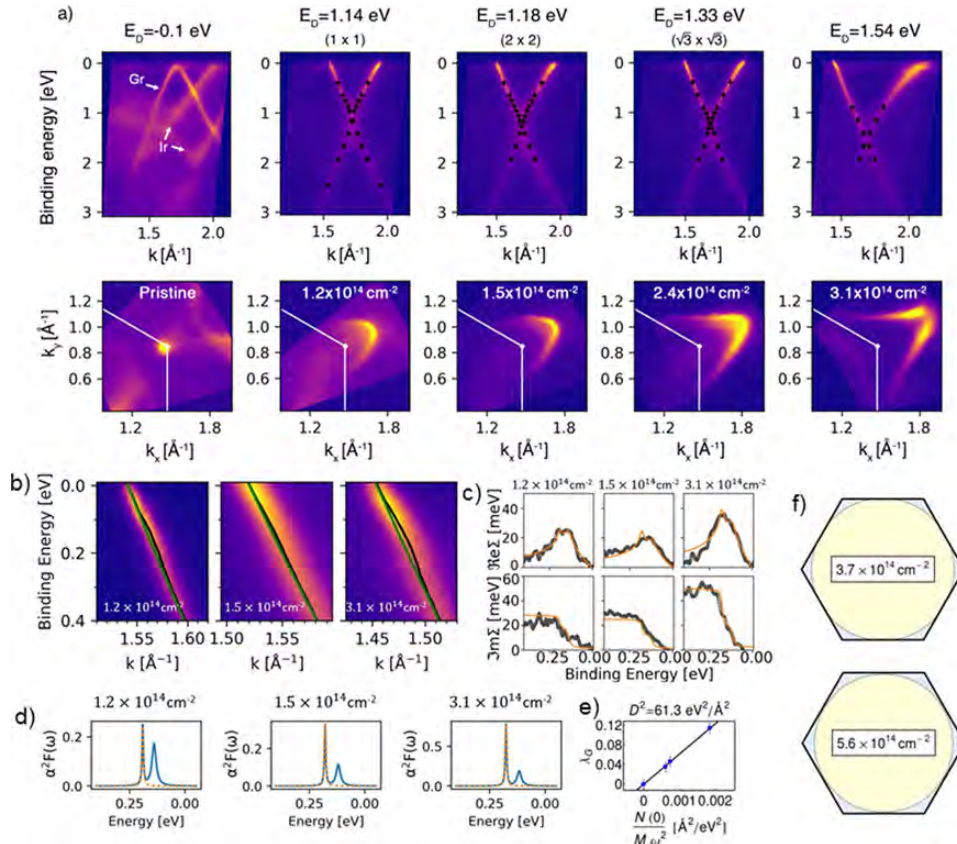


Figure 1. (a) ARPES scans of Cs doped graphene/Ir(111) in the Γ KM direction (top panel) and Fermi surface maps (bottom panel) for different Cs coverages. The shift of the Dirac point is indicated in the top panel and the carrier concentration of graphene per cm^2 is indicated in the bottom panel. (b) High-resolution ARPES data in the vicinity of the kink feature along the Γ K direction. Black and green lines denote ARPES intensity maxima and the bare band, respectively. (c) Real and imaginary part of the self-energy (denoted as $\Re\Sigma$ and $\Im\Sigma$) for different doping levels. (d) Eliashberg functions (blue) and contribution of the G band phonon (orange) along Γ K as a function of carrier concentration. The orange lines in panel c denote the self-energy functions that are calculated from these Eliashberg functions. (e) Fit of the deformation potential D^2 (see text for details). (f) Tight-binding calculation of the Fermi surfaces of doped graphene (blue regions) for carrier concentrations just before and beyond the Lifshitz transition.

The latter approach has been used to induce large carrier densities of $6 \times 10^{13} \text{ cm}^{-2}$ (ref 15). Even for such high carrier concentrations, phonon hardening due to phonon self-energy corrections dominates.⁵ However, when the carrier density is in the 10^{14} cm^{-2} range that has already been probed by transport,^{17,18} the Fermi energy can be in the vicinity of the van Hove singularity at the M point in the Brillouin zone and phonon softening will then dominate. Achieving and probing high carrier densities is fundamentally important for both conventional^{19–21} and chiral superconductivity²² in monolayer graphene. The latter case requires the Fermi level to touch the saddle point van Hove singularity at the M point in the two-dimensional (2D) BZ. In this case, the Fermi surface of graphene assumes a closed shape centered at the Γ point rather than two surfaces centered around the K and K' points. The transition of topology from two Fermi surfaces to one Fermi surface marks the Lifshitz transition²³ in graphene.

The present work aims at understanding the peculiar Raman spectrum of graphene at the Lifshitz transition and unravelling the deep underlying connection between electronic band

structure and phonon renormalization in heavily doped graphene. To that end, we synthesize Cs doped graphene up to the highest achievable carrier concentrations. The energy bands are renormalized significantly due to doping and are probed by angle-resolved photoemission spectroscopy (ARPES) for each doping step. Despite the fact that Raman spectroscopy is typically not considered a surface science method, we present an original ultrahigh-vacuum (UHV) Raman setup that employs a commercial Raman system coupled to a UHV system. From these experiments, we can relate the observed changes in the vibrational and electronic spectrum to band structure changes. We thus obtain a complete picture of the coupled electron–phonon system in epitaxial graphene.

McChesney et al. already experimentally observed the Lifshitz transition in heavily doped graphene using ARPES.²⁴ Their key finding was that the band structure of heavily doped graphene is strongly renormalized, yielding a flat conduction band at the Fermi level, that is, an extended van Hove singularity.²⁴ Importantly, the renormalization also reduces the

transition energy at the saddle point between valence and conduction bands. Indeed, Mak et al. found that the energy of the M point transition is reduced by ~ 200 meV when going from charge neutrality to 1×10^{14} carriers per cm^2 (ref 25).

For graphene, the first-order Raman spectrum due to zone-center optical phonons with in-plane polarization (the G band) shows an asymmetric Fano line shape if graphene is doped by field effect gating²⁶ or alkali metal doping.²⁷ This line shape is reproduced theoretically by considering the interference between a discrete transition (phonon) to a continuum (excitation of electron-hole pairs), which is known as electronic Raman spectra (ERS).^{28–31} The Fano line shape of the G band is more pronounced for larger doping levels²⁶ and for a higher layer number.²⁷ The most pronounced Fano asymmetries are obtained in stage 1 graphite intercalation compounds such as KC_8 .^{32,33} Doping also has a strong influence on the G band intensity,³⁴ which is determined by quantum interference in the Raman scattering pathways.^{15,35} Upon doping, transitions between two occupied (unoccupied) states are forbidden by Pauli blocking and do not contribute to the total Raman intensity. As a consequence, the G band intensity as a function of doping level is peaked for the condition $2E_F = E_{\text{laser}} - E_{\text{ph}}/2$. Here E_F is the Fermi level position measured from the charge neutrality point, E_{laser} the excitation energy, and E_{ph} the G band phonon energy.¹³

Apart from the limits regarding carrier concentration, ionic liquid gating experiments also block the direct access to the sample surface. This precludes direct observation of the electron energy band structure of gated graphene by ARPES. It thus prohibits a detailed understanding of the nonrigid band shifting and electron-phonon coupling in heavily doped graphene that has been achieved for chemically doped graphene.^{7–12,24} An approach to carry out Raman spectroscopy of chemically doped graphene is to measure it inside a quartz ampule. For example, alkali metal doped graphene^{27,36,37} and FeCl_3 doped graphene³⁸ have been measured in this way. Unfortunately, such experimental setups also preclude band structure measurements by ARPES, structural characterization by low energy electron diffraction (LEED), and efficient sample cooling to liquid He temperatures. Moreover, in the case of alkali doping inside quartz ampules, a fraction of the dopant atoms will be oxidized because of poor vacuum conditions. Combined ARPES and Raman experiments in UHV conditions would not suffer from these drawbacks. Previously, the investigation of the electronic structure of doped graphene has been performed using the standard surface science methods such as ARPES^{9,39,40} and scanning tunneling spectroscopy (STS).^{21,41} These probe the electronic structure of epitaxially grown graphene and directly reveal Fermi level shifts, spectral functions, and superconducting gaps as a function of dopant concentration and type and substrate interactions. Much less is known about the phonons and low energy electronic excitations in alkali metal doped epitaxial graphene despite these contain valuable information regarding doping level, strain, and electron-phonon coupling.

Experimental Results. Electronic Structure of Cs Doped Graphene/Ir(111). In Figure 1a, we show ARPES spectra of pristine and Cs doped graphene. For each amount of deposited Cs, we also have performed structural characterization by LEED (see Supporting Information). Pristine graphene on Ir(111) (see Methods section for details pertaining synthesis) has the R0 structural phase.⁴² This is confirmed by the moiré pattern observed in LEED. The moiré pattern is a result of

corrugations due to chemically modulated substrate interaction.⁴³ It hosts weakly covalently bonded regions with a small charge transfer from graphene to Ir(111).⁴³ Using ARPES (Figure 1a), we find in agreement to previous literature^{42,44} that R0 graphene/Ir(111) is only weakly hole doped. After depositing Cs onto the sample surface at room temperature, we find that the moiré pattern observed in LEED disappears and only the first order diffraction spots are left. This LEED pattern is denoted as 1×1 in the following. The disappearance of the moiré pattern upon Cs deposition is an indication of a change in the graphene-substrate interaction. The graphene-Ir(111) interaction also manifests in minigaps,⁴⁴ which are visible in the ARPES spectrum as regions of weaker π band intensity. After Cs deposition, these minigaps disappear, indicating that Cs doping weakens the local variations in the graphene-Ir(111) interaction. We expect that the charge transfer to graphene becomes homogeneous and removes the hybridization of C and Ir bands. ARPES also confirms a single doping phase as only one Dirac cone is visible. Increasing the Cs amount, we are able to reach an ordered 2×2 phase of Cs on graphene as reported previously.⁴⁵ This phase also has a single Dirac cone in ARPES. Analysis of the experimental Fermi surface from ARPES measurements yields a carrier concentration of $n = 1.5 \times 10^{14} \text{ cm}^{-2}$. Further increasing Cs deposition leads to the $\sqrt{3} \times \sqrt{3}$ phase in LEED and a slightly higher doping level. Here we have $n = 1.5 \times 10^{14} \text{ cm}^{-2}$. To confirm the ARPES derived carrier densities by another method, we also performed Fourier transform scanning tunneling spectroscopy (FT-STs) measurements⁴¹ (see Supporting Information). These indicate carrier concentrations of $1.7 \times 10^{14} \text{ cm}^{-2}$ for the 2×2 phase and $1.9 \times 10^{14} \text{ cm}^{-2}$ for the $\sqrt{3} \times \sqrt{3}$ phase. The carrier concentration for the 2×2 is in excellent agreement to the value from ARPES and to previous experiments.⁴⁵ However, the concentration for the $\sqrt{3} \times \sqrt{3}$ phase from FT-STs is lower by a factor ~ 1.3 when compared to ARPES. This can be understood by the $\sqrt{3} \times \sqrt{3}$ phase corresponding to graphene fully intercalated with Cs. Any extra Cs lies on top of graphene and a system with small amounts of extra Cs on top still shows a $\sqrt{3} \times \sqrt{3}$ diffraction pattern in LEED. Thus, the $\sqrt{3} \times \sqrt{3}$ phase exists for a broader range of adsorbate concentrations and can slightly vary from system to system. Thus, LEED is a good measure of stoichiometry for the 2×2 phase only. To ensure depositing of equal Cs amounts in the Raman and ARPES investigations, we calibrated the deposited Cs using a quartz microbalance as a multiple of the amount of Cs needed for reaching the 2×2 phase. Since the 2×2 phase is well-defined, this approach yields reproducible sample stoichiometries for different samples and in different experimental setups.

Evaporation of excess Cs onto the sample does not result in an ordered phase according to LEED but it is still possible to increase the graphene doping level. At $n = 3.1 \times 10^{14} \text{ cm}^{-2}$ (see Figure 1a), we already see marked deviations from the usually observed trigonal warping in ARPES. As is shown in Figure 1a (bottom row), the warping direction changes from convex to concave. We are able to reach a value of $n = 4.4 \times 10^{14} \text{ cm}^{-2}$ (for the highest value of n , see Supporting Information). Regarding the relation between Cs/C stoichiometry and carrier concentration, we note that each Cs atom may donate less than one electron. However, this does not affect the carrier densities determined from ARPES because this method is not dependent on the stoichiometry but directly measures the

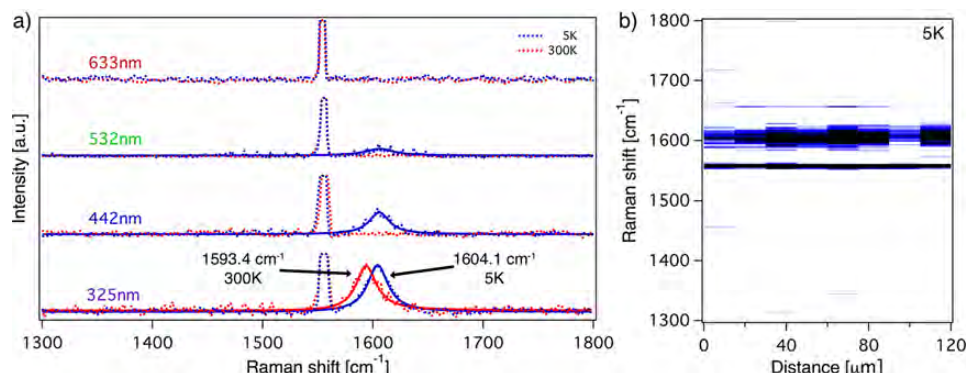


Figure 2. (a) Ultra-high vacuum (UHV) Raman spectrum of pristine graphene/Ir(111) at $T = 5$ K and $T = 300$ K for four different laser wavelengths in the range between red and ultraviolet. The dashed lines denote the experimental data and solid lines Lorentzian fits. The G band taken at 325 nm excitation shows an upshift in frequency upon cooling (indicated by arrows in the lower panel). The sharp line at 1555 cm^{-1} is due to oxygen in the unavoidable part of the laser path outside the vacuum (see Supporting Information Figure S1 for a sketch of the UHV Raman setup). (b) Linescan of the Raman spectrum (at 325 nm) across a $120\text{ }\mu\text{m}$ distance of the sample.

carrier concentration of graphene from the area of the Fermi surface of graphene.

Let us now turn to the analysis of electron–phonon coupling. Figure 1b depicts high resolution scans of the “kink” feature at low binding energy. We first perform a standard self-consistent self-energy analysis^{7–9} of ARPES data in the kink region yielding the complex self-energy and the Eliashberg function. These are depicted in Figure 1c and d, respectively. By integrating the Eliashberg function of graphene⁸ in the region of the G band, we obtain λ_G , the electron–phonon coupling constant for the G mode that is frequently used in ARPES literature. The Raman community often expresses electron–phonon coupling by the deformation potential D^2 . The deformation potential and the electron–phonon coupling constant λ_G are connected as $\lambda_G = N(0)D^2/(M\omega^2)$ (see ref 19). Here $N(0)$ is the electron density of states per unit cell, per eV, and per spin at the Fermi level, M the carbon mass, and ω the G band frequency. The resulting fit of four charge carrier concentrations is depicted in Figure 1e and yields $D^2 = 61.3\text{ eV}^2/\text{\AA}^2$. Finally, Figure 1f depicts a tight-binding calculation of the Fermi surfaces at carrier concentrations just before and beyond the Lifshitz transition. In this figure, we show Fermi surface contours at $n = 3.7 \times 10^{14}\text{ cm}^{-2}$ and at $n = 5.6 \times 10^{14}\text{ cm}^{-2}$. For the higher concentration of $n = 5.6 \times 10^{14}\text{ cm}^{-2}$, we are already above the Lifshitz transition (i.e., the Fermi surface is a single contour) while the lower concentration is just before the Lifshitz transition (i.e., the Fermi surface consists of two contours that almost touch). For the calculation of these Fermi surface contours, we have employed a third-nearest-neighbor tight-binding model⁴⁶ where the matrix elements are fitted to the experimental ARPES band structure. It is clear that the carrier concentration at which the Lifshitz transition happens is in between these two concentrations. Using the same tight-binding model, we estimate a value of $n = 4.4 \times 10^{14}\text{ cm}^{-2}$ where the Lifshitz transition is observable. We expect that the Lifshitz transition is induced purely by doping because we do not observe a lattice deformation. This is corroborated by the diffraction pattern of an overdoped sample above the $\sqrt{3} \times \sqrt{3}$ phase to a doping level close to the Lifshitz transition. The diffraction pattern of this sample [shown in the Supporting Information in

Figure S2(e)] still shows sharp spots in a hexagonal pattern that are due to graphene.

Raman Spectrum of Epitaxial Graphene/Ir(111). In Figure 2, we show the Raman spectra at $T = 300$ K and at $T = 5$ K of epitaxial graphene/Ir(111) measured by lasers with wavelengths 633 nm, 532 nm, 442 nm, and 325 nm. The depicted spectra are the average over 25 points chosen along a scan across $120\text{ }\mu\text{m}$ on the surface. In principle, for interpretation of the observed temperature-dependent spectra, in-plane strain and wrinkle formation due to the different thermal expansion coefficient of graphene and the Ir substrate must be considered.^{47–49} Only the ultraviolet (UV) laser (325 nm) results in a strong Raman signal at room temperature. Upon cooling, the spectra taken by 532 and 442 nm excitation show a weak Raman signal, which could be a sign of temperature induced changes in the substrate interaction. These observations extend previous works reporting the absence of a Raman signal for graphene/Ir(111) that belongs to the R0 structural phase for visible excitation at room temperature.⁴² So far, no quantitative explanation regarding the absence of a Raman signal for visible laser excitation for R0 graphene on Ir(111) has been given. We speculate that it could be explained in terms of minigaps,⁴⁴ which appear at certain energies in the band structure. It has been shown by ARPES that the minigaps are in all directions around K point and close nowhere.⁵⁰ If the laser energy hits a minigap, no electrons can be excited between the valence and conduction π bands of graphene and the Raman intensity is suppressed. The high quality of graphene is also corroborated by the absence of a defect related D peak. Interestingly the 2D peak is absent in all measurements. This observation is in agreement to previous works and might be related to the short lifetime of photoexcited charge carriers in graphene adsorbed on metals, which suppress the 2D intensity.⁵¹

Temperature Induced Strain in Epitaxial Graphene. Let us now move to the Raman analysis of strain^{52,53} induced by the temperature-dependent change in the lattice constant. For epitaxial graphene on Ir, the thermal expansion of graphene essentially follows the substrate.⁵⁴ The nonlinearity in T of the thermal expansion coefficient $\alpha(T)$ of iridium must be taken into account.^{55,56} To accurately describe the expansion of the Ir substrate in the temperature range explored (5 K–300 K),

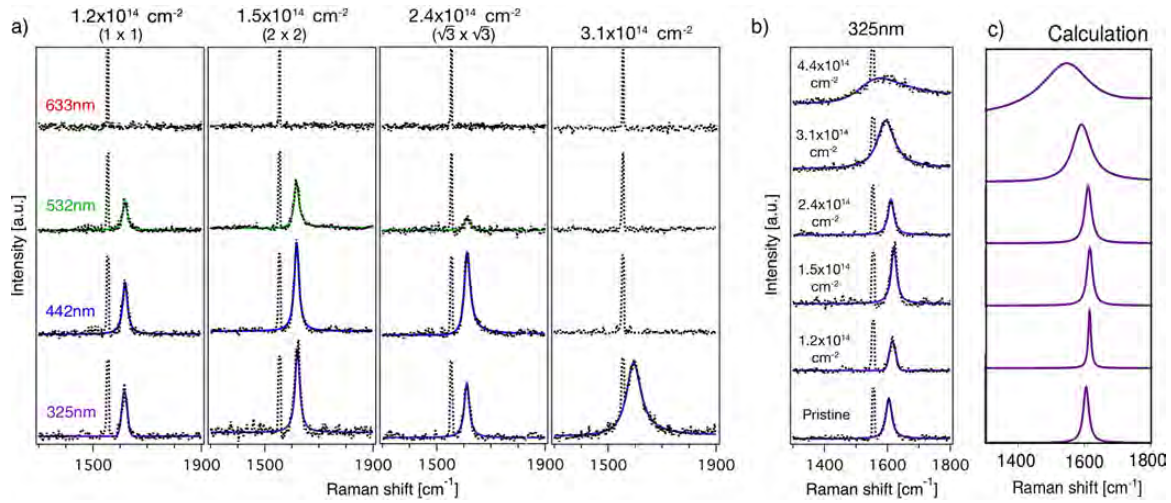


Figure 3. (a) Ultra-high vacuum (UHV) Raman spectra of Cs doped epitaxial graphene/Ir(111) with increasing carrier concentration from left to right measured by four laser lines. The raw data (dots) of the Raman G band together with a Fano line shape fit are shown. (b) UHV ultraviolet Raman spectra of doped graphene with increasing carrier concentration measured with 325 nm excitation. All Raman spectra are taken at $T = 5$ K and a vacuum better than 2×10^{-10} mbar. (c) Calculated Raman spectra for 325 nm light excitation and identical carrier concentrations as in panel b.

we fit $\alpha(T)$ to literature values^{55,56} and calculate the expansion as $l'/l = \exp(\int \alpha(T) dT)$. Here l' and l are the lattice constants at temperatures corresponding to the upper and lower border of the integral, respectively. For describing the Ir lattice expansion of the present experiment, the integral above is taken from $T = 5$ K to $T = 300$ K. The strain ϵ in percent is calculated as $100(l'/l - 1)$ yielding $\epsilon = 0.134\%$. The phonon downshift corresponding to ϵ is given by $\Delta\omega = -2\omega_0\gamma\epsilon$ (see ref 57 and references therein). Here $\gamma = 1.99$ (ref 57) is the Grüneisen parameter of the doubly degenerate G phonon mode of graphene, $\omega_0 = 1606.5 \text{ cm}^{-1}$ is the phonon frequency at 5 K. These values yield a strain induced downshift of the G band phonon when going from 5 to 300 K of $\Delta\omega = -8.6 \text{ cm}^{-1}$, which is in excellent agreement to the experimental value of $\Delta\omega = -10.7 \text{ cm}^{-1}$.

Raman Spectrum of Cs Doped Graphene/Ir(111). We have used a Fano line shape^{30,36,58,59} to fit the G band Raman spectra for all doping levels by

$$F(\omega) = I_0 \frac{\left(1 + \frac{\omega - \omega_0}{\gamma/2}\right)^2}{1 + \left(\frac{\omega - \omega_0}{\gamma/2}\right)^2} \quad (1)$$

Here I_0 is the Raman intensity, ω_0 the line position, γ the full-width at half-maximum, and $1/q$ the asymmetry (or Fano) factor, which describes the strength of the interference effect between the discrete and continuous spectra. For $1/q = 0$, we have a Lorentzian line shape indicating no interference effect. In the following, we analyze the carrier concentration dependence of I_0 , ω_0 , γ , and $1/q$. Figure 3a illustrates that, upon evaporation of Cs onto the sample, the observed Raman spectra dramatically change compared to those of pristine graphene. For the first deposition of Cs, all laser energies except the red laser (633 nm) yield a finite Raman intensity. We attribute the appearance of a Raman signal to removal of the hybridization of the graphene and Ir states as discussed in

the ARPES section. From Figure 3a, we observe that the Raman intensity almost vanishes for the green (532 nm) laser at a carrier concentration of $2.4 \times 10^{14} \text{ cm}^{-2}$ (corresponding to the $\sqrt{3} \times \sqrt{3}$ phase). The Raman intensity for the blue laser (442 nm) vanishes at a doping level of $3.1 \times 10^{14} \text{ cm}^{-2}$. On the other hand, the UV laser (325 nm) yields a Raman spectrum up to the highest doping level. This can be understood in terms of the condition that light can only induce transitions across the Dirac cone between occupied states in the valence band and unoccupied states in the conduction band. If doping shifts the Fermi level deep into the conduction band, these transitions are forbidden by Pauli blocking. The UV laser always fulfills the resonance condition $2E_F < E_{\text{laser}}$ since its laser energy ($E_{\text{laser}} = 3.8 \text{ eV}$) is significantly higher than twice the maximum Fermi level shift ($E_F = 1.58 \text{ eV}$ from the ARPES data of maximally doped graphene).

Figure 3a also reveals that the Raman spectrum taken with the lowest photon energy for each doping level becomes Fano-like. This applies to the 532 nm (green) laser for $1.5 \times 10^{14} \text{ cm}^{-2}$, the 442 nm (blue) laser for $2.4 \times 10^{14} \text{ cm}^{-2}$, and the UV laser for $3.1 \times 10^{14} \text{ cm}^{-2}$. The most striking feature is that the Fano tail of the present data is toward higher wavenumber with respect to the peak position. This corresponds to a positive sign of $1/q$. The origin of this unusual Fano line shape will be explained in the next section. In Figure 3b, we show UV Raman spectra with increasing carrier concentration. The position of the G peak shifts toward higher phonon energies for carrier concentrations up to $1.5 \times 10^{14} \text{ cm}^{-2}$ before it shifts down. The UV Raman spectrum allows for comparison of the G line position of pristine (1606.3 cm^{-1}), weakly doped graphene (1615.9 cm^{-1} for the lowest Cs deposition), and fully doped graphene (1550.0 cm^{-1}). A key to understanding the present results is the interference of the electronic and vibrational Raman, which also plays a major role in explaining the Fano asymmetry in carbon nanotubes.²⁸ Here we apply this theory³⁰ using the experimental band structure of graphene derived from ARPES measurements. The calculated Raman

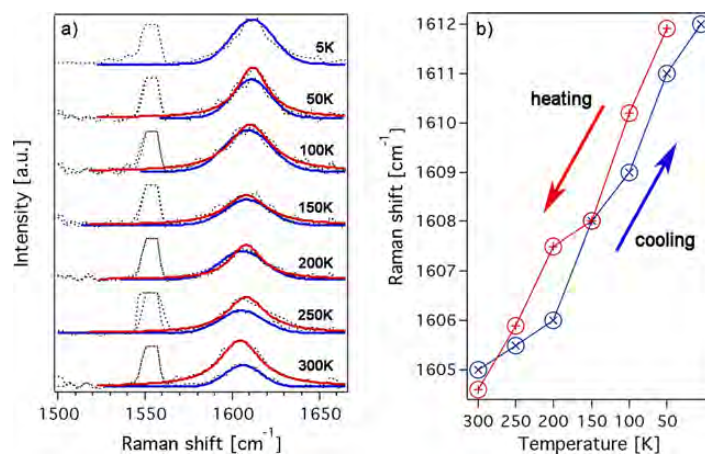


Figure 4. (a) Temperature dependent Raman spectra of the $\sqrt{3} \times \sqrt{3}$ phase of Cs doped graphene for cooling (blue line) and warming-up (red line). (b) Raman peak positions as a function of temperature.

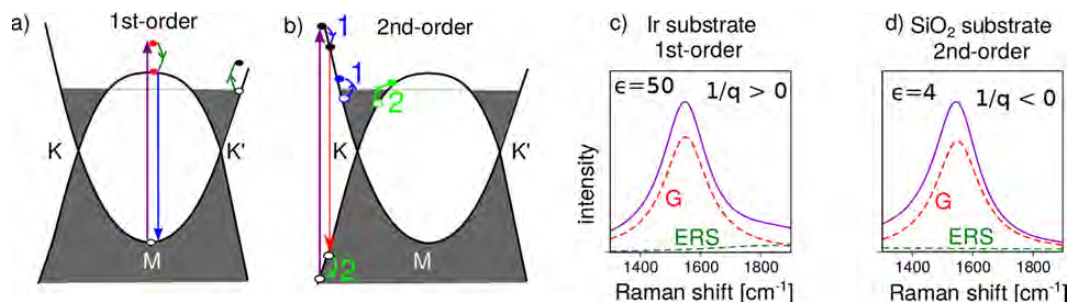


Figure 5. (a) In the first-order electronic Raman scattering (ERS) process, an electron is excited to a virtual state above the saddle-point energy and then relaxes via Coulomb interaction by exciting an e-h pair. When the electron recombines with the hole, the scattered energy is resonant to the M point energy. (b) In the second-order ERS process, the photoexcited e-h pair occupies a real state. The electron and hole relax to lower energy states by exciting two e-h pairs near Fermi surface with opposite momenta. Calculated Raman spectra of highly doped-graphene on (c) Ir substrate and (d) SiO_2 substrates. The dashed lines indicate the spectral contributions of the vibrational Raman scattering by the G phonon and ERS. The solid line is the spectrum after considering interference between these two contributions.

spectra are depicted in Figure 3c and a very good agreement regarding the position and Fano asymmetry can be seen. In the following section, we will show a quantitative comparison between experiment and theory regarding the position and asymmetry of the G band and discuss the details of the Raman calculation. Let us now look to the temperature dependent Raman spectra of doped graphene. This is motivated by question if intercalation of Cs liberates graphene from the substrate so that it does not follow any more the lattice constant of Ir. The corresponding Raman spectra and the G band positions are shown in Figure 4. An upshift of the G band position by 7 cm^{-1} with decreasing temperature (from 300 to 5 K) is found. This is within the experimental accuracy to what we observed in Figure 2 for pristine graphene/Ir. Thus, despite Cs is intercalated in between graphene and Ir(111), the graphene still follows the compression of the underlying Ir substrate.

Discussion. Electronic Raman Scattering. In the electronic Raman scattering, the photoexcited electron and hole couple to electronic excitations via the Coulomb interaction and can generate one or more electron-hole pairs. The large density of states in heavily doped graphene around the M point

enhances the cross-section for electronic Raman scattering. In Figure 5a and b, we graphically depict the relaxation processes, which we consider in the calculation. We consider first-order (creation of one electron-hole pair) and second-order (creation of two electron-hole pairs) processes. The Coulomb interaction is affected by the dielectric screening of the substrate, which is strong for the Ir substrate ($\epsilon = 50$).⁶⁰ As a consequence, only the first-order process (wavevector $\mathbf{q} = 0$) is dominant for Ir. This is depicted in Figure 5c. We note that this first-order process excites an intraband electron-hole pair whose Coulomb interaction is maximum at wavevector $\mathbf{q} = 0$. This process is completely different from the interband electron-hole pair excitation in the low doping regime, in which the direct Coulomb interaction vanishes at $\mathbf{q} = 0$.³¹

Interference between the first-order ERS (shown by the green line) and the G band (red line) produces the asymmetric Fano line shape toward larger wavenumber ($1/q > 0$). Figure 5d depicts the simulated Raman spectra of highly doped graphene on SiO_2 substrate. Because of the relatively weak screening effect ($\epsilon = 4$), the second-order Raman ($\mathbf{q} \neq 0$) process overcomes the first-order process thanks to the double resonant effect. The resulting Raman spectra are asymmetric

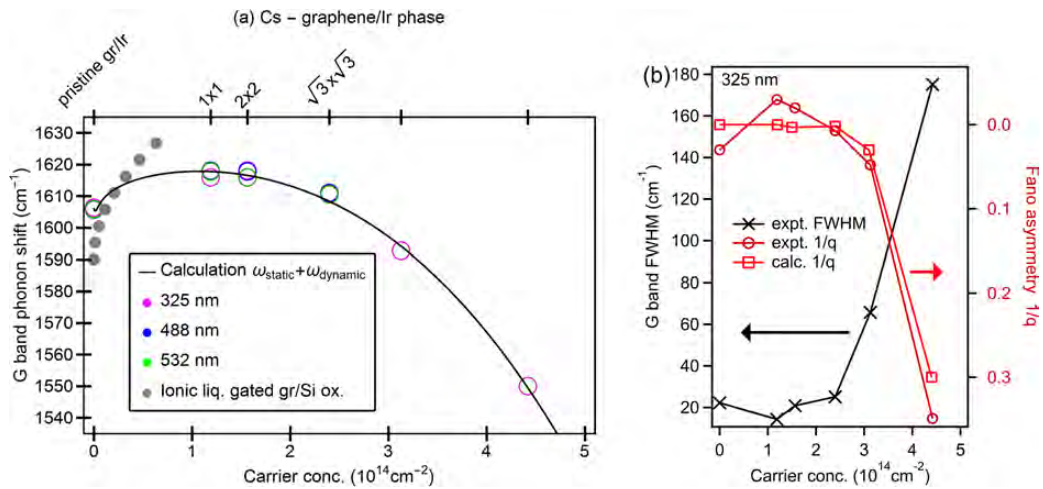


Figure 6. (a) Raman G peak positions of Cs doped graphene versus the carrier concentration. The full line is a model calculation of the G band frequency (see Methods section) and open circles are the experimentally determined G band maxima. The gray filled circles indicate the G peak position from ionic liquid gated graphene on fused silica (ref 15). (b) Crosses connected by a black line: expt. line width (full width at half-maximum) of the Raman G peak. Circles connected by a dark red line: the experimental Fano asymmetry factor obtained from measurements with the UV ($\lambda = 325$ nm) laser. The squares connected by a red line are the calculated values of the Fano asymmetry (obtained by fitting a Fano line to the calculated spectra in Figure 3c).

toward the lower wavenumber ($1/q < 0$). The spectra reported for doped graphene on Si have the Fano tail toward low wavenumbers^{27,36,37} corresponding to negative values of $1/q$. Our calculated results can thus fully explain the present data on Ir and the literature data on silicon wafers and other insulators.

G Band Position: Experiment and Theory. In Figure 6a, we show plots of the experimental G band positions versus carrier concentration and along with a calculation of the phonon energy shift with carrier concentration. We quantitatively describe the observed Raman G band shifts by considering the effects of phonon renormalization and lattice expansion.⁵ Our model is based on expressing the doping induced change of the Raman G band frequency $\Delta\omega$ as a sum of static (lattice expansion) and dynamic (electron-phonon coupling) effects as $\Delta\omega = \alpha\omega_{static} + \omega_{dynamic}(D^2)$ (ref 5). Here α is a parameter that describes the scaling of the theoretical doping dependence for freestanding graphene due to the effects of the Ir substrate. We have shown in Figure 2 (temperature dependence) that the lattice constant of graphene perfectly follows the Ir substrate. Because of the strong interaction, graphene's expansion due to doping will also be affected and hence $\alpha \neq 1$. D^2 is the deformation potential as explained in the ARPES section. The equations for ω_{static} and $\omega_{dynamic}$ are given in the Methods section. Using the ARPES-derived value of $D^2 = 63.1$ eV²/Å², we proceed to perform the fit of the parameter α describing the lattice expansion versus carrier concentration. We find $\alpha = 0.18$, which would suggest there is still compressive strain, that is, the lattice constant of freestanding graphene doped to an equal concentration would be larger. Let us discuss these results for D^2 and α in more detail. First, the experimental value of D^2 is considerably larger than the DFT value of $D^2 = 45.6$ eV²/Å² (ref 5). A perfect agreement between theory and experiment is achieved by GW calculations, which yield $D^2 = 62.8$ eV²/Å² (ref 61). This can be understood by the fact that the underlying electron and phonon dispersions of graphene are accurately described only by GW calculations and DFT

underestimates the size of the electron and phonon dispersions.⁶¹ Regarding the dependence of the $\alpha\omega_{static}$ term that describes the lattice expansion on carrier concentration, we estimate from Figure 6a that the observed maximum G band frequency downshift from undoped graphene is ~ 50 cm⁻¹. Assuming that 69 cm⁻¹ downshift of the G band phonon corresponds to 1% expansive strain (ref 57), we estimate a C-C bond increase of 0.8%. Indeed, this is close to what has been observed by diffraction in intercalated graphite where the C-C bond length increases from 1.4211 Å (pristine graphite) to 1.4320 Å (stage 1 GIC)⁶² corresponding to a 0.7% increase in the lattice constant. The small differences to the present case could be ascribed to the higher doping level that we have achieved in the present case corresponding to a shift of the charge neutrality point to $E_D = 1.58$ eV, whereas the stage 1 KC₈ GIC has $E_D = 1.35$ eV.⁶³ Interestingly, the theoretically expected downshift for the carrier concentrations achieved is much larger, which is described by $\alpha = 0.18$. We attribute this to two effects. First, the substrate interaction is strong despite Cs is intercalated in between graphene and the substrate. This is evident from the temperature dependent Raman spectra of the $\sqrt{3} \times \sqrt{3}$ phase where the C-C lattice constant is following the Ir substrate. It is clear that the substrate interaction can hinder the lattice expansion, which would result in $\alpha < 1$, as we have observed. Additionally, substrate interaction can cause the formation of wrinkles. Second, regarding the very large difference between experiment and theory, the analytical expression for ω_{static} is derived from DFT calculations and perhaps not sufficiently accurate to describe the very high doping levels considered here.⁵

Next, let us discuss how our observed G band shift corresponds to experiments performed with ionic liquid gated graphene (data from ref 15). These data are shown in Figure 6a along with our experiments. The ionic liquid gated graphene on Si oxide has a maximum upshift of 25 cm⁻¹ (ref 15), whereas the observed maximum G band upshift of Cs

Nano Letters

Letter

doped graphene on Ir is about 10 cm^{-1} . Notably, Rb doped graphene on Si oxide also displayed a maximum upshift of the G band by 25 cm^{-1} (ref 37) and it could therefore be related to the substrate. We believe that the observed differences in the slope of the G band with doping lie in the phonon dispersion relation of graphene on insulators and on metals. It has been put forward, that for graphene on metals, the Kohn anomalies at Γ and K points are screened by the metal substrate.⁶⁴ High resolution electron energy loss spectroscopy measurements and calculations of the phonon dispersion relations of the graphene/Ir(111) system⁶⁵ indicate that the Kohn anomaly at Γ is not as strongly kinked than in freestanding graphene. This results in a higher phonon frequency for graphene/Ir(111) compared to freestanding graphene. Upon doping, the Kohn anomaly at Γ point shifts away to a finite wavevector equal to $2k_F$ (k_F is length of the Fermi wavevector) and the Γ point phonon frequency moves to higher values. Thus, for graphene on Ir, the upshift in phonon energy as a result of doping is smaller than the one observed for freestanding graphene. These arguments explain the experimental data of graphene/Ir(111) and graphene/Si oxide shown in Figure 6a.

Doping Dependence of Fano Asymmetry and Spectral Line Width. Figure 6b depicts the experimental and theoretical Fano asymmetry parameter $1/q$ and the experimental spectral width (fwhm) as a function of carrier concentration. The values of Fano asymmetry $1/q$ and the fwhm at carrier concentrations larger than $3 \times 10^{14}\text{ cm}^{-2}$ exhibit a strong deviation from the behavior at lower carrier concentrations. Correlating this with the experimental Fermi surfaces from ARPES, we attribute the sudden increase in $1/q$ and line width to increased electronic Raman scattering as the Lifshitz transition is approached. This is not only via the large carrier concentration which causes the downshift of the G band position, but also via the change in the energy-momentum conservation for electron-hole pair excitation affecting the Fano line shape of the G band as theoretically predicted.³⁰

Conclusions and Outlook. In conclusion, we have established a fully experimental relation between energy shift and Fano asymmetry parameter of the Raman G band versus carrier concentration in doped epitaxial graphene. This is based on ARPES experiments that reveal the deformation potential D^2 from the kink feature and Raman measurements on identical samples. This relation is expected to be useful for future stand-alone UHV Raman experiments. In the Raman experiments, we have exploited the band renormalization upon doping, which reduces the optical transition energy at the saddle point. This allowed us to achieve resonance Raman conditions with UV light in the vicinity of the van Hove singularity. We have observed a peculiar Fano line shape with an asymmetry tail toward high Raman shifts. This is opposite to what is known for doped graphene on semiconductors such as Si oxide. By performing resonant Raman calculations, we have fully explained this behavior by considering first and second-order electronic Raman contributions.

Our work has introduced UV UHV Raman spectroscopy as a function of temperature as a versatile tool for surface science of two-dimensional materials. Let us now consider two future research directions. First, the presented approach could also be applied to hole doped graphene. Theoretically, we expect it to yield qualitatively similar results if the Fermi level reaches the van-Hove singularity in the valence band. Hole doping of graphene on Ir(111) has already been achieved by oxygen intercalation⁶⁶ or chlorine intercalation⁶⁷ and it would be

interesting to investigate such samples by UHV Raman spectroscopy at low temperatures. Second, UHV Raman spectroscopy of alkali doped graphene could be used for investigation of the superconducting properties of graphene analogous to previous experiments that are carried out on superconducting bulk CaC_6 (ref 68). In these experiments, a sharp superconducting coherence peak is observed by Raman at 24 cm^{-1} , which is very close to the value for the superconducting gap obtained by scanning tunneling spectroscopy (25.8 cm^{-1}), highlighting that this Raman peak has its origin in the superconducting phase.⁶⁸ For graphene, electronic Raman scattering from the superconducting phase has not been observed yet. It should also lead to low-energy Raman peaks with an energy roughly equal to the size of the superconducting gap.⁶⁹ Theory predicts that this holds for both, *s*-wave and *d*-wave superconducting graphene at doping levels close to what is shown in the present work.⁷⁰ The Raman intensity of these low-energy peaks has been estimated to be approximately a factor 1000 lower than the G band intensity.⁶⁹ Given, the comparably low Raman intensity of graphene on metals with respect to graphene on insulators, we estimate that the electronic Raman peaks at low wavenumber will be hard to measure for the present graphene/Ir(111) system. An approach for addressing this problem is to carry out the present experiment with graphene transferred onto an insulating substrate. The large Raman response of graphene on insulators compared to graphene on metals could be a key to measure the appearance of low wavenumber Raman peaks when the temperature is below T_c . Thus, a future experiment could be to perform doping graphene into the superconducting state after it is transferred onto an insulator. Having doped graphene on an insulator inside UHV would in principle also allow for electrical transport characterization. To that end, the presented UHV Raman setup can be extended via electrical feedthroughs into the UHV chamber. In such a setup, the Raman spectrum and the four-point resistance could be measured simultaneously as a function of alkali doping. This could provide strong evidence for the existence of a superconducting phase and elucidate its Raman response. Finally, such a work could also be extended to doped bilayer graphene with a relatively higher critical temperature²¹ and doped heterostructures composed out of different van der Waals materials.

Methods. Synthesis. Graphene/Ir(111) has been synthesized in situ in the preparation chamber attached to the UHV Raman system using an established recipe⁷¹ that yields monolayer coverage by a self-limiting process.⁷² The fact that we have monolayer graphene is supported by three techniques: ARPES, STM, and LEED. ARPES spectra show only one π valence band. A bilayer, for example, would show two π valence bands. We have also verified that the full Ir(111) is covered by monolayer graphene via scanning the spot of the ARPES measurement (spotsize: $100 \times 50\text{ }\mu\text{m}^2$) over the full $1 \times 1\text{ cm}^2$ Ir(111) crystal. We have nowhere found two valence bands that would hint bilayer formation. The STM images that we took of samples prepared in that way (Supporting Information Figure S4) show the moiré pattern due to substrate interaction. This moiré pattern is a clear proof of monolayer coverage. Also, the individual carbon atoms of the monolayer are clearly seen. Finally, the LEED shown in Figure S2 of the Supporting Information displays the diffraction spots due to the moiré pattern of monolayer graphene/Ir(111). The Ir(111) single crystal, which was used as a substrate for the

Nano Letters

Letter

graphene synthesis that was first sputtered (1 keV) in Ar atmosphere (1×10^{-6} mbar), followed by an annealing step under O_2 flow (1×10^{-7} mbar) at 1200°C for 30 min. After the crystal cooled down to room temperature a rapid flashing to 1700°C provided a clean surface indicated by a sharp hexagonal LEED pattern. For the graphene synthesis, we used a combination of CVD (chemical vapor deposition) and TPG (temperature-programmed growth). Hereby, propene (C_3H_6) was dosed into the UHV chamber (1×10^{-6} mbar) for 60 s at room temperature to adsorb molecules on the iridium surface followed by a flashing step to 1250°C for 3 min without propene to create graphene islands with the same crystallographic orientation as the substrate. The TPG synthesis was applied twice to increase the amount of graphene islands. After the second TPG step, the sample was not cooled down to room temperature but only to 900°C . After reaching this temperature, the CVD growth was carried out. Hereby, propene was dosed (1×10^{-6} mbar) for 15 min to grow graphene in the areas between the islands creating a closed monolayer of graphene without rotational domains with respect to iridium. Finally, the sample was cooled down slowly to room temperature to minimize the formation of wrinkles. Cs was deposited by evaporation from a commercial SAES getter source. The evaporated amount of Cs was calibrated by a quartz crystal microbalance. The amount of evaporated Cs monolayer reported in the paper are with respect to the bulk Cs structure.

Angle-Resolved Photoemission Spectroscopy. ARPES was performed at the BaDElPh beamline⁷³ of the Elettra synchrotron in Trieste (Italy) with linear s- and p-polarization at $h\nu = 31$ eV at a temperature of 20 K. The graphene/Ir(111) samples were prepared in situ and measured in a vacuum better than 5×10^{-11} mbar. Immediately after the synthesis, Cs deposition was carried out in an ultra-high vacuum (UHV) chamber from SAES getters with the sample at RT. We performed stepwise evaporation of Cs, which we monitored by ARPES measurements of the band structure. Cs evaporation was stopped after the desired doping level was reached.

Scanning Tunneling Spectroscopy and Microscopy. STM and STS are carried out with a background pressure lower than 10^{-11} mbar. The constant energy maps are recorded using the lock-in technique with a modulation frequency of 833.1 Hz and a modulation amplitude of 8 mV, providing an energy resolution of 14 meV. An etched tungsten tip is used for all measurements, which is prepared in situ by applying positive or negative voltage pulses up to 10 V. Fourier transformed images are obtained from spectroscopic maps by using the fast Fourier transform of the SPIP software⁷⁴ with Hanning window. Subsequently, the symmetry of the sample is exploited to enhance the signal-to-noise ratio.

Ultra-high Vacuum Raman Spectroscopy. UHV Raman measurements were performed in the backscattering geometry using commercial Raman systems (Renishaw) integrated in a home-built optical chamber,⁷⁵ where the exciting and Raman scattered light were coupled into the vacuum using a 50-times long-working distance microscope objective with an NA of ~ 0.4 and a focal distance of 20.5 mm for lasers with wavelength 442 nm, 532 nm, and 633 nm. For the UV laser, UV compatible optical elements have been used. The 20 \times UV objective has a focal distance equal to 13 mm and an NA = 0.32. A sketch of our experimental setup is shown in the Supporting Information. The laser powers used were ~ 2 mW for the UV laser and 9 mW, 25 mW and 45 mW for blue, red,

and green lasers, respectively. Assuming that this energy gets spread over $\sim 4 \mu\text{m}^2$, we obtain power densities in the range of 100 kW/cm^2 . Using liquid He cooling and given the fact that graphene is directly on a metal, these laser powers result in a linear dependence of Raman intensity to the laser power. The position of the laser on the sample could be checked by a camera in the laser path. All spectra have been calibrated in position and intensity to the O_2 vibration at 1555 cm^{-1} (ref 76). O_2 Raman peaks can be seen with all laser lines used in the present experiment which is consistent with the previous published works.^{76,77} Further precautions that we took to prevent laser heating induced effects is a study of the laser power dependence (see Supporting Information).

Calculations of Raman spectra. Calculations of Doping Dependent Phonon Shift. We have calculated the Raman shift $\Delta\omega = \alpha\omega_{\text{static}} + \omega_{\text{dynamic}}(D^2)$ according to the well-established model.⁵ The frequency downshift due to doping induced lattice expansion is described by ω_{static} . The parameter α is a scaling factor for the phonon downshift with respect to the calculated doping dependence of freestanding graphene. The frequency upshift is described by $\omega_{\text{dynamic}}(D^2)$. Here D^2 is the deformation potential. For ω_{static} we use the equation for freestanding graphene (ref 5):

$$\omega_{\text{static}} = -2.13\sigma - 0.0360\sigma^2 - 0.00329\sigma^3 - 0.226|\sigma|^{3/2} \quad (2)$$

Here σ is the charge carrier density per cm^2 and ω_{static} is given in cm^{-1} . For calculation of the dynamic contribution, we need to consider

$$\tilde{F}_q^{\epsilon_f}(\omega) = \frac{2}{N} \sum_{\mathbf{k}, n \neq m} \frac{D^2(\tilde{f}_{\mathbf{k}m} - \tilde{f}_{\mathbf{k}n})}{\epsilon_{\mathbf{k},m} - \epsilon_{\mathbf{k},n} + \hbar\omega + i\delta} \quad (3)$$

Here the sum goes over all points in the 2D BZ and $\tilde{f}_{\mathbf{k}m} = \tilde{f}(\epsilon_{\mathbf{k}m} - \epsilon_f)$ with \tilde{f} being the Fermi distribution function. For numerical integration, we have used a trigonal grid having ~ 1000 points in the 2D BZ of graphene. $\hbar\omega$ is the phonon energy of the undoped system and $\delta = 10$ meV a small broadening term. For the band structure calculations, we have used a third nearest neighbor tight-binding fit to the experimental ARPES band structure.⁴⁶ The corresponding dynamic shift is calculated by

$$\omega_{\text{dynamic}} = \text{Re} \left[\frac{\tilde{F}_0^{\epsilon_f}(\omega_0) - \tilde{F}_0^0(\omega_0)}{2M\omega_0} \right] \quad (4)$$

Here M is the free electron mass, ω_0 the unperturbed phonon frequency of the G band, and $\tilde{F}_0^{\epsilon_f}$ is defined in eq 3. In the calculations, we used an artificially high temperature of $T = 400$ K in the Fermi distribution function as a means to describe doping inhomogeneities and charge puddles that can not be resolved spatially. A similar observation was made in previous works that have also used artificially high temperatures³⁷ or Fermi level smearing.¹⁶

Raman Intensity Calculation. We consider the interference between the G band phonon Raman and ERS pathways and write the Raman intensity as

$$I(\omega_s) = [A_G(\omega_s) + A_{\text{ERS}}(\omega_s)]^2 \quad (5)$$

where $A_G = \sum_\nu A_\nu$ is the G phonon scattering amplitude, which consists of zone center (Γ point) $\nu = \text{LO}$ and iTO modes, and A_{ERS} is the ERS scattering amplitude. The phonon Raman process consists of (1) excitation of an electron-hole pair by

Nano Letters

Letter

the electron–photon interaction, (2) phonon emission by means of the electron–phonon interaction, and (3) electron–hole recombination and photoemission by the electron–

photon interaction. On the basis of the three subprocesses, phonon scattering amplitude is given by⁷⁸

$$A_\nu(E_s) = \sum_{\mathbf{k}} \frac{M_{\text{op}}^{\text{vc}}(\mathbf{k})M_{\text{ep}}^{\text{v}}(\mathbf{k}, \mathbf{k})M_{\text{op}}^{\text{cv}}(\mathbf{k})[f(E_{\mathbf{k}}^{\text{v}}) - f(E_{\mathbf{k}}^{\text{c}})]}{[E_{\text{L}} - E_{\mathbf{k}}^{\text{cv}} - i\gamma/2][E_{\text{L}} - E_{\mathbf{k}}^{\text{cv}} - \hbar\omega^{\text{v}} - i(\gamma + \Gamma_{\text{v}})/2][E_{\text{L}} - \hbar\omega^{\text{v}} - E_s - i\Gamma_{\text{v}}/2]} \quad (6)$$

Here E_{L} is the laser energy, E_s is the scattered photon energy, $E_{\mathbf{k}}^{\text{cv}} = E_{\mathbf{k}}^{\text{c}} - E_{\mathbf{k}}^{\text{v}}$ is the electron energy difference between the conduction (c) and the valence (v) bands at a wave vector \mathbf{k} . The energy bands of graphene have been obtained by the tight-binding (TB) fits to the experimental band structure considering up to the three nearest-neighbors for each of doping level. The M_{op} and M_{ep}^{v} are the electron–photon and electron–phonon matrix elements, respectively. These matrix elements are obtained within the TB method.^{79,80} The phonon frequency of the ν th mode is depicted by ω^{v} and a broadening factor of the photoexcited carriers $\gamma = 0.2$ eV is used. The

phonon line width Γ_{v} is fitted to the Raman measurements. The summation of states considered in eq 6 are taken below a cutoff energy $E_{\mathbf{k}}^{\text{v}} = 5$ eV. For the ERS amplitude A_{ERS} , we consider the lowest order processes as shown in Figure 5. In the first-order ERS, the photoexcited carrier excites an electron–hole (e–h) pair via Coulomb interaction with zero momentum transfer ($\mathbf{q} = 0$) or vertical transition. We note that the e–h pair is allowed to occupy a virtual state as the lifetime of Coulomb interaction is very short (~ 10 fs). The first order ERS amplitude is given by

$$A_{\text{ERS}}^{(1)}(E_s) = \sum_{\mathbf{k}} \sum_{\mathbf{k}'} \frac{M_{\text{op}}^{\text{vc}}(\mathbf{k})K_{\mathbf{k}, \mathbf{k}' \text{ c}, \mathbf{k}, \mathbf{k}' \text{ c}}(0)M_{\text{op}}^{\text{cv}}(\mathbf{k})[f(E_{\mathbf{k}}^{\text{v}}) - f(E_{\mathbf{k}}^{\text{c}})]}{[E_{\text{L}} - E_{\mathbf{k}}^{\text{cv}} - i\gamma/2][E_{\text{L}} - E_{\mathbf{k}}^{\text{cv}} - E_{\mathbf{k}'}^{\text{c}} - i(\gamma + \Gamma_{\text{e}})/2][E_{\text{L}} - E_{\mathbf{k}'}^{\text{c}} - E_s - i\Gamma_{\text{e}}/2]} \quad (7)$$

where $E_{\mathbf{k}}^{\text{c}}$ and $\Gamma_{\text{e}} = 60$ meV are the energy of the excited e–h pair and the Coulomb scattering rate, respectively. If $E_{\text{L}} > E_{\text{M}}$ (here E_{M} is the M point transition energy), we expect that the photoexcited electron relaxes to the conduction band at the M point. In such a way, we estimate $E_s = E_{\text{M}} - E_{\text{ex}}$, where E_{ex} is the exciton binding energy, estimated to be 100 meV. For $E_{\text{L}} < E_{\text{M}}$, we expect hot luminescence,¹⁵ that is, the photoexcited carrier relaxes to the lowest intermediate energy $\sim 2E_{\text{F}}$ and then recombines with the hole by emitting $E_s \approx 2E_{\text{F}}$. The direct Coulomb interactions between two electrons for initial states 1,2 with states 3,4 is given by $K_{1,2,3,4}(\mathbf{q})$. In the TB approximation, this kernel is expressed as

$$K_{1,2,3,4}(\mathbf{q}) = \sum_{ss'=A,B} C_s^1 C_s^2 C_{s'}^{*3} C_{s'}^{*4} \nu(\mathbf{q})/\epsilon \quad (8)$$

Here C_s^i is the TB coefficient for the atomic site s at the state i and $\nu(\mathbf{q})$ is the Fourier transform of the Ohno potential.⁸¹ ϵ is the dielectric constant of the substrate. Because the Raman shift of the ERS process is about 0.2 eV, we do not consider the dynamical screening effect. For the second-order ERS, we consider the excitation of two e–h pairs by the photoexcited electron and hole [Figure 5b]. The amplitude of the second-order ERS process is given by

$$A_{\text{ERS}}^{(2)}(E_s) = \sum_{\mathbf{k}} \sum_{\mathbf{k}' \mathbf{q}} \frac{M_{\text{op}}^{\text{vc}}(\mathbf{k})K_{\mathbf{k}(\mathbf{k}+\mathbf{q})\text{ v}, \mathbf{k}' \text{ c}, \mathbf{k}, \mathbf{q} \text{ v}, \mathbf{k}'+\mathbf{q} \text{ c}}(-\mathbf{q})}{[E_{\text{L}} - E_{\mathbf{k}}^{\text{cv}} - i\gamma/2][E_{\text{L}} - E_{\mathbf{k}}^{\text{cv}} - E_{\mathbf{k}'}^{\text{c}} - E_{\mathbf{k}'}^{\text{v}} - i(\gamma + 2\Gamma_{\text{e}})/2]} \times \frac{K_{\mathbf{k}, \mathbf{k}' \text{ c}, (\mathbf{k}+\mathbf{q}) \text{ c}}(\mathbf{q})M_{\text{op}}^{\text{cv}}(\mathbf{k})[f(E_{\mathbf{k}}^{\text{v}}) - f(E_{\mathbf{k}}^{\text{c}})]}{[E_{\text{L}} - E_{\mathbf{k}}^{\text{c}} - E_s - i\Gamma_{\text{e}}/2][E_{\text{L}} - E_{\mathbf{k}'}^{\text{c}} - E_{\mathbf{k}'}^{\text{v}} - E_s - i2\Gamma_{\text{e}}/2]} \quad (9)$$

Here $E_{\mathbf{k}'}^{\text{v}} = E_{\mathbf{k}'}^{\text{c}} - \mathbf{q}$ and $E_{\mathbf{k}'}^{\text{v}} = E_{\mathbf{k}'}^{\text{c}} + \mathbf{q} - E_{\mathbf{k}}^{\text{v}}$ are the excitation energies of the e–h pairs.

■ ASSOCIATED CONTENT

S Supporting Information

The Supporting Information is available free of charge on the ACS Publications website at DOI: 10.1021/acs.nanolett.8b02979.

Sketch of UHV Raman experiment; LEED of 1×1 , 2×2 , $\sqrt{3} \times \sqrt{3}$, and overdoped Cs/graphene phases; ARPES of Cs doped graphene with carrier concentration $n = 4.4 \times 10^{14} \text{ cm}^{-2}$; STM and FT-STs of 2×2 and $\sqrt{3} \times \sqrt{3}$ phases; Raman G band spectra of Cs doped graphene measured with two different laser powers and after 3 h laser exposure (PDF)

■ AUTHOR INFORMATION

Corresponding Author

*E-mail: grueneis@ph2.uni-koeln.de.

ORCID

Niels Ehlen: 0000-0002-8581-8359
Boris V. Senkovskiy: 0000-0003-1443-6780
Alexander Fedorov: 0000-0002-9228-7082
Carsten Busse: 0000-0001-5522-0578
Luca Petaccia: 0000-0001-8698-1468
Alexander Grüneis: 0000-0003-2448-6060

Notes

The authors declare no competing financial interest.

■ ACKNOWLEDGMENTS

M.H., N.E., B.V.S., and A.G. acknowledge the ERC Grant No. 648589 ‘SUPER-2D’, funding from DFG projects A01 with CRC 1238 and GR 3708/2-1. A.G. acknowledges INST 216/808-1 FUGG, support from the ‘Quantum Matter and Materials’ (QM2) initiative, and support from Tohoku University for a research stay in Japan. The research leading to these results has received funding from the Horizon 2020 EC programme under Grant Agreement No. 730872 (CALIPSOplus). This work has been supported by the

Nano Letters

Letter

University of Cologne through the Institutional Strategy of the University of Cologne within the German Excellence Initiative. R.S. acknowledges MEXT KAKENHI (Nos. JP18H01810, JP15K21722).

REFERENCES

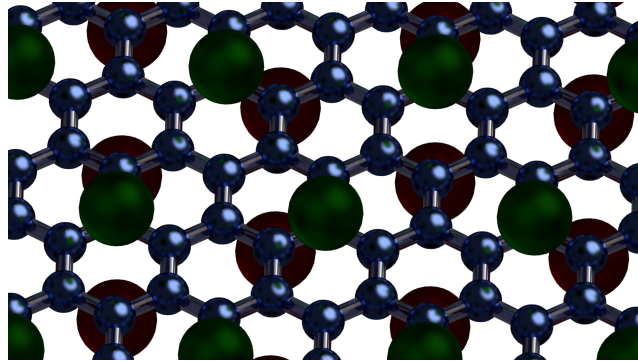
- (1) Ferrari, A. C.; Meyer, J. C.; Scardaci, V.; Casiraghi, C.; Lazzeri, M.; Mauri, F.; Piscanec, S.; Jiang, D.; Novoselov, K. S.; Roth, S.; Geim, A. K. *Phys. Rev. Lett.* **2006**, *97*, 187401.
- (2) Graf, D.; Molitor, F.; Ensslin, K.; Stampfer, C.; Jungen, A.; Hierold, C.; Wirtz, L. *Nano Lett.* **2007**, *7*, 238–242.
- (3) Saito, R.; Hofmann, M.; Dresselhaus, G.; Jorio, A.; Dresselhaus, M. S. *Adv. Phys.* **2011**, *60*, 413–550.
- (4) Ferrari, A. C.; Basko, D. M. *Nat. Nanotechnol.* **2013**, *8*, 235–246.
- (5) Lazzeri, M.; Mauri, F. *Phys. Rev. Lett.* **2006**, *97*, 266407.
- (6) Pisana, S.; Lazzeri, M.; Casiraghi, C.; Novoselov, K. S.; Geim, A. K.; Ferrari, A. C.; Mauri, F. *Nat. Mater.* **2007**, *6*, 198–201.
- (7) Bianchi, M.; Rienks, E. D. L.; Lizzit, S.; Baraldi, A.; Balog, R.; Hornekar, L.; Hofmann, P. *Phys. Rev. B: Condens. Matter Mater. Phys.* **2010**, *81*, No. 041403, DOI: [10.1103/PhysRevB.81.041403](https://doi.org/10.1103/PhysRevB.81.041403).
- (8) Haberer, D.; Petaccia, L.; Fedorov, A. V.; Praveen, C. S.; Fabris, S.; Piccinin, S.; Vilkov, O.; Vyalikh, D. V.; Preobrajenski, A.; Verbitskiy, N. I.; Shiozawa, H.; Fink, J.; Knupfer, M.; Büchner, B.; Grüneis, A. *Phys. Rev. B: Condens. Matter Mater. Phys.* **2013**, *88*, No. 081401, DOI: [10.1103/PhysRevB.88.081401](https://doi.org/10.1103/PhysRevB.88.081401).
- (9) Fedorov, A. V.; Verbitskiy, N. I.; Haberer, D.; Struzzi, C.; Petaccia, L.; Usachov, D.; Vilkov, O. Y.; Vyalikh, D. V.; Fink, J.; Knupfer, M.; Büchner, B.; Grüneis, A. *Nat. Commun.* **2014**, *5*, 4257.
- (10) Verbitskiy, N. I.; Fedorov, A. V.; Tresca, C.; Profeta, G.; Petaccia, L.; Senkovskiy, B. V.; Usachov, D. Y.; Vyalikh, D. V.; Yashina, L. V.; Eliseev, A. A.; Pichler, T.; Grüneis, A. *2D Mater.* **2016**, *3*, 045003.
- (11) Kleeman, J.; Sugawara, K.; Sato, T.; Takahashi, T. *J. Phys.: Condens. Matter* **2016**, *28*, 204001.
- (12) Usachov, D. Y.; Fedorov, A. V.; Vilkov, O. Y.; Ogorodnikov, I. I.; Kuznetsov, M. V.; Grüneis, A.; Laubschat, C.; Vyalikh, D. V. *Phys. Rev. B: Condens. Matter Mater. Phys.* **2018**, *97*, No. 085132, DOI: [10.1103/PhysRevB.97.085132](https://doi.org/10.1103/PhysRevB.97.085132).
- (13) Stampfer, C.; Molitor, F.; Graf, D.; Ensslin, K.; Jungen, A.; Hierold, C.; Wirtz, L. *Appl. Phys. Lett.* **2007**, *91*, 241907.
- (14) Das, A.; Pisana, S.; Chakraborty, B.; Piscanec, S.; Saha, S. K.; Waghmare, U. V.; Novoselov, K. S.; Krishnamurthy, H. R.; Geim, A. K.; Ferrari, A. C.; Sood, A. K. *Nat. Nanotechnol.* **2008**, *3*, 210–215.
- (15) Chen, C.-F.; Park, C.-H.; Boudouris, B. W.; Horng, J.; Geng, B.; Girit, C.; Zettl, A.; Crommie, M. F.; Segalman, R. A.; Louie, S. G.; Wang, F. *Nature* **2011**, *471*, 617–620.
- (16) Froehlicher, G.; Berciaud, S. *Phys. Rev. B: Condens. Matter Mater. Phys.* **2015**, *91*, 205413.
- (17) Efetov, D. K.; Kim, P. *Phys. Rev. Lett.* **2010**, *105*, 256805.
- (18) Ye, J.; Craciun, M. F.; Koshino, M.; Russo, S.; Inoue, S.; Yuan, H.; Shimotani, H.; Morpurgo, A. F.; Iwasa, Y. *Proc. Natl. Acad. Sci. U. S. A.* **2011**, *108*, 13002–13006.
- (19) Profeta, G.; Calandra, M.; Mauri, F. *Nat. Phys.* **2012**, *8*, 131.
- (20) Chapman, J.; Su, Y.; Howard, C. A.; Kundys, D.; Grigorenko, A. N.; Guinea, F.; Geim, A. K.; Grigorieva, I. V.; Nair, R. R. *Sci. Rep.* **2016**, *6*, 23254.
- (21) Ichinokura, S.; Sugawara, K.; Takayama, A.; Takahashi, T.; Hasegawa, S. *ACS Nano* **2016**, *10*, 2761–2765.
- (22) Nandkishore, R.; Levitov, L. S.; Chubukov, A. V. *Nat. Phys.* **2012**, *8*, 158–163.
- (23) Lifshitz, I. *Soviet Physics JETP* **1960**, *11*, 1130.
- (24) McChesney, J. L.; Bostwick, A.; Ohta, T.; Seyller, T.; Horn, K.; González, J.; Rotenberg, E. *Phys. Rev. Lett.* **2010**, *104*, 136803.
- (25) Mak, K. F.; da Jornada, F. H.; He, K.; Deslippe, J.; Petrone, N.; Hone, J.; Shan, J.; Louie, S. G.; Heinz, T. F. *Phys. Rev. Lett.* **2014**, *112*, 207401.
- (26) Yoon, D.; Jeong, D.; Lee, H.-J.; Saito, R.; Son, Y.-W.; Lee, H. C.; Cheong, H. *Carbon* **2013**, *61*, 373–378.
- (27) Jung, N.; Kim, B.; Crowther, A. C.; Kim, N.; Nuckolls, C.; Brus, L. *ACS Nano* **2011**, *5*, 5708–5716.
- (28) Farhat, H.; Berciaud, S.; Kalbac, M.; Saito, R.; Heinz, T. F.; Dresselhaus, M. S.; Kong, J. *Phys. Rev. Lett.* **2011**, *107*, 157401.
- (29) Ma, Y.; Kim, Y.; Kalugin, N. G.; Lombardo, A.; Ferrari, A. C.; Kono, J.; Imambekov, A.; Smirnov, D. *Phys. Rev. B: Condens. Matter Mater. Phys.* **2014**, *89*, 121402.
- (30) Hasdeo, E. H.; Nugraha, A. R. T.; Dresselhaus, M. S.; Saito, R. *Phys. Rev. B: Condens. Matter Mater. Phys.* **2014**, *90*, 245140.
- (31) Hasdeo, E. H. *Gate Modulated Raman Spectroscopy of Graphene*, Ph.D. thesis, Tohoku University, Dept. of Physics, 2016.
- (32) Eklund, P. C.; Subbaswamy, K. R. *Phys. Rev. B: Condens. Matter Mater. Phys.* **1979**, *20*, 5157–5161.
- (33) Dresselhaus, M. S.; Dresselhaus, G. *Adv. Phys.* **2002**, *51*, 1–186.
- (34) Kalbac, M.; Reina-Cecco, A.; Farhat, H.; Kong, J.; Kavan, L.; Dresselhaus, M. S. *ACS Nano* **2010**, *4*, 6055–6063.
- (35) Basko, D. M. *New J. Phys.* **2009**, *11*, 095011.
- (36) Howard, C. A.; Dean, M. P. M.; Withers, F. *Phys. Rev. B: Condens. Matter Mater. Phys.* **2011**, *84*, 241404.
- (37) Parret, R.; Paillet, M.; Huntzinger, J.-R.; Nakabayashi, D.; Michel, T.; Tiberj, A.; Sauvajol, J.-L.; Zahab, A. A. *ACS Nano* **2013**, *7*, 165–173.
- (38) Zhao, W.; Tan, P. H.; Liu, J.; Ferrari, A. C. *J. Am. Chem. Soc.* **2011**, *133*, 5941–5946.
- (39) Kanetani, K.; Sugawara, K.; Sato, T.; Shimizu, R.; Iwaya, K.; Hitosugi, T.; Takahashi, T. *Proc. Natl. Acad. Sci. U. S. A.* **2012**, *109*, 19610–19613.
- (40) Ludbrook, B. M.; Levy, G.; Nigge, P.; Zonno, M.; Schneider, M.; Dvorak, D. J.; Veenstra, C. N.; Zhdanovich, S.; Wong, D.; Dosanjh, P.; Straßer, C.; Stöhr, A.; Forti, S.; Ast, C. R.; Starke, U.; Damascelli, A. *Proc. Natl. Acad. Sci. U. S. A.* **2015**, *112*, 11795–11799.
- (41) Dombrowski, D.; Jolie, W.; Petrović, M.; Runte, S.; Craes, F.; Klinkhammer, J.; Kralj, M.; Lazić, P.; Sela, E.; Busse, C. *Phys. Rev. Lett.* **2017**, *118*, 116401.
- (42) Starodub, E.; Bostwick, A.; Moreschini, L.; Nie, S.; Gabaly, F. E.; McCarty, K. F.; Rotenberg, E. *Phys. Rev. B: Condens. Matter Mater. Phys.* **2011**, *83*, 125428.
- (43) Busse, C.; Lazić, P.; Djemour, R.; Coraux, J.; Gerber, T.; Atodiresei, N.; Caciuc, V.; Brako, R.; N'Diaye, A. T.; Blügel, S.; Zegenhagen, J.; Michely, T. *Phys. Rev. Lett.* **2011**, *107*, No. 036101, DOI: [10.1103/PhysRevLett.107.036101](https://doi.org/10.1103/PhysRevLett.107.036101).
- (44) Pletikosić, I.; Kralj, M.; Pervan, P.; Brako, R.; Coraux, J.; N'Diaye, A. T.; Busse, C.; Michely, T. *Phys. Rev. Lett.* **2009**, *102*, No. 056808, DOI: [10.1103/PhysRevLett.102.056808](https://doi.org/10.1103/PhysRevLett.102.056808).
- (45) Petrovic, M.; Srut Rakic, I.; Runte, S.; Busse, C.; Sadowski, J. T.; Lazić, P.; Pletikosić, I.; Pan, Z.-H.; Milun, M.; Pervan, P.; Atodiresei, N.; Brako, R.; Sokcevic, D.; Valla, T.; Michely, T.; Kralj, M. *Nat. Commun.* **2013**, *4*, 2772.
- (46) Grüneis, A.; Attacalite, C.; Wirtz, L.; Shiozawa, H.; Saito, R.; Pichler, T.; Rubio, A. *Phys. Rev. B: Condens. Matter Mater. Phys.* **2008**, *78*, 205425.
- (47) Hattab, H.; N'Diaye, A. T.; Wall, D.; Klein, C.; Jnawali, G.; Coraux, J.; Busse, C.; van Gastel, R.; Poelsema, B.; Michely, T.; Meyer zu Heringdorf, F.-J.; Horn-von Hoegen, M. *Nano Lett.* **2012**, *12*, 678–682.
- (48) Jean, F.; Zhou, T.; Blanc, N.; Felici, R.; Coraux, J.; Renaud, G. *Phys. Rev. B: Condens. Matter Mater. Phys.* **2013**, *88*, 165406.
- (49) Bronsgeest, M. S.; Bendiab, N.; Mathur, S.; Kimouche, A.; Johnson, H. T.; Coraux, J.; Pochet, P. *Nano Lett.* **2015**, *15*, 5098–5104.
- (50) Sánchez-Barriga, J.; Varykhalov, A.; Marchenko, D.; Scholz, M. R.; Rader, O. *Phys. Rev. B: Condens. Matter Mater. Phys.* **2012**, *85*, 201413.
- (51) Usachov, D. Y.; Davydov, V. Y.; Levitskii, V. S.; Shevelev, V. O.; Marchenko, D.; Senkovskiy, B. V.; Vilkov, O. Y.; Rybkin, A. G.; Yashina, L. V.; Chulkov, E. V.; Sklyadneva, I. Y.; Heid, R.; Bohnen, K.-P.; Laubschat, C.; Vyalikh, D. V. *ACS Nano* **2017**, *11*, 6336–6345.

Nano Letters

Letter

- (52) Frank, O.; Tsoukleri, G.; Riaz, I.; Papagelis, K.; Parthenios, J.; Ferrari, A. C.; Geim, A. K.; Novoselov, K. S.; Galiotis, C. *Nat. Commun.* **2011**, *2*, 255.
- (53) Mueller, N. S.; Heeg, S.; Alvarez, M. P.; Kusch, P.; Wassertho, S.; Clark, N.; Schedin, F.; Parthenios, J.; Papagelis, K.; Galiotis, C.; Kalbac, M.; Vijayaraghavan, A.; Huebner, U.; Gorbachev, R.; Frank, O.; Reich, S. *2D Mater.* **2018**, *5*, 015016.
- (54) Pozzo, M.; Alfe, D.; Lacovig, P.; Hofmann, P.; Lizzit, S.; Baraldi, A. *Phys. Rev. Lett.* **2011**, *106*, 135501.
- (55) White, G. K.; Pawlowicz, A. T. *J. Low Temp. Phys.* **1970**, *2*, 631–639.
- (56) Halvorson, J. J.; Wimber, R. T. *J. Appl. Phys.* **1972**, *43*, 2519–2522.
- (57) Mohiuddin, T. M. G.; Lombardo, A.; Nair, R. R.; Bonetti, A.; Savini, G.; Jalil, R.; Bonini, N.; Basko, D. M.; Galiotis, C.; Marzari, N.; Novoselov, K. S.; Geim, A. K.; Ferrari, A. C. *Phys. Rev. B: Condens. Matter Mater. Phys.* **2009**, *79*, 205433.
- (58) Cerdeira, F.; Fjeldly, T. A.; Cardona, M. *Solid State Commun.* **1973**, *13*, 325–328.
- (59) Tristant, D.; Wang, Y.; Gerber, I.; Monthieux, M.; Penicaud, A.; Puech, P. J. *Appl. Phys.* **2015**, *118*, 044304.
- (60) Choi, W. S.; Seo, S. S. A.; Kim, K. W.; Noh, T. W.; Kim, M. Y.; Shin, S. *Phys. Rev. B: Condens. Matter Mater. Phys.* **2006**, *74*, 205117.
- (61) Lazzeri, M.; Attacalite, C.; Wirtz, L.; Mauri, F. *Phys. Rev. B: Condens. Matter Mater. Phys.* **2008**, *78*, No. 081406, DOI: [10.1103/PhysRevB.78.081406](https://doi.org/10.1103/PhysRevB.78.081406).
- (62) Nixon, D. E.; Parry, G. S. *J. Phys. C: Solid State Phys.* **1969**, *2*, 1732.
- (63) Grüneis, A.; Attacalite, C.; Rubio, A.; Vyalikh, D. V.; Molodtsov, S. L.; Fink, J.; Follath, R.; Eberhardt, W.; Büchner, B.; Pichler, T. *Phys. Rev. B: Condens. Matter Mater. Phys.* **2009**, *80*, No. 075431, DOI: [10.1103/PhysRevB.80.075431](https://doi.org/10.1103/PhysRevB.80.075431).
- (64) Allard, A.; Wirtz, L. *Nano Lett.* **2010**, *10*, 4335–4340.
- (65) Endlich, M.; Molina-Sánchez, A.; Wirtz, L.; Kröger, J. *Phys. Rev. B: Condens. Matter Mater. Phys.* **2013**, *88*, 205403.
- (66) Ulstrup, S.; Andersen, M.; Bianchi, M.; Barreto, L.; Hammer, B.; Hornekaer, L.; Hofmann, P. *2D Mater.* **2014**, *1*, 025002.
- (67) Vinogradov, N. A.; Simonov, K. A.; Generalov, A. V.; Vinogradov, A. S.; Vyalikh, D. V.; Laubschat, C.; Martensson, N.; Preobrajenski, A. B. *J. Phys.: Condens. Matter* **2012**, *24*, 314202.
- (68) Mialitsin, A.; Kim, J. S.; Kremer, R. K.; Blumberg, G. *Phys. Rev. B: Condens. Matter Mater. Phys.* **2009**, *79*, No. 064503, DOI: [10.1103/PhysRevB.79.064503](https://doi.org/10.1103/PhysRevB.79.064503).
- (69) García-Ruiz, A.; Mucha-Kruczyński, M.; Fal'ko, V. I. *Phys. Rev. B: Condens. Matter Mater. Phys.* **2018**, *97*, 155405.
- (70) Lu, H.-Y.; Chen, S.; Xu, Y.; Zhang, L.-Q.; Wang, D.; Wang, W.-S. *Phys. Rev. B: Condens. Matter Mater. Phys.* **2013**, *88*, No. 085416, DOI: [10.1103/PhysRevB.88.085416](https://doi.org/10.1103/PhysRevB.88.085416).
- (71) van Gastel, R.; N'Diaye, A. T.; Wall, D.; Coraux, J.; Busse, C.; Buckanie, N. M.; Meyer zu Heringdorf, F.-J.; Horn von Hoegen, M.; Michely, T.; Poelsema, B. *Appl. Phys. Lett.* **2009**, *95*, 121901.
- (72) Coraux, J.; N'Diaye, A. T.; Engler, M.; Busse, C.; Wall, D.; Buckanie, N.; zu Heringdorf, F.-J. M.; van Gastel, R.; Poelsema, B.; Michely, T. *New J. Phys.* **2009**, *11*, 039801.
- (73) Petaccia, L.; Vilmercati, P.; Gorovikov, S.; Barnaba, M.; Bianco, A.; Cocco, D.; Masciovecchio, C.; Goldoni, A. *Nucl. Instrum. Methods Phys. Res., Sect. A* **2009**, *606*, 780–784.
- (74) *SPIP 6.S.1; Image Metrology*, 2018.
- (75) Grüneis, A.; Senkovskiy, B.; Fedorov, A.; Hell, M.; Michel, S. Ultrahigh Vacuum Optical Spectroscopy of Chemically Functionalized Graphene Nanoribbons. In *Reference Module in Chemistry, Molecular Sciences and Chemical Engineering*; Elsevier, 2017.
- (76) Faris, G. W.; Copeland, R. A. *Appl. Opt.* **1997**, *36*, 2684–2685.
- (77) Barrett, J. J.; Adams, N. I. *J. Opt. Soc. Am.* **1968**, *58*, 311–319.
- (78) YU, P.; Cardona, M. *Fundamentals of Semiconductors: Physics and Materials Properties*; Graduate Texts in Physics; Springer Berlin Heidelberg, 2010.
- (79) Jiang, J.; Saito, R.; Samsonidze, G. G.; Chou, S. G.; Jorio, A.; Dresselhaus, G.; Dresselhaus, M. S. *Phys. Rev. B: Condens. Matter Mater. Phys.* **2005**, *72*, 235408.
- (80) Grüneis, A.; Saito, R.; Samsonidze, G. G.; Kimura, T.; Pimenta, M. A.; Jorio, A.; Filho, A. G. S.; Dresselhaus, G.; Dresselhaus, M. S. *Phys. Rev. B: Condens. Matter Mater. Phys.* **2003**, *67*, 165402.
- (81) Jiang, J.; Saito, R.; Samsonidze, G. G.; Jorio, A.; Chou, S. G.; Dresselhaus, G.; Dresselhaus, M. S. *Phys. Rev. B: Condens. Matter Mater. Phys.* **2007**, *75*, No. 035407, DOI: [10.1103/PhysRevB.75.035407](https://doi.org/10.1103/PhysRevB.75.035407).

2.2 Origin of the flat band in heavily Cs doped graphene



Origin of the flat band in heavily Cs doped graphene

N. Ehlen^{1*}, M. Hell^{1*}, G. Marini², E.H. Hasdeo³, R. Saito⁴, Y. Falke¹,
G. Di Santo⁵, L. Petaccia⁵, G. Profeta², A. Grüneis^{1*}

¹II. Physikalisches Institut, Universität zu Köln,
Zùlpicher Strasse 77, 50937 Köln, Germany

²Department of Physical and Chemical Sciences and SPIN-CNR,
University of L'Aquila, Via Vetoio 10, I-67100 Coppito, Italy

³Research Center for Physics, Indonesian Institute of Sciences,
Kawasan Puspiptek Serpong, Tangerang Selatan, 15314, Indonesia

⁴Department of Physics, Tohoku University, Sendai 980-8578, Japan

⁵Elettra Sincrotrone Trieste, Strada Statale 14 km 163.5, 34149 Trieste, Italy

*To whom correspondence should be addressed;

E-mail: ehlen@ph2.uni-koeln.de, hell@ph2.uni-koeln.de, grueneis@ph2.uni-koeln.de
N. Ehlen and M. Hell have contributed equally.

May 10, 2019

A flat energy dispersion of electrons at the Fermi level of a material leads to instabilities in the electronic system and can drive phase transitions. Here we introduce a method to induce flat bands for two-dimensional (2D) materials. We show that flat bands can be achieved by sandwiching a 2D layer by two cesium (Cs) layers. We apply this method to monolayer graphene and investigate the flat bands by a combination of angle-resolved photoemission spectroscopy experiments and calculations. Our work highlights that zone folding of graphene bands and their hybridization with Cs states are at the origin of the flat energy band formation.

The presented approach is an alternative route for obtaining flat band materials to twisting bilayer graphene. It yields thermodynamically stable flat band materials in large areas.

Introduction

An electronic energy dispersion with a narrow band width for a significant portion of the Brillouin zone (BZ) near the Fermi energy (E_F) is an intriguing electronic system [1, 2]. We refer to such a material, in accordance to literature [1, 2], as a “flat-band material” even though the dispersion is usually not perfectly flat. Due to the singularity in the density of states (DOS) for the flat band, the material is unstable against opening of a gap near E_F that reduces the total energy. The instability can drive a phase transition of the system e.g. into a gapped superconductor, a charge-density wave, or magnetic ordering. Many theories predict that flat bands occur in the dice lattice [3], the Kagome lattice [4, 5, 6], the Lieb lattice [7] and the Tasaki lattice [8]. Some of the flat bands have recently been experimentally observed, e.g. the Lieb lattice [9, 10]. Graphene related systems also provide ample opportunity for engineering flat bands. Theoretically, a carbon Kagome lattice has been predicted [11], and recently, flat bands have been found in bilayer graphene [12] ~ 250 meV below E_F as well as in boron doped graphene nanoribbons [13] ~ 1.5 eV below E_F . However, since these flat bands were not located at E_F , gating or chemical doping needs to be applied to make them relevant for the emergent ground state. It is thus important to induce flat bands at E_F . Flat bands at E_F have been achieved in graphene systems by engineering the stacking order [14, 15, 16, 17], the twist angle [18, 19] and the doping level [20]. Rhombohedrally stacked trilayer graphene exhibits flat bands and, as a consequence, an antiferromagnetic ground state [1, 14, 15, 16, 17]. Bilayer graphene where the two layers are twisted with respect to each other by a magic angle of $\sim 1.1^\circ$ also exhibits a flat band very close to E_F [18, 19]. The discovery of both Mott insulating and superconducting phases

in the $\sim 1.1^\circ$ twisted bilayer graphene [19] highlights the rich physics of the flat band systems. One drawback of rhombohedrally stacked and twisted bilayer systems is that they are fabricated from exfoliated flakes and hence can not be prepared deterministically and in large areas. Furthermore, the crystal structure of the twisted bilayer graphene is unstable against a rotation of the two layers, that brings the system back to the Bernal stacking order, which corresponds to the global energy minimum. Hence, the fabrication and characterization of large area systems that have flat bands at E_F is an important problem in condensed matter physics and materials science.

The present work introduces a new technique that is applied to induce a flat band at E_F of epitaxial graphene which is probed by angle-resolved photoemission spectroscopy (ARPES). The technique relies on the combined effects of zone folding, hybridization and strong electron doping by excess cesium (Cs) / carbon (C) stoichiometry. Zone folding refers to the folding of graphene bands into a smaller supercell. Zone folding of energy bands occurs in the periodic potential of Cs atoms which is widely studied in the context of graphite intercalation compounds [21] and alkali-metal doped bilayer graphene [22]. Recently, zone folding of graphene bands has been observed by oxygen intercalation under graphene/Ir(111) [23]. Zone folding leads to an increase in the number of bands in the folded BZ. For example, a 2×2 zone folding increases the the number of bands by a factor of four compared with those in the unfolded band structure. Because of zone folding, the bands of doped graphene close to E_F occupy a central region of the BZ. Since the Cs band is also located around the BZ center for energies close to E_F , hybridization between graphene and the Cs bands is then possible. It is noted that, without zone folding, there would be no hybridization close to E_F possible because the bands of graphene and Cs do not cross. According to the quantum-mechanical description, a finite hybridization between C and Cs causes anti-crossing of the energy bands. That is, the two dispersions do not actually cross, but disperse away from the hypothetical crossing point

that would occur for no hybridization. We will show in this work that hybridization and anti-crossing are key for obtaining a flat dispersion. A condition for the hybridization is that the alkali metal band is partially filled, i.e. the Cs atom should not be fully ionized. To ensure that the graphene layer is highly doped, we sandwich graphene in between two Cs layers. In fact, the doping levels we achieve are beyond the Lifshitz transition which occurs when E_F is higher than the energy of the conduction band at the M point [20, 24].

Our work is closely linked to chiral superconductivity [25, 26] and conventional superconductivity in graphene [27, 28, 29]. The former is a result of electron-electron interaction in the flat band [25, 26]. The latter is driven by a large electron-phonon coupling (EPC) at E_F in alkali-metal doped graphene [30, 31, 32, 33, 22, 34] in which a large electronic density of states (DOS) at E_F is favorable since the EPC constant can be written by $\lambda = N(0)D^2/M\omega^2$ where $N(0)$ is the DOS at E_F , D is the deformation potential and M and ω are the mass and the phonon frequency, respectively [35]. The critical temperature T_c for conventional superconductivity depends on λ and also on the renormalized Coulomb pseudopotential μ^* that likewise depends on $N(0)$ [35]. Thus, a decrease in the band width can lead to an increase of T_c . However, for the special case of superconductivity in alkali-metal doped graphene systems, not only a large $N(0)$ but also EPC by additional coupling of phonons of graphene to alkali metal layer bands at E_F is required [36, 27, 37]. Thus, alkali metal bands at E_F are necessary for superconductivity in graphene. This condition is equivalent to having a partially occupied alkali metal band (or interlayer state) [36, 27]. The two conditions (high doping level and partially occupied alkali metal band) apparently contradict each other - a high doping level (i.e. a flat band) would mean that all alkali atoms are fully ionized and thus the alkali derived band would be unoccupied whereas a low doping level would allow for the observation of the interlayer state but not the flat band. All previous works failed to engineer and characterize high-quality systems that allow for simultaneous observation of a flat band and the interlayer state. For example,

Ref. [20] reports a flat band but no interlayer state and Refs. [38] and [22] find the interlayer state in bilayer graphene but their doping level is considerably lower than what is needed to occupy the flat band. In the present work we simultaneously observe a flat band at E_F and an alkali metal band by ARPES.

We also investigate the Raman spectrum of heavily doped graphene with a flat band. The doping strongly affects the Raman spectra of epitaxial graphene/Ir(111). The Raman G band shifts down in frequency and assumes a Fano lineshape by alkali-metal doping [24]. The Fano lineshape of the G band in alkali-metal doped graphene has been explained by quantum interference effects in the scattering pathways for vibrational and electronic Raman scattering (ERS) [24]. The relationship of G band frequency and Fano asymmetry (expressed by the parameter $1/q$) versus carrier concentration has been probed for carrier concentrations up to the Lifshitz transition [24]. Here, a large and positive value of $1/q$ means a large Fano asymmetry of the observed Raman peak towards high wavenumbers. It was found that $1/q$ increases with carrier concentration up to $1/q = 0.35$ for a carrier density at the Lifshitz transition [24]. The large $1/q$ is due to a resonance of electronic Raman scattering when the sample is doped slightly below the flat band [24]. However, although the Fano resonance and the flat band appear simultaneously in heavily doped graphene, the Raman response is not known and the relationship for the two phenomena is not clear.

Experimental results

Angle-resolved photoemission spectroscopy

The details of the preparation of monolayer graphene on an Ir(111) substrate are given in Refs. [39, 24]. A large amount of Cs corresponding to a thickness of approximately 30 Å is evaporated onto graphene with a rate of about 1 Å per 1 min (measured by a quartz micro balance) at room temperature. In these conditions, most Cs desorbs from the sample. The result

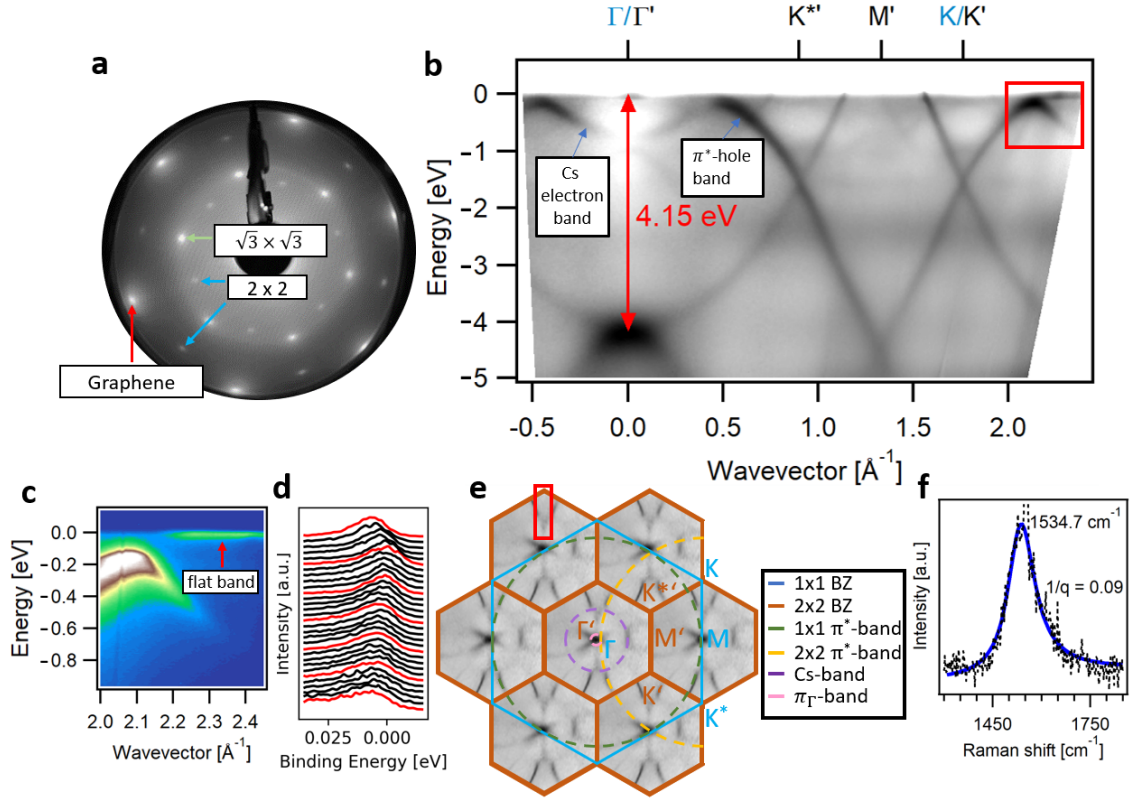


Figure 1: Characterization of Cs 2×2 /graphene/Cs $\sqrt{3} \times \sqrt{3}$ /Ir(111). (a) LEED pattern taken at an energy $E=73$ eV and a temperature $T = 13$ K. (b) ARPES scan ($h\nu = 31$ eV and $T = 17$ K) along the $\Gamma K M$ directions. The region with the flat band is indicated by a red rectangle. The transition energy at the van Hove singularity of 4.15 eV is indicated. The high symmetry points of the original 1×1 and the zone folded 2×2 BZ are denoted in blue and black color, respectively. (c) Zoom-in to the region indicated by a red rectangle in (b) showing the flat band at E_F . (d) Energy distribution curves (EDCs) for the flat band (stepsize 0.01 \AA^{-1}) taken between 2.2 \AA^{-1} (lower EDC) and 2.5 \AA^{-1} (upper EDC). EDCs at every 0.05 \AA^{-1} are colored red. (e) Map at E_F with the 1×1 and 2×2 BZs. The map has been generated from a symmetrized azimuthal map taken in the first BZ. The π^* bands of the original 1×1 and the 2×2 superstructure, the Cs band and the π^* band from close to the Γ point (π_Γ) are indicated. The red rectangle indicates a region along $\Gamma' K'$ containing the flat band. (f) Ultra-high vacuum Raman spectrum taken at $T = 5$ K with a UV laser (325 nm) in a vacuum better than 1.0×10^{-10} mbar.

of the 30 min long exposure to Cs vapor is that one Cs layer intercalates under graphene and the other Cs layer adsorbs on top of the graphene layer. We confirm that only negligible extra Cs atoms stick to the surface of the trilayer structure which is observed by sharp diffraction spots of graphene and Cs in the low energy electron diffraction (LEED) as shown in Figure 1a. The observed LEED pattern consists of three subpatterns: the hexagonal graphene lattice, a Cs $\sqrt{3} \times \sqrt{3}$ -R30° pattern and a Cs 2×2 pattern. From previous works that studied Cs interaction with graphene/Ir(111), it is known that the Cs $\sqrt{3} \times \sqrt{3}$ -R30° phase occurs for the Cs in between graphene and the metal substrate while the Cs 2×2 phase grows above the graphene [40, 24]. Actually, when less Cs is deposited, we obtain the intercalated $\sqrt{3} \times \sqrt{3}$ -R30° phase that we described earlier [24]. Thus, the graphene layer is encapsulated by one Cs $\sqrt{3} \times \sqrt{3}$ -R30° layer and one Cs 2×2 layer. Figure 1b depicts the energy band structure of this sample as is measured by ARPES along the high symmetry directions of the two-dimensional BZ. We observe zone folding of the electronic bands for the 2×2 superstructure. Zone folding occurs in the periodic potential of the top Cs 2×2 layer. It is important to note that the Cs $\sqrt{3} \times \sqrt{3}$ order below the graphene does not cause zone folding. This can be explained by the screening of the Coulomb potential of Cs by the Ir which reduces the effective potential. On the other hand, for the Cs atoms on the top of graphene, the potential is sufficiently large to form the superstructure. The 2×2 zone folding means that a folded BZ with half the original reciprocal lattice vectors appears that corresponds to the 2×2 unit cell. The high symmetry points of the original BZ which are relevant for the ARPES cuts are Γ , K , K^* , and M points. The relevant high symmetry points of the folded BZ are indicated by dashed symbols as Γ' , K' , $K^{*'} and M' (see Figure 1b and 1e). Due to the zone folding, the $K^{*'} and K' points of the zone folded BZ appear at the centers of ΓK and ΓK^* of the original BZ.$$

Let us investigate the observed band structure to phenomenologically identify the origin of the flat band. From the ARPES, we see that there are two Dirac cones: one at K which

corresponds to a wavevector $k \sim 1.7 \text{ \AA}^{-1}$ and the other one at $K^{*'} at $k \sim 0.8 \text{ \AA}^{-1}$. The π conduction bands are located above each of the two Dirac points in the ARPES spectra. In the present case, the conduction bands are partially occupied because of Cs doping. Each of the two π conduction bands consists of two branches that disperse in opposite direction to each other with positive and negative curvatures which we will call π^* electron and hole band, respectively. Around the Γ point we observe an electron band whose minimum is located at 0.7 eV below E_F . This electron band appears only by Cs doping. As we will show later by calculations, the electron band consists mainly of Cs $6s$ states. We therefore call it Cs electron band. The Cs electron band hybridizes with the π^* hole band whose maximum is at $\sim 0.5 \text{ \AA}^{-1}$. The π^* hole band and the Cs electron band are labelled in Figure 1b. Zone folding of the graphene bands is key for the hybridization with the Cs electron band since the graphene bands cross E_F in the original 1×1 BZ at wavevectors $\sim 1.5 \text{ \AA}^{-1}$ and $\sim 2.2 \text{ \AA}^{-1}$. The crossing of E_F by the Dirac cone bands of the 1×1 BZ occurs far away from Γ , therefore a hybridization of graphene bands and Cs electron band close to E_F would not be possible. However, when we consider the zone folded Dirac cone, it can be seen immediately that the Cs electron band and the zone folded π^* hole band can hybridize close to E_F near $\sim 0.5 \text{ \AA}^{-1}$. The hybridization results in an anti-crossing of two branches. An extended flat band emerges as the higher energy branch of the anti-crossing located around Γ/Γ' and M points in the BZ.$

The fact that part of the conduction band is below E_F , allows us to determine the transition energy at Γ/Γ' to be ≈ 4.15 eV from ARPES (see Figure 1b). Due to zone folding, the transition also appears at the M point in the 1×1 BZ. For optical measurements such as resonance Raman spectroscopy, the transition energy is expected to be reduced due to excitonic effects [41, 42]. Thus we can resonantly excite heavily doped graphene and collect Raman spectra with good intensity if the laser energy is close to the value of 4.15 eV. In the following section we will show resonant Raman spectra that are measured using an ultraviolet laser with a wavelength

of 325 nm (3.8 eV). Figure 1c depicts high resolution ARPES in the region close to E_F where the π^* hole band and the Cs electron band display the anti-crossing behaviour. The region appears at $k = 2.2 \text{ \AA}^{-1}$ as discussed before but due to zone folding it is equivalent to the region around $k = 0.5 \text{ \AA}^{-1}$. From Figure 1c, we can find evidence for a hybridization gap between the two branches near E_F . The ARPES scan in Figure 1c shows the flat band in a range from $k = 2.2 \text{ \AA}^{-1}$ to a $k = 2.4 \text{ \AA}^{-1}$. However, considering the full 2D BZ, the flat band covers a much larger area as we will show later. Figure 1d shows the energy distribution curves of the flat band with a band width less than 10 meV. Notably, the band width is even smaller than the one observed for rhombohedral graphene where a band width of $\sim 25 \text{ meV}$ has been observed [17]. In Figure 1e, we plot the 2D map of the ARPES intensity at E_F with highlighting the 2×2 zone folding and the C and Cs derived energy bands. Due to zone folding, there are π^* bands from the original 1×1 BZ and the folded 2×2 BZ that are indicated by green and yellow color, respectively. The π^* derived Fermi surface contours and the Cs derived Fermi surface contours can be approximated well by circles (see the dashed circles in Figure 1e). ARPES matrix element effects are the reason why there are only segments with a strong ARPES intensity along the Fermi surface contours. Because of zone folding, the $\Gamma'K'$ and the KM directions are equivalent. This allows us to observe the flat band segment shown in Figures 1b and 1c multiple times along the $\Gamma'K'$ directions of the zone folded BZs. One such segment is highlighted by a red rectangle in Figure 1e. Analysis of the observed Fermi surface requires consideration of charge carriers that occupy Cs and C derived bands. Using circles as approximations of the Fermi surface contours with C and Cs character, we obtain a total carrier concentration of $n = 5.0 \times 10^{14} \text{ cm}^{-2}$. Let us compare n with the predicted carrier concentration for the $5/8$ filling [26]. In the nearest neighbor TB picture, the equi-energy contour at $5/8$ filling connects adjacent M points in the 2D BZ. For this case, we evaluate a large carrier concentration of $n = 9.0 \times 10^{14} \text{ cm}^{-2}$. The much lower experimental value of

$n = 5.0 \times 10^{14} \text{ cm}^{-2}$ is explained by the trigonal warping effect [43, 44, 21, 45], i.e. the equi-energy contour in the 1×1 BZ does not connect adjacent M points by straight lines but rather by trigonally warped curves. The trigonally warped equi-energy contour reduces n compared without trigonal warping effect. Let us now break up the total charge carrier concentration into Cs and C states contributions. Evaluating the carrier concentration of the Cs band, we find 0.54 electrons remaining per 2×2 unit cell (note: for a full charge transfer, we would have zero electrons remaining in the Cs band and thus the Cs band would appear above E_F). The carrier concentration in the Cs band alone is $n = 2.56 \times 10^{14} \text{ cm}^{-2}$.

Ultra-high vacuum Raman spectroscopy

We have also performed Raman spectroscopy of an identically prepared Cs/graphene/Cs tri-layer. Because of the high sensitivity of Cs doped graphene towards oxygen and moisture, these experiments are carried out in a homebuilt ultra-high vacuum (UHV) Raman system [24]. The sample quality was confirmed *in-situ* by LEED where we have detected a diffraction pattern identical to Figure 1a.

The resonance Raman effect involves an optical transition from valence to conduction band [46, 47]. The difference of the energy levels involved in this transition was evaluated from ARPES as 4.15 eV as discussed in the previous section. Since the transition energy is important for the observation of the present Raman spectrum of heavily doped graphene we compare its value to the transition in pristine graphene. We have shown that the 4.15 eV transition occurs between valence and conduction bands at the M point of the unfolded BZ. The transition energy at the M point in the doped graphene sample is reduced when compared to pristine graphene [24]. Pristine graphene on Ir(111) has the valence band minimum at the M point with an energy of 2.8 eV (see Figure 3b of Ref. [48]). The transition energy at the M point can be expressed by the simplest tight-binding (TB) model in which we adopt one parameter, i.e. the transfer integral between the nearest C atoms, $t_{C-C} < 0$ [44]. In the TB model, the valence and con-

duction bands are symmetric around E_F and the transition energy E at the M point is equal to $E = 2|t_{C-C}|$ [44, 45]. When we use the experimentally observed valence band energy of 2.8 eV at the M point, $2|t_{C-C}| = 5.6$ eV which is 1.5 eV larger than the transition energy we observed by ARPES. A more accurate TB description [44] which also includes the effects of non-zero overlap matrix element s yields $E = 2|t_{C-C}|/(1 - s^2)$ transition energy at M . Using a typical literature value of $s \sim 0.1$ [49, 44] we obtain a slight increase of E in the order of one percent. For both cases of $s = 0$ and $s \sim 0.1$, the calculated transition energy can not explain the ARPES data. Since the electron doping expands the C-C bonds [50], $|t_{C-C}|$ is reduced. Further the energies of valence and conduction bands are affected by exchange and correlation energies that depend on the screening of the Coulomb interaction which is given by density functional theory. For a larger electron density, screening can be more efficient which contributes to the reduction of t_{C-C} . Ulstrup et al. compared ARPES spectra of doped graphene to density functional theory (DFT) calculations and found a reduction of the total π band width upon doping [51]. Thus the reduction of band width - and by extension the reduction of the transition energy - for Cs doped graphene can also be explained by the larger screening of the Coulomb interaction compared with that of pristine graphene.

Figure 1f depicts the Raman spectrum of the G band for graphene in a $\text{Cs } 2 \times 2 / \text{graphene} / \text{Cs } \sqrt{3} \times \sqrt{3} / \text{Ir}(111)$ structure. It can be seen that the G peak is located at an energy of 1534.7 cm^{-1} . This energy is lower than was observed previously for doped graphene. The lower energy indicates larger doping of the present sample compared to previous works [52, 53, 24]. The peak shift can be understood well in terms of the existing theory describing the doping dependence of phonon modes in terms of lattice expansion and phonon self energy renormalization [50]. Using the relation between carrier concentration and G band frequency that we have developed (figure 6a of Ref. [24]) to describe experiments of doped graphene on Ir(111), we correlate the peak position of the G band phonon mode to a carrier concentration. For the experimentally

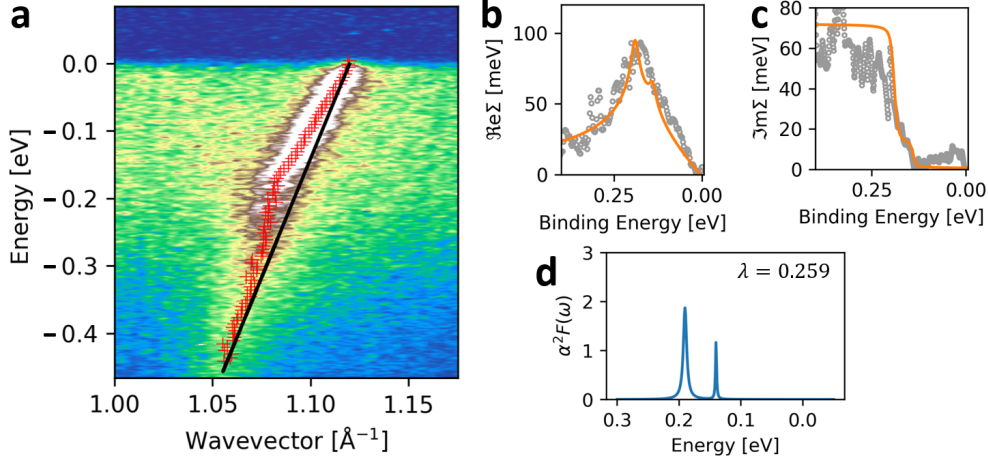


Figure 2: Analysis of the ARPES data in the region close to the Fermi level along $\Gamma K'^*$ direction. ARPES was taken at $h\nu = 31$ eV and at $T = 10$ K. (a) ARPES scan in the vicinity of the Fermi wavevector and Fermi energy. The red crosses denote the ARPES maxima and the black line the bare band. (b) and (c) show the real and imaginary part of the self-energy, respectively. (d) the calculated Eliashberg function.

observed $\omega_G = 1534.7 \text{ cm}^{-1}$ we would expect a carrier concentration of $4.6 \times 10^{14} \text{ cm}^{-2}$. This is in good agreement to the ARPES derived carrier density of $5.0 \times 10^{14} \text{ cm}^{-2}$. Interestingly, for the present system with larger carrier concentration, the Raman spectrum has a smaller Fano asymmetry of $1/q = 0.09$ than for carrier concentrations below or at the Lifshitz transition that we previously measured [24]. As we will show later in the theory section, the dependence of $1/q$ on the carrier concentration reveals a sudden drop of the Fano asymmetry if E_F lies above the flat band. We explain this drop by the effects of electronic Raman scattering and Pauli blocking. The flat band phase is therefore characterized by Raman spectroscopy by a strongly renormalized G band frequency of 1534.7 cm^{-1} and the value of the Fano asymmetry parameter $1/q = 0.09$.

Analysis of electron phonon coupling

Let us now turn to the analysis of EPC which results in a renormalized electronic dispersion

that manifests as a kink in the measured spectral function close to the Fermi wave vectors along ΓK [31, 32, 33]. In Figure 2a, we show ARPES taken in the vicinity of the EPC induced “kink” feature. The self-energy analysis of the kink is performed according to previously established techniques [31, 32, 33]. Figures 2b and 2c depict the real and imaginary part of the self energy, respectively. The corresponding Eliashberg function is shown in Figure 2d and has peaks at ~ 200 meV and ~ 150 meV for intra- and intervalley EPC, respectively. Comparing the relative strengths of the two peaks with graphene doped to a lower carrier concentration, we find that the intravalley peak in the present case is dominant over the intervalley peak. We speculate that the relatively larger importance of intravalley EPC in the present case is related to the flat band which provides a large phase space for scattering with a phonon of a fixed energy. From integration over the complete Eliashberg function, we extract an EPC constant of $\lambda = 2 \int a^2 F(\omega) d\omega = 0.259$ along ΓK which is the largest λ in that crystallographic direction reported in doped graphene so far [31, 32, 33]. The Eliashberg function allows for discriminating the phonon origin of λ by restricting the integration to a certain energy range. That is, if we integrate only over the high-energy peak that emerges due to the Γ point phonon (identical to the Raman G band) we obtain $\lambda_G = 0.203$. Typically, the EPC in KM directions is larger than the EPC along the ΓK direction by a factor 2-3, see e.g. Refs. [31, 32, 33]. Thus we do expect also a record value of λ along the KM direction but unfortunately λ cannot be reliably determined in this direction because the energy maximum of the branch along KM is located at the phonon energy (see Figure 1c where the top of the band appears at 2.05 \AA^{-1} with 0.2 eV binding energy). Note that the large λ in the ΓK direction is also nicely in-line with the large Raman downshift of the G Raman mode as discussed in the previous section.

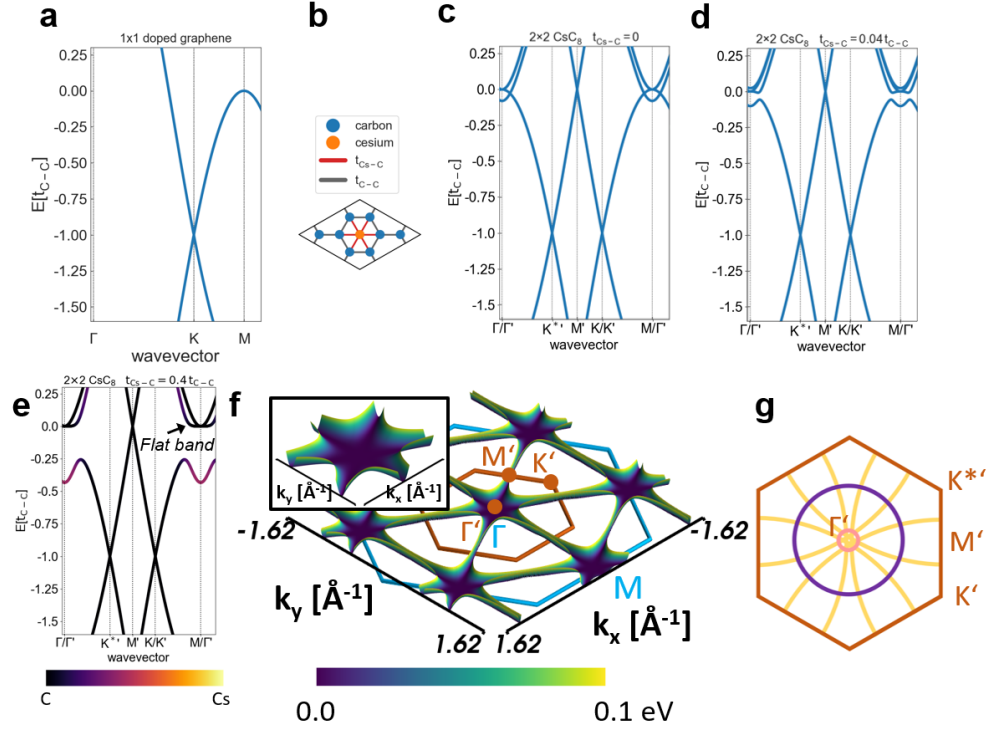


Figure 3: (a) Tight-binding (TB) calculation of the band structure of electrostatically doped graphene in the original 1×1 cell without Cs. (b) Geometry and TB hopping matrix elements for the 2×2 Cs/graphene unit cell. The blue atoms are C and the orange atom is Cs. Red lines indicate Cs-C hopping (t_{Cs-C}) and black lines the C-C hopping (t_{C-C}) within the first unit cell. The six Cs-Cs hopping terms to the nearest neighbors are not indicated. (c) TB calculation of the electronic structure of 2×2 Cs on graphene without Cs-C hybridization, i.e. $t_{Cs-C} = 0$. (d,e) same as in (c) but with non-zero values of t_{Cs-C} . (e) The carbon (cesium) character of the band is indicated by black (purple) color. The flat band is marked by an arrow. (f) 3D plot of the band structure in a region between E_F and $E_F + 0.1$ eV using the parameters of (e). The brown (blue) hexagon denotes the 2×2 (1×1) BZ. The inset shows a zoom of the region around the zone center. In all calculations all TB parameters except t_{Cs-C} are kept constant. Parameters are expressed as multiples of t_{C-C} . We used $\epsilon_{Cs} = -t_{C-C}$, $\epsilon_C = t_{C-C}$ and $t_{Cs-Cs} = 0.2t_{C-C}$ (see text for details on the TB model). All high symmetry points refer to the zone folded Brillouin zone shown in Figure 1e. (g) Experimentally derived Fermi surface contours in the zone folded 2×2 BZ. The contours have been obtained by fits to the Fermi surface extracted from the ARPES experiments as shown in Figure 1e.

Origin of the flat band

We study the effects of zone folding and hybridization between the Cs derived and graphene bands using a simple orthogonal nearest-neighbor TB model. The TB model considers only the upper Cs 2×2 layer which causes the supercell formation since the bottom Cs $\sqrt{3} \times \sqrt{3}$ layer does not impose a sufficiently strong periodic potential as shown by ARPES. As we will show in the next section, the Cs atoms of the bottom layer are fully ionized and thus the bottom layer acts as a charge transfer layer. To accomodate the effects of charge transfer from the bottom layer into the TB calculation, we shift the on-site potential of graphene. Thus, the unit cell of our calculation includes one Cs $6s$ and eight C $2p_z$ orbitals in a 2×2 unit cell with CsC_8 stoichiometry, defining a 9×9 Hamiltonian matrix (see methods section). The parameters needed in our calculation are the two on-site energies for Cs and C orbitals (labeled ϵ_{Cs} and ϵ_C) and the C-C, C-Cs and Cs-Cs hopping parameters indicated as t_{C-C} , t_{C-Cs} and t_{Cs-Cs} , respectively. We start from a non-interacting monolayer graphene and switch on the 2×2 potential and the Cs-C hybridization (i.e. the value of t_{C-Cs}) in steps. The band structure of doped graphene monolayer is shown in Figure 3a. The geometry of the unit cell of our TB calculation and the hopping parameters t_{C-C} and t_{C-Cs} are shown in Figure 3b. Let us now study the effect of zone folding and the effect of Cs-C hybridization on the electronic structure. Figure 3c depicts the bands calculated in a 2×2 supercell but without Cs-C hybridization (indicated by a matrix element $t_{Cs-C} = 0$). Due to zone folding, the Cs band and the graphene derived bands occupy the same region in the $E(k)$ plot. Since we set $t_{Cs-C} = 0$ these bands do not interact with each other and they cross each other. The effect of non-zero t_{Cs-C} becomes obvious by considering the regions in the BZ around Γ and M points. Figures 3d and 3e depict the calculated band structure of the 2×2 system with values $t_{Cs-C} = 0.04t_{C-C}$ and $t_{Cs-C} = 0.4t_{C-C}$. It can be seen that a hybridization gap opens in the electronic spectrum in

the crossing region between graphene and Cs derived bands. As a consequence of the anti-crossing, two branches emerge from that region. The higher energy branch forms an extended flat band at E_F . Importantly, the extent of the flat region is a function of t_{Cs-C} as can be seen by comparing Figures 3c and 3e. We observe that with increasing hybridization t_{Cs-C} , the flat band becomes more extended in the BZ. Figure 3e also shows the carbon and cesium character of the bands which we obtained from the eigenvector of the TB Hamiltonian (see methods). This calculation highlights that the flat band is derived from carbon states. Hence we conclude that it is inherited from the saddle point in the band structure at the M point of the BZ of graphene. This conclusion is in agreement with the next section where first-principles calculations confirm the carbon character of the flat band. The simple TB model thus captures all the essential physics that were observed by ARPES. It highlights that the combined effects of zone folding and hybridization give rise to a flat band at E_F . Importantly, it also means that the Cs derived bands must be occupied in order to form the hybridization. Partial occupation is the case if Cs is partially ionized. In the present experiment, the excess of Cs from the bottom layer ensures partial ionization of the upper Cs layer.

Let us now investigate the dispersion of the flat band in the 2D BZ. The 2D nature of the flat region is important for obtaining an instability in the electronic system because nesting of the electron wavevector is more efficient in an extended flat band. Figure 3f shows a 2D plot of the TB band structure close to E_F . It can be seen that there are extended flat regions at Γ and M points of the 1×1 BZ (or equivalently at the Γ' point of the zone folded BZ). This theoretical result is in excellent agreement to the ARPES map shown in Figure 1e, where the extended flat regions around Γ and M points are visible dark regions. In the inset to Figure 3f, we show that the region around the zone center forms an extended flat band from which stripes of flat regions emerge in a star-like fashion with a sixfold symmetry. The direction of the stripes is along the ΓM direction. To facilitate comparison of the TB calculated Fermi surface to the experimental

Fermi surface, we plot the experimentally derived Fermi surface contours of the zone folded 2×2 BZ in Figure 3g. The experimentally derived Fermi surface contours are obtained from fits of the ARPES intensity maxima by circular shapes as shown previously in Figure 1e. This procedure allows straightforward comparison of theory and experiment because it eliminates ARPES intensity variations due to matrix element effects. The Fermi surface that is shown in Figure 3g includes the zone folded Fermi surfaces of all neighboring BZs. Comparing the TB calculated contour with the contour derived from experiment along $\Gamma'M'$ we see observe good qualitative agreement. Theory and experiment deviate in the shape of the segment along $\Gamma'M'$. In the TB calculation (Figure 3f) it is straight but in the experiment (Figure 3g) it consists of two curved segments. We expect that this is due to trigonal warping which is not adequately described in the nearest neighbor TB calculation. We expect that an improved TB calculation that includes more parameters will achieve quantitative agreement to the experiment.

Our approach might provide a solution to the intense efforts in materials engineering to find new flat band materials and is not limited to small flakes but can produce large-area flat band materials. Such an approach is very much demanded in view of the current interest in flat bands in twisted bilayer graphene - a material that is not available in large areas. The simple nearest neighbor TB approach does not quantitatively describe the experiment, e.g. the experimentally observed band structure around the M' point deviates from the TB calculation. More importantly, the flat part of the band structure in the experiment extends to a much larger part of the BZ, i.e. the simple nearest neighbor TB calculation underestimates the extent of the flat region. To that end, more parameters (hopping between neighbors that are further apart than one bond length) must be included. A parameter-free description is given by first-principles calculations in the following section.

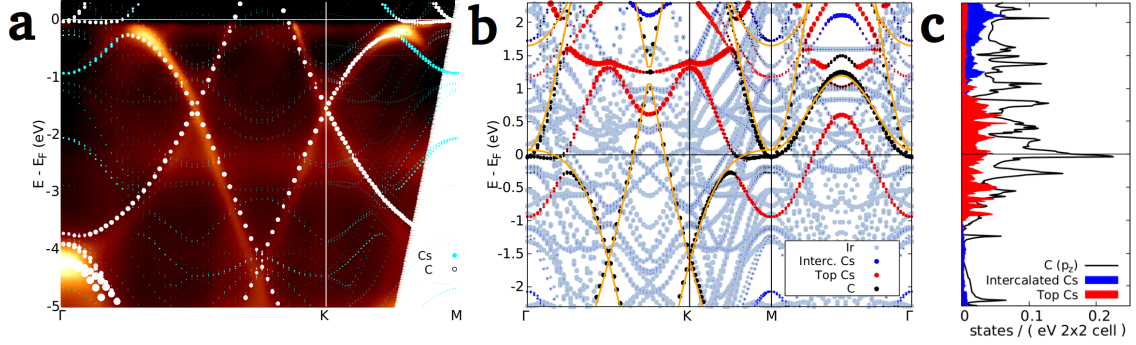


Figure 4: (a) Density functional theory calculations (a shift of -130 meV was applied to match the experimental Fermi level) of 2×2 Cs/graphene/ 2×2 Cs along the $\Gamma K M$ directions (high symmetry points of the original 1×1 BZ) overlaid on the experimental ARPES intensity. The color and the size of the dots indicate the atomic character of the corresponding projected eigenfunction of the Kohn-Sham eigenvalues (white for carbon and cyan for Cs-derived bands). (b) Calculated band structure projected on Iridium (grey), Carbon (black), intercalated Cs (blue) and Cs adatoms (red). The orange lines are calculations of electrostatically doped (i.e. without Cs) free-standing graphene in a 2×2 supercell. (c) Corresponding partial density of states of C, intercalated Cs and top Cs.

Theoretical results and comparison to experiment

Density functional theory calculations of the band structure

First principles DFT calculations are performed by using a plane-wave pseudopotential approach [54, 55, 56] (see methods section for details). Since the 2×2 and the $\sqrt{3} \times \sqrt{3}$ Cs superstructures are incommensurate to each other, the real structure is approximated by using 2×2 Cs adsorbate layers on either side for simplicity. The two Cs layers are relatively shifted within in-plane direction by $\mathbf{a}_1 + \mathbf{a}_2$, where \mathbf{a}_1 and \mathbf{a}_2 are the unit vectors of graphene. After Cs intercalation and subsequent adsorption we find that the graphene-Ir(111) perpendicular distance is 6.17 \AA , indicating a complete detaching of graphene from the substate. The deposited Cs atoms are at distances of 2.97 \AA (for top Cs) and 3.01 \AA (for the bottom Cs) from the graphene layer. These distances are larger than what was obtained for Ba doped graphene in the same recon-

struction [57]. We will show later that these distances are important for the energetic position of the interlayer band. The calculated band structure of the Cs 2×2 /graphene/Cs 2×2 /Ir(111) system is plotted in Figure 4a, in the unfolded 1×1 graphene BZ (note, the bands have been shifted down by 0.13 eV in order to match the experimental Fermi level). The comparison of the calculated results with the experimental ARPES spectrum reveals an impressive agreement between the theoretical and experimental bands. The effect of Cs on the band structure is crucial: apart from the obvious doping effect, the Cs 6s orbital hybridizes with the carbon 2 p_z orbitals. Along the KM direction, we observe a clear anti-crossing and the opening of a local hybridization gap of ~ 200 meV. In the region of the gap opening, the orbital character of the band abruptly changes from C to Cs (see Figures 4a and c). We also calculated the band structure of electrostatically doped graphene in the zone folded BZ (see Figure 4b - orange lines). The band structure of electrostatically doped graphene shows no such gap opening.

Going back to the Cs 2×2 /graphene/Cs 2×2 /Ir(111) system, we see that the anti-crossing results in an electron-like band with cesium character centered at the M point. The other branch of the band with avoided crossing disperses along E_F with a very narrow band width. We obtain a flat band that extends for one half of the KM distance and quantitatively explains the origin of the flat band observed in the ARPES spectra. The flat dispersion gives rise to a van Hove singularity in the DOS; the corresponding peak is seen in Figure 4c. The Cs derived DOS is derived from the intercalated and adsorbed Cs layer. The intercalated Cs layer underneath graphene is almost completely ionized and acts as a charge transfer layer while the adsorbed Cs layer above graphene is only partially ionized and forms part of the Fermi surface. The DOS calculation corroborates full and partial ionization of the Cs layers below and above graphene, respectively. This can be seen in Figure 4c where the partial DOS of the upper Cs layer's 6s orbital crosses E_F (red color area of the DOS of Figure 4c) whereas the partial DOS of the lower layer is localized mostly above E_F . We note that the calculations have been performed

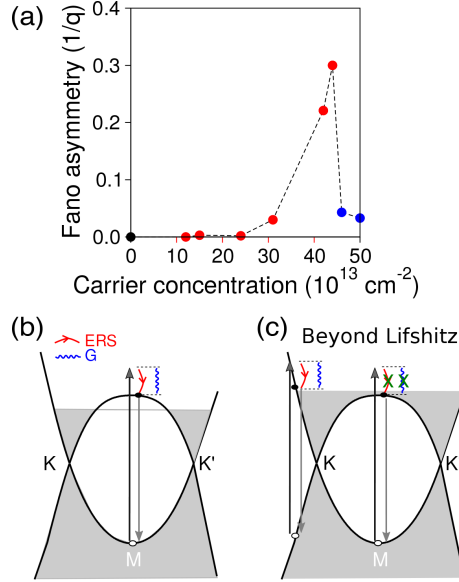


Figure 5: (a) Calculations of Fano asymmetry $1/q$ of the Raman G band of doped graphene versus carrier concentration across the Lifshitz transition. The colors of the points carry the following meaning: black (pristine graphene), red (carrier concentration below the Lifshitz transition) and blue (carrier concentration above the Lifshitz transition). (b) and (c) sketches that depict the Raman interference between vibrational (G , blue) and electronic Raman scattering (ERS, red) before and beyond the Lifshitz transition.

for a 2×2 intercalated Cs layer. We do not expect a qualitative difference for the experimentally observed $\sqrt{3} \times \sqrt{3}$ Cs structure apart from a slightly higher charge transfer for the $\sqrt{3} \times \sqrt{3}$ structure as a result of the higher Cs density. In the present calculation, the higher Cs density (and hence higher charge transfer) was accounted for by downshifting the band structure in energy.

Calculation of the Fano asymmetry of Raman spectra

For calculations of the Raman spectrum of the G band of doped graphene we have employed a previously developed model [58, 24] which incorporates the effects of vibrational Raman scattering and ERS. Figure 5a depicts the calculated Fano asymmetry parameter $1/q$ versus charge carrier concentration, indicating an abrupt decrease to a value close to zero for carrier

concentrations beyond the Lifshitz transition. The large Fano asymmetry in Raman for E_F just below the M point conduction band maximum is a result of the interference of the G band and ERS that are resonant with the van Hove singularity of the DOS (Figure 5b). Increasing the doping level hampers the resonant transition due to Pauli blocking (Figure 5c). As a result, the ERS intensity as well as the Fano parameter $1/q$ decrease. The observed sudden drop in $1/q$ can therefore be explained by the filling of the states at the M point (or Γ' point) as shown in the ARPES section. Thus the combined information of position and asymmetry can be used as a reference for Raman fingerprinting the electronic structure of a Cs/graphene/Cs trilayer. Note, that the calculated value of $1/q$ for the present carrier concentration is in excellent agreement to the observed Fano asymmetry. Theoretically, we obtain $1/q = 0.05$ while the fit to the experimental G band yields $1/q = 0.09$ (see Figure 1f). Interestingly, we did not observe evidence of zone folding of the phonon spectrum. For KC_8 , a new, low-intensity Raman active phonon mode that is derived from the M point of the BZ has been reported [37, 21]. We speculate that its weak intensity precludes its observation in epitaxial graphene since all Raman modes are weakened due to the metallic substrate.

Conclusions and outlook

In the present work, we have used ARPES to directly proof the existence of a flat band in a Cs/graphene/Cs trilayer. TB calculations have revealed the mechanism of flat band formation. Two effects were found to be crucial: 1) zone folding of the graphene bands in a 2×2 supercell and 2) hybridization of the zone folded graphene bands with the Cs metal $6s$ bands at E_F . Condition 2) also implies a partially occupied Cs band, i.e. an incomplete charge transfer of the upper Cs layer. The electronic structure obtained in the present system bears an interesting analogy to the electronic structure of the cuprate high temperature superconductors where the superconducting CuO_2 planes are next to charge reservoir layers. The role of the charge reser-

voir layer in the present case is played by the fully ionized Cs $\sqrt{3} \times \sqrt{3}$ layer below graphene. The doped graphene and the upper Cs 2×2 layer act as charge transport layers. Thus the presented trilayer system and related structures may act as a test-bed for engineering superconductivity in 2D matter by chemical functionalization. The relevance to superconductivity is also clear from the large electron-phonon coupling that has been measured as “kink” feature in ARPES and as a phonon frequency renormalization in Raman spectroscopy. The presented system is relevant to both, chiral and conventional superconductivity because it hosts both, a flat band and a partially filled Cs band and has strong electron-phonon interaction.

Our TB calculations also reveal that the “flatness”, i.e. the extension of the flat band in the 2D BZ can directly be controlled by the wavefunction overlap of the alkali metal s orbital and the carbon $2p_z$ orbital. The wavefunction overlap is given by the parameter t_{Cs-C} in our TB calculations. This parameter is expected to change its value according to the type of alkali or earth alkali metal deposited and thus offers a wide tunability. We expect that Cs has a comparably large hybridization amongst the alkali metals because its outer electron occupies the $6s$ orbital with large spatial extent. It therefore has a large overlap with the adjacent carbon $2p_z$ wavefunctions. The other alkali atoms smaller. We thus predict that the flat band is less extended in the 2D BZ for other MC_8 structures (M being lithium, sodium, potassium or rubidium). From the variation of the parameter t_{Cs-C} (Figure 2) it can be seen that the flatness increases for increasing $|t_{Cs-C}|$. In principle, the presented strategy to induce flat bands could be applied to any 2D material where the alkali metal order implies zone folding of the electronic structure of the host. It would be interesting to induce flat bands in the transition metal dichalcogenide (TMDC) family. TMDCs are known to also host ordered alkali metal intercalant and adsorbate phases. For example, Cs evaporated onto TiS_2 forms a Cs 2×2 superstructure at certain Cs densities [59]. Another TMDC where the presented approach might work is the semiconductor MoS_2 . The conduction band of MoS_2 has several flat segments at Q and K points and in the

segment between Γ and M in the 2D BZ. These points give rise to maxima in the tunneling current in scanning tunneling experiments [60]. Moreover, alkali metal evaporation onto the surface of MoS_2 results in a charge transfer to MoS_2 and the shift of E_F into the conduction band [61]. A sufficiently large charge transfer and an ordered alkali metal adsorbate layer could cause hybridization of the MoS_2 conduction band with the alkali metal band and hence bring the flat segments of the conduction band down to E_F .

Methods

Angle-resolved photoemission spectroscopy and ultra-high vacuum Raman spectroscopy

ARPES was performed at the BaDElPh beamline [62] of the Elettra synchrotron in Trieste (Italy) with linear s - and p - polarisation at $h\nu = 31$ eV. The graphene/Ir(111) samples were prepared in-situ and measured in a vacuum better than 5×10^{-11} mbar. Immediately after the synthesis, Cs deposition was carried out in one-shot in an ultra-high vacuum (UHV) chamber from commercial SAES getters with the sample at room temperature. The Fermi surface map from Figure 1 has been generated from a symmetrized azimuthal sweep of the first zone folded BZ taken at $T = 13$ K. All ARPES measurements plotted in Figure 1 are the sum of s and p polarization.

UHV Raman measurements were performed with the sample at $T = 5$ K in the back-scattering geometry using a commercial Raman system (Renishaw) integrated in a homebuilt optical chamber [63], where the exciting and Raman scattered light were coupled into the vacuum using a HeCd laser with wavelength of 325 nm. The $20\times$ UV objective has a focal distance equal to 13 mm and an NA= 0.32. The position of the laser on the sample was checked by a camera in the laser path. All spectra have been calibrated in position and intensity to the O_2 vibration at 1555 cm^{-1} (see Ref. [64]). The O_2 vibration is visible in the spectra due to the laser

path outside the UHV. Sample preparation and Raman measurements were done in-situ and the sample was never exposed to air.

Tight-binding model of the flat band formation

To simulate the Cs 2×2 /graphene structure we employed an orthogonal tight-binding Hamiltonian using nearest neighbor (nn) hopping for C-C, C-Cs and Cs-Cs bonds. The unit cell of the Hamiltonian consists of 8 C atoms (making up the 2×2 supercell of graphene) and 1 Cs atom. The basis set is thus made up of 8 p_z -orbitals (one at each C site) and one s -orbital at the Cs site yielding a 9×9 Hamilton matrix

$$H = \begin{pmatrix} C1 & C2 & C3 & C4 & C5 & C6 & C7 & C8 & Cs \\ \hline & & & H_{C-C} & & & & & H_{Cs-C} \\ \hline & & & & & & & H_{Cs-C}^\dagger & H_{Cs-Cs} \end{pmatrix} \begin{matrix} C1 \\ C2 \\ C3 \\ C4 \\ C5 \\ C6 \\ C7 \\ C8 \\ Cs \end{matrix} \quad (1)$$

that can be decomposed into an 8×8 Hamilton matrix H_{C-C} describing the C-C intralayer hopping in the 2×2 unit cell, a 1×8 matrix H_{C-Cs} describing the C-Cs interlayer interaction (H_{Cs-C}^\dagger describes the hopping in the other direction) and a scalar function H_{Cs-Cs} describing the Cs-Cs intralayer hopping. In the above Hamiltonian, C atoms are labelled as $C1-C8$ and the Cs atom as Cs . The distance between nearest neighbors in the Cs layer is given by $d_{Cs-Cs} = 2\sqrt{3}a_{C-C}$ with a_{C-C} the C-C bonding distance. There are six nearest neighbor

hopping directions in the lattice given by

$$\begin{aligned}
 \vec{\delta}_1^{Cs} &= a_{C-C}(3, \sqrt{3})^T \\
 \vec{\delta}_2^{Cs} &= a_{C-C}(3, -\sqrt{3})^T \\
 \vec{\delta}_3^{Cs} &= a_{C-C}(-3, \sqrt{3})^T \\
 \vec{\delta}_4^{Cs} &= a_{C-C}(-3, -\sqrt{3})^T \\
 \vec{\delta}_5^{Cs} &= a_{C-C}(0, 2\sqrt{3})^T \\
 \vec{\delta}_6^{Cs} &= a_{C-C}(0, -2\sqrt{3})^T.
 \end{aligned} \tag{2}$$

The Cs-Cs hopping term can then be described by

$$H_{Cs-Cs} = \epsilon_{Cs} + t_{Cs-Cs} \sum_{j=1}^6 \exp(i\vec{k} \cdot \vec{\delta}_j^{Cs}) \tag{3}$$

$$= \epsilon_{Cs} + t_{Cs-Cs} \cdot h_{Cs-Cs}(\vec{k}) \tag{4}$$

with t_{Cs-Cs} the hopping integral, ϵ_{Cs} the on-site potential of the Cs-lattice, and

$$h_{Cs-Cs}(\vec{k}) = (4 \cos(3k_x a_{C-C}) \cos(\sqrt{3}k_y a_{C-C}) + 2 \cos(2\sqrt{3}k_y a_{C-C})). \tag{5}$$

For the C-C and Cs-C hopping, it is helpful to define the hopping directions

$$\begin{aligned}
 \vec{\delta}_1 &= a_{C-C}(1, 0)^T \\
 \vec{\delta}_2 &= a_{C-C} \left(-\frac{1}{2}, \frac{\sqrt{3}}{2} \right)^T \\
 \vec{\delta}_3 &= a_{C-C} \left(-\frac{1}{2}, -\frac{\sqrt{3}}{2} \right)^T
 \end{aligned} \tag{6}$$

and then define

$$f_j^\pm(\vec{k}) = \exp(\pm i\vec{k} \cdot \vec{\delta}_j) \tag{7}$$

which gives the 2×2 nearest neighbor Graphene Hamiltonian

$$H_{C-C} = \begin{pmatrix} \epsilon_C & 0 & tf_1^+ & 0 & tf_3^+ & 0 & tf_2^+ & 0 \\ & \epsilon_C & tf_3^+ & 0 & tf_1^+ & 0 & 0 & tf_2^+ \\ & & \epsilon_C & tf_2^- & 0 & 0 & 0 & 0 \\ & & & \epsilon_C & 0 & 0 & tf_1^+ & tf_3^+ \\ & & & & \epsilon_C & tf_2^- & 0 & 0 \\ & & & & & \epsilon_C & tf_3^+ & tf_1^+ \\ & & & & & & \epsilon_C & 0 \\ & & & & & & & \epsilon_C \end{pmatrix} \quad (8)$$

with $t = t_{C-C}$ the hopping integral and ϵ_C the on-site potential of the carbon lattice. The lower triangle can be constructed from the upper triangle by using the Hermitian condition of Hamiltonians. The C-Cs interlayer hopping can be described by

$$H_{C-Cs} = \begin{pmatrix} 0 \\ t_{C-Cs}f_2^- \\ t_{C-Cs}f_1^+ \\ t_{C-Cs}f_3^- \\ t_{C-Cs}f_3^+ \\ t_{C-Cs}f_1^- \\ t_{C-Cs}f_2^+ \\ 0 \end{pmatrix} \quad (9)$$

with t_{C-Cs} the hopping integral for nearest neighbor C-Cs hopping. The band structures in Figure 2 have been calculated by solving $H(\mathbf{k})\mathbf{c}(\mathbf{k}) = \mathbf{c}(\mathbf{k})E(\mathbf{k})$ where $\mathbf{c}(\mathbf{k})$ and $E(\mathbf{k})$ are the eigenvector and eigenvalue, respectively. The Cs or C character of the bands (Figure 2e) was calculated from the value of the corresponding eigenvector components.

Computational details of the DFT calculation and modelling of the system

First-principles Density Functional Theory calculations were performed to describe the Cs doped graphene system on an Ir(111) surface. We used pseudopotentials approximation for the electron-ion interaction and a plane-wave expansion of the Kohn-Sham wavefunctions as implemented in the *VASP* package [54, 55, 56]. Generalized gradient approximation (GGA)

in the Perdew, Burke and Ernzerhof (PBE) formulation has been adopted for the exchange-correlation potential. A 400 eV cutoff for the plane waves basis set and 14^2 Γ centered \mathbf{k} -point grid with a gaussian smearing of 0.1 eV have been employed. Long range van-der-Waals interaction (important to describe graphene-substrate interactions) have been included by the Grimme's semiempirical correction (DFT-D2) to the functional[65]. Spin-orbit coupling has been self-consistently taken into account.

We modelled the system using a 2×2 graphene unit cell on-top of an Ir(111) terminated surface. Due to the lattice mismatch between graphene and the ideal Ir(111) surface we fixed the in-plane lattice parameter at the graphene equilibrium value (2.47 Å), thus straining the Iridium in-plane lattice constant by $\approx 9\%$. The out-of-plane distance between two Iridium layers has been fixed to its bulk value, using the Ir bulk lattice constant (3.84 Å). Four Ir layers and 25 Å of vacuum have been used in the calculation adding dipole correction to account for the inequivalent top and bottom surfaces of the slab. We treated Cs doping adding one Cs atom per unit cell below the graphene layer as intercalant to detach graphene from the substrate and additional Cs atoms on-top of the graphene layer, both in the hollow sites of the carbon hexagons. With this unit cell, we found that the lowest energy configuration for the adsorbed Cs atoms (above and below graphene) is the one with Cs atoms occupying the center of the two inequivalent hexagons of the 2×2 unit cell. The positions of the carbon and Cs atoms have been relaxed until the forces on the atoms are less than 0.01 eV/Å, while the Ir atoms were fixed to their bulk sites.

Interestingly, both the position and the dispersion of the flat band are slightly affected by spin-orbit coupling induced by the Ir substrate. Although spin-orbit coupling in graphene is negligible, the presence of the Ir substrate induces a relevant reconstruction of the band structure around the Γ -point. The calculated band structure without the inclusion of the spin-orbit interaction shows that the Ir-derived hole-pocket at the Γ -point overlaps with graphene π bands

and is strongly hybridized with them. In particular, we reveal the presence of a flat band at E_F at the M -point. When we switch on the spin-orbit interaction in the calculation, we get a significant change for the Ir states. In particular, at the M point, spin-orbit coupling induces a gap-opening: the Ir bands become lower in energy by strongly reducing the hybridization with graphene bands. Thus the Ir band becomes fully occupied with a band maximum at 175 meV below E_F . The Ir band shows a Rashba type splitting of 0.079 \AA^{-1} which is in agreement with that reported in Ref. [66]. This value can be estimated by the energy position of the surface state of Ir(111)[67].

Calculation of the Raman spectrum

We have performed calculations of the Raman spectrum according to previously developed model [58, 24]. Raman intensity as a function of Raman shift ω_s arises from the interference effect between the phonon G band and the electronic Raman spectra (ERS) causing the Fano resonance [58, 24]:

$$I(\omega_s) = [A_G(\omega_s) + A_{\text{ERS}}(\omega_s)]^2, \quad (10)$$

where $A_G = \sum_{\nu} A_{\nu}$, is the G phonon scattering amplitude which consists of zone center (Γ point) $\nu = \text{LO}$ and iTO modes. A_{ERS} is the ERS scattering amplitude considering only the first order process. To obtain A_G and A_{ERS} , electronic energy bands and wave functions for the electron-photon, electron-phonon and electron-electron interactions have been obtained from tight-binding (TB) method considering up to the three nearest neighbors with TB parameters fitted from ARPES measurement (this work) for each doping level. For simplicity, all Raman calculations are carried out in the $1 \times 1 \text{ BZ}$.

Acknowledgements

NE, MH and AG acknowledge the ERC-grant no. 648589 'SUPER-2D' and funding from Quantum Matter and Materials as well as CRC1238 project A1. The stay at the Elettra synchrotron for ARPES experiments has been supported by Horizon 2020 EC programme under Grant Agreement No. 730872 (CALIPSOplus). H.H. acknowledges funding from DAAD for a stay in Germany. R.S. acknowledges JSPS KAKENHI (No. JP18H01810).

Figures 3a, 3b, 3c, and 3d were generated using the pybinding package for python3 [68]. The Mayavi software was used to generate Figure 3f [69].

References

- [1] N. B. Kopnin, T. T. Heikkilä, G. E. Volovik, High-temperature surface superconductivity in topological flat-band systems. *Phys. Rev. B* **83**, 220503 (2011).
- [2] D. Leykam, A. Andreanov, S. Flach, Artificial flat band systems: from lattice models to experiments. *Advances in Physics: X* **3**, 1473052 (2018).
- [3] B. Sutherland, Localization of electronic wave functions due to local topology. *Phys. Rev. B* **34**, 5208–5211 (1986).
- [4] I. Syozi, Statistics of kagome lattice. *Progress in Theoretical Physics* **6**, 306–308 (1951).
- [5] A. Mielke, Ferromagnetism in the hubbard model on line graphs and further considerations. *Journal of Physics A: Mathematical and General* **24**, 3311–3321 (1991).
- [6] T. Bilitewski, R. Moessner, Disordered flat bands on the kagome lattice. *Phys. Rev. B* **98**, 235109 (2018).
- [7] E. H. Lieb, Two theorems on the hubbard model. *Phys. Rev. Lett.* **62**, 1201–1204 (1989).

- [8] H. Tasaki, Ferromagnetism in the hubbard models with degenerate single-electron ground states. *Phys. Rev. Lett.* **69**, 1608–1611 (1992).
- [9] R. Drost, T. Ojanen, A. Harju, P. Liljeroth, Topological states in engineered atomic lattices. *Nature Physics* **13**, 668 (2017).
- [10] M. R. Slot, T. S. Gardenier, P. H. Jacobse, G. C. P. van Miert, S. N. Kempkes, S. J. M. Zevenhuizen, C. M. Smith, D. Vanmaekelbergh, I. Swart, Experimental realization and characterization of an electronic lieb lattice. *Nature Physics* **13**, 672 (2017).
- [11] C. Zhong, Y. Xie, Y. Chen, S. Zhang, Coexistence of flat bands and dirac bands in a carbon-kagome-lattice family. *Carbon* **99**, 65–70 (2016).
- [12] D. Marchenko, D. V. Evtushinsky, E. Golias, A. Varykhalov, T. Seyller, O. Rader, Extremely flat band in bilayer graphene. *Science Advances* **4**, eaau0059 (2018). DOI: 10.1126/sciadv.aau0059.
- [13] B. V. Senkovskiy, D. Y. Usachov, A. V. Fedorov, T. Marangoni, D. Haberer, C. Tresca, G. Profeta, V. Caciuc, S. Tsukamoto, N. Atodiresei, N. Ehlen, C. Chen, J. Avila, M. C. Asensio, A. Y. Varykhalov, A. Nefedov, C. Wöll, T. K. Kim, M. Hoesch, F. R. Fischer, A. Grüneis, Boron-doped graphene nanoribbons: Electronic structure and raman fingerprint. *ACS Nano* **12**, 7571–7582 (2018).
- [14] Y. Henni, H. P. Ojeda Collado, K. Nogajewski, M. R. Molas, G. Usaj, C. A. Balseiro, M. Orlita, M. Potemski, C. Faugeras, Rhombohedral multilayer graphene: A magneto-raman scattering study. *Nano Lett.* **16**, 3710–3716 (2016).
- [15] D. Pierucci, H. Sediri, M. Hajlaoui, J.-C. Girard, T. Brumme, M. Calandra, E. Velez-Fort, G. Patriarche, M. G. Silly, G. Ferro, V. Soulière, M. Marangolo, F. Sirotti, F. Mauri,

- A. Ouerghi, Evidence for flat bands near the fermi level in epitaxial rhombohedral multi-layer graphene. *ACS Nano* **9**, 5432–5439 (2015).
- [16] B. Pamuk, J. Baima, F. Mauri, M. Calandra, Magnetic gap opening in rhombohedral-stacked multilayer graphene from first principles. *Phys. Rev. B* **95**, 075422 (2017).
- [17] H. Henck, J. Avila, Z. Ben Aziza, D. Pierucci, J. Baima, B. Pamuk, J. Chaste, D. Utt, M. Bartos, K. Nogajewski, B. A. Piot, M. Orlita, M. Potemski, M. Calandra, M. C. Asensio, F. Mauri, C. Faugeras, A. Ouerghi, Flat electronic bands in long sequences of rhombohedral-stacked graphene. *Phys. Rev. B* **97**, 245421 (2018).
- [18] R. Bistritzer, A. H. MacDonald, Moiré bands in twisted double-layer graphene. *Proceedings of the National Academy of Sciences* **108**, 12233–12237 (2011).
- [19] Y. Cao, V. Fatemi, S. Fang, K. Watanabe, T. Taniguchi, E. Kaxiras, P. Jarillo-Herrero, Unconventional superconductivity in magic-angle graphene superlattices. *Nature* **556**, 43 (2018).
- [20] J. L. McChesney, A. Bostwick, T. Ohta, T. Seyller, K. Horn, J. González, E. Rotenberg, Extended van hove singularity and superconducting instability in doped graphene. *Phys. Rev. Lett.* **104**, 136803 (2010).
- [21] M. S. Dresselhaus, G. Dresselhaus, Intercalation compounds of graphite. *Advances in Physics* **51**, 1-186 (2002).
- [22] J. Kleeman, K. Sugawara, T. Sato, T. Takahashi, Enhancement of electron-phonon coupling in Cs-overlayered intercalated bilayer graphene. *Journal of Physics: Condensed Matter* **28**, 204001 (2016).

- [23] Y. Lin, G. Chen, J. T. Sadowski, Y. Li, S. A. Tenney, J. I. Dadap, M. S. Hybertsen, R. M. Osgood, Observation of intercalation-driven zone folding in quasi-free-standing graphene energy bands. *Phys. Rev. B* **99**, 035428 (2019).
- [24] M. Hell, N. Ehlen, B. V. Senkovskiy, H. Hasdeo, A. V. Fedorov, D. Dombrowski, C. Busse, T. Michely, G. Di Santo, L. Petaccia, R. Saito, A. Grüneis, Resonance Raman spectrum of doped epitaxial graphene at the Lifshitz transition. *Nano Letters* **18**, 6045 (2018).
- [25] C. Honerkamp, Density waves and cooper pairing on the honeycomb lattice. *Phys. Rev. Lett.* **100**, 146404 (2008).
- [26] R. Nandkishore, L. S. Levitov, A. V. Chubukov, Chiral superconductivity from repulsive interactions in doped graphene. *Nature Physics* **8**, 158– (2012).
- [27] G. Profeta, M. Calandra, F. Mauri, Phonon-mediated superconductivity in graphene by lithium deposition. *Nat Phys* **8**, 131 (2012).
- [28] J. Chapman, Y. Su, C. A. Howard, D. Kundys, A. N. Grigorenko, F. Guinea, A. K. Geim, I. V. Grigorieva, R. R. Nair, Superconductivity in ca-doped graphene laminates. *Scientific Reports* **6**, 23254– (2016).
- [29] S. Ichinokura, K. Sugawara, A. Takayama, T. Takahashi, S. Hasegawa, Superconducting calcium-intercalated bilayer graphene. *ACS Nano* **10**, 2761-2765 (2016). PMID: 26815333.
- [30] M. Bianchi, E. D. L. Rienks, S. Lizzit, A. Baraldi, R. Balog, L. Hornekær, P. Hofmann, Electron-phonon coupling in potassium-doped graphene: Angle-resolved photoemission spectroscopy. *Phys. Rev. B* **81**, 041403 (2010).

- [31] D. Haberer, L. Petaccia, A. V. Fedorov, C. S. Praveen, S. Fabris, S. Piccinin, O. Vilkov, D. V. Vyalikh, A. Preobrajenski, N. I. Verbitskiy, H. Shiozawa, J. Fink, M. Knupfer, B. Büchner, A. Grüneis, Anisotropic eliashberg function and electron-phonon coupling in doped graphene. *Phys. Rev. B* **88**, 081401 (2013).
- [32] A. V. Fedorov, N. I. Verbitskiy, D. Haberer, C. Struzzi, L. Petaccia, D. Usachov, O. Y. Vilkov, D. V. Vyalikh, J. Fink, M. Knupfer, B. Büchner, A. Grüneis, Observation of a universal donor-dependent vibrational mode in graphene. *Nat. Commun.* **5**, 4257 (2014).
- [33] N. I. Verbitskiy, A. V. Fedorov, C. Tresca, G. Profeta, L. Petaccia, B. V. Senkovskiy, D. Y. Usachov, D. V. Vyalikh, L. V. Yashina, A. A. Eliseev, T. Pichler, A. Grüneis, Environmental control of electron-phonon coupling in barium doped graphene. *2D Materials* **3**, 045003 (2016).
- [34] D. Y. Usachov, A. V. Fedorov, O. Y. Vilkov, I. I. Ogorodnikov, M. V. Kuznetsov, A. Grüneis, C. Laubschat, D. V. Vyalikh, Electron-phonon coupling in graphene placed between magnetic li and si layers on cobalt. *Phys. Rev. B* **97**, 085132 (2018).
- [35] W. L. McMillan, Transition temperature of strong-coupled superconductors. *Phys. Rev.* **167**, 331–344 (1968).
- [36] G. Csanyi, P. B. Littlewood, A. H. Nevidomskyy, C. J. Pickard, B. D. Simons, The role of the interlayer state in the electronic structure of superconducting graphite intercalated compounds. *Nature Physics* **1**, 42 (2005).
- [37] R. P. Smith, T. E. Weller, C. A. Howard, M. P. M. Dean, K. C. Rahnejat, S. S. Saxena, M. Ellerby, Superconductivity in graphite intercalation compounds. *Superconducting Materials: Conventional, Unconventional and Undetermined* **514**, 50–58 (2015).

- [38] K. Kanetani, K. Sugawara, T. Sato, R. Shimizu, K. Iwaya, T. Hitosugi, T. Takahashi, Ca intercalated bilayer graphene as a thinnest limit of superconducting c6ca. *Proceedings of the National Academy of Sciences* **109**, 19610–19613 (2012).
- [39] J. Coraux, A. T. NDiaye, C. Busse, T. Michely, Structural coherency of graphene on ir(111). *Nano Letters* **8**, 565-570 (2008).
- [40] M. Petrovic, I. Srut Rakic, S. Runte, C. Busse, J. T. Sadowski, P. Lazic, I. Pletikosic, Z.-H. Pan, M. Milun, P. Pervan, N. Atodiressei, R. Brako, D. Sokcevic, T. Valla, T. Michely, M. Kralj, The mechanism of caesium intercalation of graphene. *Nature Communications* **4**, 2772– (2013).
- [41] K. F. Mak, J. Shan, T. F. Heinz, Seeing many-body effects in single- and few-layer graphene: Observation of two-dimensional saddle-point excitons. *Phys. Rev. Lett.* **106**, 046401 (2011).
- [42] K. F. Mak, F. H. da Jornada, K. He, J. Deslippe, N. Petrone, J. Hone, J. Shan, S. G. Louie, T. F. Heinz, Tuning many-body interactions in graphene: The effects of doping on excitons and carrier lifetimes. *Phys. Rev. Lett.* **112**, 207401 (2014).
- [43] T. Ando, T. Nakanishi, R. Saito, Berry’s phase and absence of back scattering in carbon nanotubes. *J. Phys. Soc. Jpn.* **67**, 2857–2862 (1998).
- [44] R. Saito, G. Dresselhaus, M. S. Dresselhaus, *Physical Properties of Carbon Nanotubes* (Imperial College Press, 1998).
- [45] A. H. Castro Neto, F. Guinea, N. M. R. Peres, K. S. Novoselov, A. K. Geim, The electronic properties of graphene. *Rev. Mod. Phys.* **81**, 109–162 (2009).

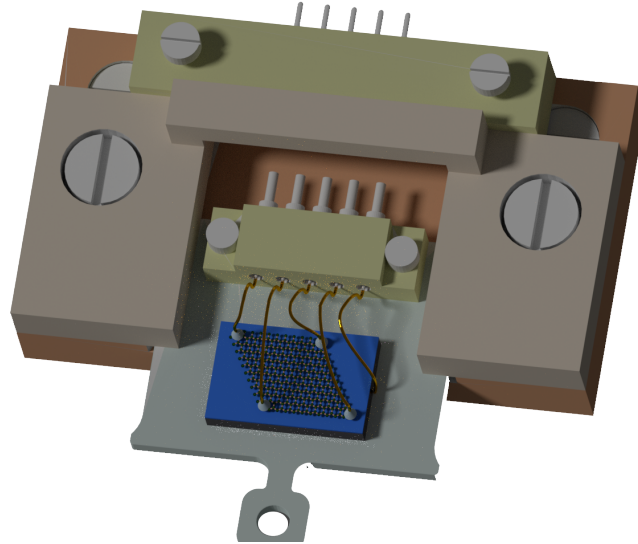
- [46] R. Saito, M. Hofmann, G. Dresselhaus, A. Jorio, M. S. Dresselhaus, Raman spectroscopy of graphene and carbon nanotubes. *Advances in Physics* **60**, 413-550 (2011).
- [47] A. C. Ferrari, D. M. Basko, Raman spectroscopy as a versatile tool for studying the properties of graphene. *Nature Nanotechnology* **8**, 235– (2013).
- [48] C. Tusche, P. Goslawski, D. Kutnyakhov, M. Ellguth, K. Medjanik, H. J. Elmers, S. Chernov, R. Wallauer, D. Engel, A. Jankowiak, G. Schönhense, Multi-MHz time-of-flight electronic bandstructure imaging of graphene on Ir(111). *Appl. Phys. Lett.* **108**, 261602 (2016).
- [49] A. Bostwick, T. Ohta, J. L. McChesney, T. Seyller, K. Horn, E. Rotenberg, Band structure and many body effects in graphene. *The European Physical Journal Special Topics* **148**, 5–13 (2007).
- [50] M. Lazzeri, F. Mauri, Nonadiabatic kohn anomaly in a doped graphene monolayer. *Phys. Rev. Lett.* **97**, 266407 (2006).
- [51] S. Ulstrup, M. Schüler, M. Bianchi, F. Fromm, C. Raidel, T. Seyller, T. Wehling, P. Hofmann, Manifestation of nonlocal electron-electron interaction in graphene. *Phys. Rev. B* **94**, 081403 (2016).
- [52] N. Jung, B. Kim, A. C. Crowther, N. Kim, C. Nuckolls, L. Brus, Optical reflectivity and raman scattering in few-layer-thick graphene highly doped by K and Rb. *ACS Nano* **5**, 5708–5716 (2011).
- [53] R. Parret, M. Paillet, J.-R. Huntzinger, D. Nakabayashi, T. Michel, A. Tiberj, J.-L. Sauvajol, A. A. Zahab, In situ raman probing of graphene over a broad doping range upon rubidium vapor exposure. *ACS Nano* **7**, 165-173 (2013). PMID: 23194077.

- [54] G. Kresse, J. Furthmüller, Efficient iterative schemes for ab initio total-energy calculations using a plane-wave basis set. *Phys. Rev. B* **54**, 11169–11186 (1996).
- [55] G. Kresse, J. Furthmüller, Efficiency of ab-initio total energy calculations for metals and semiconductors using a plane-wave basis set. *Computational Materials Science* **6**, 15–50 (1996).
- [56] G. Kresse, D. Joubert, From ultrasoft pseudopotentials to the projector augmented-wave method. *Phys. Rev. B* **59**, 1758–1775 (1999).
- [57] C. Tresca, N. I. Verbitskiy, A. Grüneis, G. Profeta, Ab initio study of the (2×2) phase of barium on graphene. *The European Physical Journal B* **91**, 165 (2018).
- [58] E. H. Hasdeo, A. R. T. Nugraha, M. S. Dresselhaus, R. Saito, Breit-wigner-fano line shapes in raman spectra of graphene. *Phys. Rev. B* **90**, 245140 (2014).
- [59] H. I. Starnberg, H. E. Brauer, V. N. Strocov, Low temperature adsorption of cs on layered TiS_2 studied by photoelectron spectroscopy. *Surface Science* **384**, L785–L790 (1997).
- [60] C. Murray, W. Jolie, J. A. Fischer, J. Hall, C. van Efferen, N. Ehlen, A. Grüneis, C. Busse, T. Michely, Comprehensive tunneling spectroscopy of quasifreestanding MoS_2 on graphene on $\text{Ir}(111)$. *Phys. Rev. B* **99**, 115434 (2019).
- [61] N. Ehlen, J. Hall, B. V. Senkovskiy, M. Hell, J. Li, A. Herman, D. Smirnov, A. Fedorov, V. Yu Voroshnin, G. Di Santo, L. Petaccia, T. Michely, A. Grüneis, Narrow photoluminescence and Raman peaks of epitaxial MoS_2 on graphene/ $\text{Ir}(111)$. *2D Materials* **6**, 011006 (2018).
- [62] L. Petaccia, P. Vilmercati, S. Gorovikov, M. Barnaba, A. Bianco, D. Cocco, C. Masciovecchio, A. Goldoni, Bad elph: A normal-incidence monochromator beamline at elettra. *Nu-*

clear Instruments and Methods in Physics Research Section A: Accelerators, Spectrometers, Detectors and Associated Equipment **606**, 780–784 (2009).

- [63] M. G. Hell, Y. Falke, A. Bliesener, N. Ehlen, B. V. Senkovskiy, T. Szkopek, A. Grüneis, Combined ultra high vacuum raman and electronic transport characterization of large-area graphene on sio₂. *Phys. Status Solidi B* **255**, 1800456 (2018).
- [64] G. W. Faris, R. A. Copeland, Ratio of oxygen and nitrogen raman cross sections in the ultraviolet. *Appl. Opt.* **36**, 2684–2685 (1997).
- [65] S. Grimme, Semiempirical gga-type density functional constructed with a long-range dispersion correction. *J. Comput. Chem.* **27**, 1787–1799 (2006).
- [66] A. Varykhalov, D. Marchenko, M. R. Scholz, E. D. L. Rienks, T. K. Kim, G. Bihlmayer, J. Sánchez-Barriga, O. Rader, Ir(111) surface state with giant rashba splitting persists under graphene in air. *Phys. Rev. Lett.* **108**, 066804 (2012).
- [67] A. Dal Corso, Clean ir(111) and pt(111) electronic surface states: A first-principle fully relativistic investigation. *Surface Science* **637-638**, 106–115 (2015).
- [68] D. Moldovan, M. Andelkovic, F. Peeters, pybinding v0.9.4: a Python package for tight-binding calculations (2017). This work was supported by the Flemish Science Foundation (FWO-VI) and the Methusalem Funding of the Flemish Government.
- [69] P. Ramachandran, G. Varoquaux, Mayavi: 3D Visualization of Scientific Data. *Computing in Science & Engineering* **13**, 40–51 (2011).

2.3 Combined ultra high vacuum Raman and electronic transport characterization of large-area graphene on SiO₂



ORIGINAL PAPER

Electronic Properties of Novel Materials



Combined Ultra High Vacuum Raman and Electronic Transport Characterization of Large-Area Graphene on SiO₂

Martin G. Hell,* Yannic Falke, Andrea Bliesener, Niels Ehlen, Boris V. Senkovskiy, Thomas Szkopek, and Alexander Grüneis*

An original experimental setup which allows for simultaneous sample characterization by Raman spectroscopy and electronic transport in ultra-high vacuum at low temperatures is presented. We show the applicability of this setup for the case of graphene that is transferred from an Ir(111) single crystal onto SiO₂. The transfer of graphene is carried out using a water-promoted electrochemical bubbling technique which is applied to graphene/Ir for the first time. The characterization prior to the transfer includes electron diffraction, photoemission spectroscopy and Raman spectroscopy using ultraviolet excitation. Following the transfer procedure, the graphene layer is electrically contacted and mounted onto a special sample carrier. This carrier allows for combined Raman and transport measurements inside an ultra high vacuum (UHV) system. UHV Raman mapping reveals a large area homogeneous graphene quality over several mm² characterized by a D/G intensity ratio less than 0.1. UHV electrical characterization of transferred graphene in a field effect transistor geometry yields a carrier mobility of 675 cm² V⁻¹ s⁻¹. Upon alkali metal doping in UHV conditions using a Cs getter, a decrease of the 4-point resistance from above 2500 Ω to below 10 Ω is observed. The presented approach paves the way for future combined UHV Raman and transport characterization of two-dimensional materials that are doped into superconducting or charge-density-wave ground states.

challenging task which is essential, e.g., for the study of the superconducting state of graphene.^[1,2] that can be induced by alkali metal doping monolayer or few-layer graphene.^[3–8] Raman spectroscopy applied in ultra-high vacuum (UHV) has been shown to be a powerful method to study the doping induced electron–phonon coupling and lattice expansion.^[9] However, often one wishes to combine the spectroscopic information from Raman scattering with an electronic transport characterization. The application of these two techniques in tandem would neatly combine the selectivity of spectroscopic data (for example the selective probing of the C–C vibration) with the high sensitivity that can be achieved in electronic transport experiments. The present manuscript thus aims at introducing an experimental setup that is capable of measuring the very same sample in UHV conditions using Raman and electronic transport. We also show the procedures needed to obtain samples that are needed for carrying out such experiments and show first experimental results obtained with this setup on pristine and alkali metal doped graphene on insulators.


1. Introduction

The spectroscopic and electronic transport characterization of air-sensitive two-dimensional (2D) materials remains a

The graphene used here is produced by chemical vapour deposition on Ir(111) single crystals. A clean transfer procedure is key for avoiding the reaction of residual chemicals or water with the deposited alkali metal. The large area of epitaxial graphene eases the fabrication of contacts. To date several transfer procedures for 2D materials have been established on the basis of etching,^[10] (electro)chemical-based bubbling transfer,^[11–16] ultrasound-based,^[17] peeling-based,^[18–20] or stamping^[21–23] methods. In the case of graphene, for samples that are produced on Cu foil the etching of the substrate results in metal contaminations and often precludes the repeated use of the growth substrate. Growth on single crystal metal substrates provides an alternative way of obtaining large area graphene layers with a single orientation which is needed, e.g., analyzing the band structure by angle resolved photoemission spectroscopy measurements.^[9] Only the bubbling transfer technique and stamping are potential options for the transfer in this case and a wide range of delamination steps have been reported for Pt,^[12,14]

M. G. Hell, Y. Falke, A. Bliesener, N. Ehlen, Dr. B. V. Senkovskiy, Prof. A. Grüneis
II. Physikalisches Institut
Universität zu Köln
Zùlpicher Strasse 77, 50937 Köln, Germany
E-mail: hell@ph2.uni-koeln.de; grueneis@ph2.uni-koeln.de

Prof. T. Szkopek
Department of Electrical and Computer Engineering
McGill University
845 Sherbrooke St W, Montreal, QC H3A 0G4, Canada

 The ORCID identification number(s) for the author(s) of this article can be found under <https://doi.org/10.1002/pssb.201800456>.

DOI: 10.1002/pssb.201800456

Cu,^[13,24,25] and even Ir.^[16] Fundamentally, the steps during transfer are the intercalation underneath graphene to weaken the bonding to the substrate^[26] and polymethylmethacrylate (PMMA) deposition as a support layer.^[15] This contribution shows the full life-cycle of a graphene sample and is organized as follows. In section 2 we describe the experimental setup. Sections 3 and 4 are related to the growth of graphene on Ir(111) and to the characterization of the graphene/Ir(111) system. Section 5 is about the transfer procedure that is carried out in ambient conditions to transfer graphene onto Si wafers. Section 6 gives details on how such contacted graphene samples on Si wafers are placed back inside the UHV system and characterized by UHV-Raman and electronic transport. Finally, section 7 gives conclusions and an outlook.

2. Setup

Figure 1 depicts a schematic drawing of the setup that we have built. This setup allows us to perform in situ Raman spectroscopy combined with transport measurements at ultra high vacuum (UHV) conditions with a base pressure of $\approx 2 \times 10^{-10}$ mbar. It consists of an analytical chamber where the Raman spectroscopy is performed and a preparation chamber where samples can be prepared or functionalized chemically. In the analysis chamber, there is a specially designed optical flange which directs an ex situ laser beam directly onto samples. The sample plates are suitable for performing transport measurements as there are five spring connectors attached (four pins are used to measure the four-point resistance and one pin is used for gating). The inset of Figure 1 depicts a sketch of a sample holder.

3. Growth

Graphene was produced in ultra high vacuum (UHV) at a base pressure of $\leq 10^{-9}$ mbar using an Ir(111) single crystal which was first sputtered (1 keV) in Ar atmosphere 1×10^{-6} mbar followed by an anneal step under O_2 flow (1×10^{-7} mbar) at 1200°C for 30 min to oxidize the surface. When the crystal cooled down to

ambient conditions, a rapid flash to 1700°C provided a clean surface indicated by a 1×1 LEED pattern that showed a sharp hexagon, illustrated in the inset of Figure 2b. The growth was performed by a low pressure hydrocarbon room temperature adsorption of C_3H_6 molecules (propene), followed by decomposition at a fixed, elevated temperature (1250°C), referred as a temperature programmed growth (TPG).^[27] Hereby the graphene flakes are perfectly oriented with their dense packed direction in registry with the Ir(111) surface. The TPG cycle leads only to a 0.2 ML coverage,^[28] but the very high temperature prevents the generation of additional rotational variants of graphene. A complete monolayer graphene sheet is obtained by exposing the hot (1250°C) sample for additional 15 min at a pressure of 1×10^{-6} mbar to a continuous flow of hydrocarbon gas, referred as a chemical vapor deposition (CVD), finalized with slow cooling to room temperature to avoid wrinkle formation.^[29] The combination of TPG and CVD enables a full graphene coverage with an excellent orientational order and a small amount of defects.

4. Characterization of Graphene/Ir(111)

A UHV-Raman system^[30] allows us to measure Raman spectra of the Gr/Ir(111) sample directly after the growth without any exposure to air. The measurement shown in Figure 2a was performed with a Renishaw InVia Raman system, using a 2 mW 325 nm ultraviolet laser and a $20\times$ UV long-working distance microscope objective with a focal distance equal to 13 mm and a $NA = 0.32$. The G-peak is located at 1593 cm^{-1} . The 2D peak is absent in our measurements of graphene on Ir(111). This is a very similar observation as found by Usachov et al. for graphene grown on Co(0001) and Ni(111) surfaces.^[31] Similarly, a weak 2D intensity for UV excitation (325 nm) was also found for graphene transferred onto Si oxide wafers.^[32,33] Low energy electron diffraction (LEED) experiments were performed using an OCI rear view LEED optics with 4 retarding grids. The instrument was operated inside the UHV chamber attached to the UHV Raman with a base pressure in the 10^{-10} mbar range. Samples were kept at room temperature during measurements. The typical moiré pattern is shown in

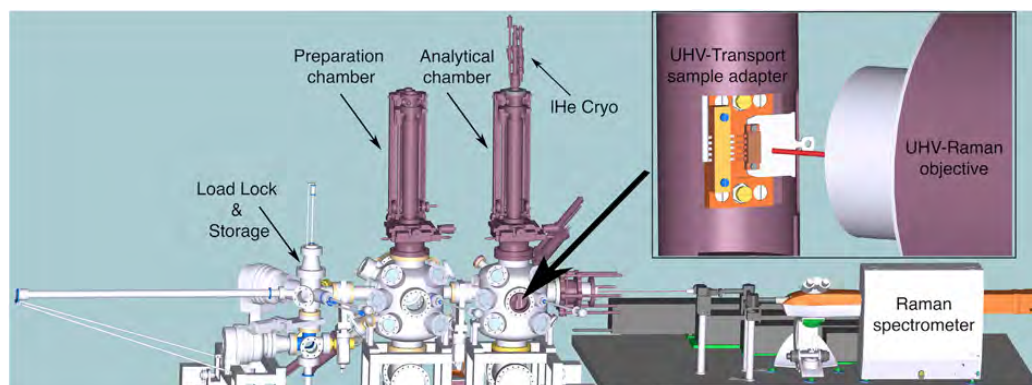


Figure 1. UHV-Raman and transport setup with an inset showing the UHV-Raman objective focusing the laser beam and the transport sample plate adapter attached to the IHe cryostat.

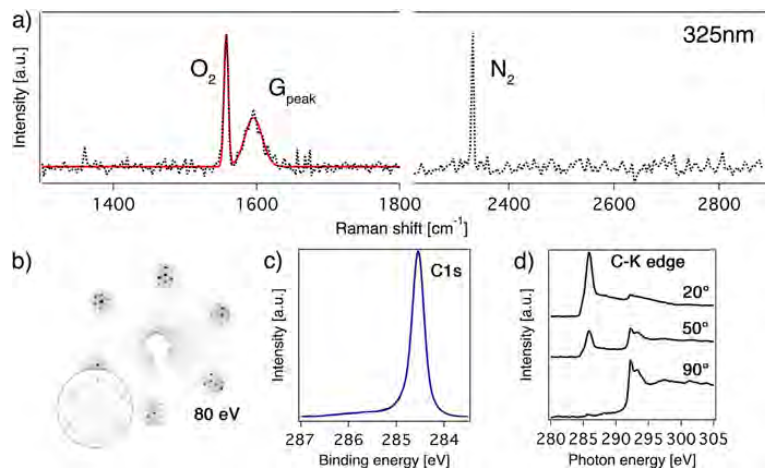


Figure 2. Characterization of graphene grown on Ir(111). a) Ultra high vacuum Raman spectrum with 325 nm excitation wavelength. The Raman G band is located at 1593 cm⁻¹ with a calibration by O₂ at 1555 cm⁻¹. The 2D peak is absent whilst the peak at 2331 cm⁻¹ corresponds to N₂. b) LEED pattern of Gr/Ir(111) at 80 eV with the typical moiré pattern and pristine Ir(111) as an inset. c) XPS spectra depict the C1s core level at 284.5 eV. d) NEXAFS spectra of C K-edge at three different angles of linearly polarized light to the sample surface.

Figure 2b and shows the six-fold symmetry having the Ir spots surrounded by graphene satellites.

X-ray photoelectron spectroscopy (XPS) data are shown in Figure 2c and were obtained at the Russian-German beamline (RGL) of the HZB BESSY II synchrotron radiation facility (Berlin, Germany). The graphene/Ir(111) samples were prepared in-situ and measured in a vacuum better than 5×10^{-10} mbar. XPS spectra were measured with photon energy of 370 eV and pass energy of 5 eV in the normal emission geometry. All XPS spectra were calibrated using Ir4f core levels. XPS shows one C1s peak at 284.5 eV with a narrow (280 meV) linewidth indicating that the graphene is of high quality and not contaminated.^[34]

Near edge X-ray absorption fine structure (NEXAFS) spectroscopy has been performed in partial yield mode at the Russian-German beamline (RGL). Figure 2d depicts the C-K edge NEXAFS spectra measured at three different incidence angles of linearly polarized light regarding the surface of graphene on Ir(111). The peaks at the photon energy around 285 eV are related to transitions from the C 1s core levels to unoccupied molecular π^* and σ^* bands having a minimum and the peaks at the photon energy range 290–310 eV have a maximum for normal incidence. This angle dependence corroborates that the graphene is lying planar on the surface.

Angle-resolved photoemission (ARPES) measurements of Gr/Ir(111) are shown in a related publication^[9] and confirm the weak p-doping of graphene/Ir(111) in agreement to literature^[35] reporting a Dirac crossing 100 meV above the Fermi level. ARPES moreover confirms that the graphene is monolayer in nature since only a single π valence band appears.

5. Transfer Procedure

To weaken the interaction to the single crystal prior to the transfer procedure, we used a water intercalation method.^[36] To that end the graphene/Ir(111) was kept in distilled water at 90 °C for 1 h and afterwards dried at 90 °C for 2 min. For the

bubbling transfer we used a setup described previously.^[37] In short, 2 μ L of PMMA [poly(methyl methacrylate)] with an average mass of 950 kDa per polymer chain was drop-coated on the sample as a support layer. PMMA was dried at 70 °C to obtain a flat surface and baked it at 90 °C for 2 min. Note that these temperatures are below the glass transition temperature of PMMA. Then the PMMA/graphene/Ir(111) stack was immersed in a 1 mol L⁻¹ aqueous NaOH solution and used as a cathode (Figure 3a). The anode was a Pt grid which is chosen because of its chemical inertness. When applying a voltage to the system, the half equations for the reactions on the cathode and anode can be written as:^[25]



Here, the upper (lower) reaction takes place at the negative (positive) pole of the electrochemical cell. Thus H bubbles appear at the Ir crystal and slowly penetrate in between the graphene and Ir(111) crystal from the side and delaminate the PMMA/graphene stack. The applied voltage was ≈ 2.5 V and the delamination took ≈ 20 min. When the graphene and the supporting PMMA were completely separated from the underlying Ir(111), the sample was floating on the liquid as is shown in Figure 3b and was picked up and rinsed carefully in deionized water for several minutes. The supporting PMMA layer makes it easy to handle the graphene sample simply using a tweezer or a glass slide. The target substrate (SiO₂) was baked at 130 °C for 5 min. To increase hydrophobicity, the baked wafer was exposed to HMDS (hexamethyldisilazane)^[38] vapor for 5 min and a glass slide assisted to scoop out the PMMA/graphene and place it directly onto the wafer. To remove water between graphene and the target substrate, the sample was first

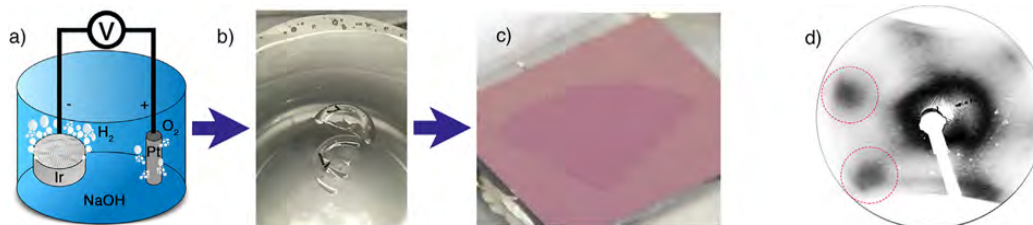


Figure 3. Key steps of the transfer process: a) Electrochemical delamination in aqueous NaOH solution. b) Delaminated PMMA/graphene stack. c) Photograph of transferred graphene/SiO₂ with enhanced contrast. d) LEED pattern of graphene/SiO₂ at 80 eV.

heated to 70 °C for 10 min and then additional 30 min at 90 °C. The sample was then slowly cooled down to room temperature and the PMMA was removed by in DCE (1,2-dichloroethane) for 24 h and rinsed in IPA (isopropyl alcohol) and distilled water. The final result is shown in Figure 3c as a typical photograph of a graphene film transferred by the above-described method to a silicon substrate with ≈ 300 nm SiO₂ layer. The size of the roundish shaped graphene is approximately 1 cm in diameter and visible to the naked eye. Finally, the sample with graphene was mounted onto a sample carrier with five electrical pins (for four point resistance measurements as a function of gate voltage) and electrically contacted using 50 m Au wire. Then the sample was put back inside the UHV system and annealed for about 1 h at 250 °C. Figure 3d shows LEED of the transferred graphene layer. The blurry, due to charging, spots that are arranged in a hexagon are from graphene. The fact that we observe LEED indicates a reasonable surface cleanliness and flatness of the graphene and is a very useful parameter for further optimization. For example, such sample may be useful for future ARPES investigations.

6. Spectroscopic and Electrical Transport Characterization of Transferred Graphene on SiO₂

Raman spectroscopy was used to characterize the transferred graphene/SiO₂ sample. The averaged Raman spectrum carried out with a 532 nm laser is shown in Figure 4a. The G-peak can be found at 1582 cm⁻¹ with a FWHM (full width at half maximum) of

17 cm⁻¹. We also have a small defect mode (1350 cm⁻¹). The Raman spectrum is the sum over Raman spectra collected across the whole sample in a 400 × 400 μm² map with a step size of 20 μm. The scan is carried out in a serpentine like fashion. The corresponding Raman map is shown in Figure 4b. The D/G intensity ratio is constant along the scan and shows a value of 0.09. The origin of the D peak can in principle be two-fold. One is that the transfer induces strain and can cause the graphene to break. The other reason is that the transfer process induces wrinkling which can also cause a finite D band.^[39]

Let us now move to the characterization by transport. Our experimental setup allows for a combined Raman and transport characterization inside UHV. Thus the same sample that we measured Raman and LEED from, could be characterized electrically without exposure to air to avoid molecular adsorption from air, which modifies the transport characteristics. We have performed four point resistance measurements in the van der Pauw geometry as a function of gate voltage, as shown in Figure 5a. We found that the four-point resistances $R_{1,2}$ and $R_{1,4}$ differ by less than 10%. Figure 5b(1) is a photograph of the graphene/SiO₂ sample mounted on the UHV sample holder with five electrical connections. The gate sweep shows a slightly p-doped sample with the Dirac point at a gate voltage $V_D = 3.5$ V, measured at a temperature of 5 K. The charge carrier density n is estimated according to $n = CV/eA$ with $C = \epsilon\epsilon_0 \cdot A/d$ (here C is the sheet capacitance of the back gate, V_D the gate voltage of maximum sheet resistance, e is the elementary charge, $\epsilon_{(0)}$ the vacuum permittivity respectively for SiO₂, and d the thickness of the oxide layer). For $C = 11.5$ nF cm⁻² (for 300 nm SiO₂) and

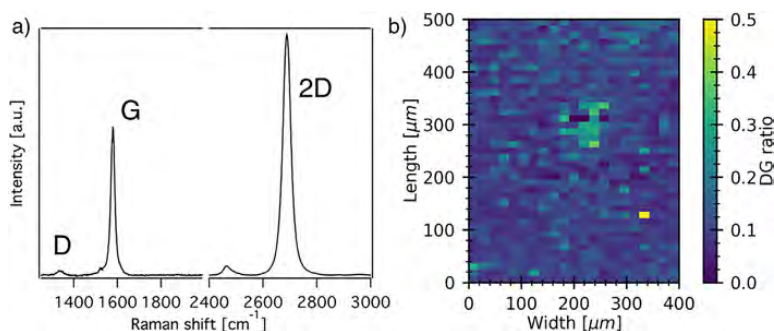


Figure 4. a) Averaged UHV-Raman spectra of transferred graphene/SiO₂ with 532 nm excitation wavelength. b) The individual UHV-Raman map over an area of 400 × 500 μm² graphene/SiO₂.

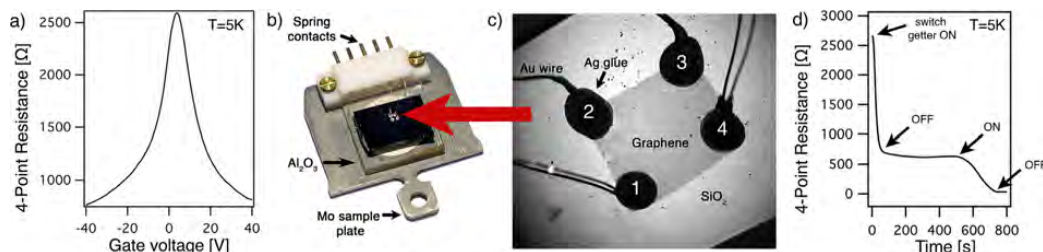


Figure 5. a) Four-point resistance of a transferred graphene monolayer on SiO_2 versus gate voltage applied measured inside ultra high vacuum (UHV) using the setup shown in Figure 1. The curve shows a maximum resistance at a gate voltage of 3.5 V. b) A photograph of a typical sample mounted onto a UHV compatible sample carrier. c) Photograph of the four Au wires contacted to graphene. These four contacts are used for the four-point resistance measurement inside UHV. The edges of the graphene layer have a length of approximately 1 mm. d) UHV four-point resistance characteristics during Cs doping of graphene on SiO_2 .

$V_D = 3.5 \text{ V}$ we reach a carrier density of $n = 2.5 \times 10^{11} \text{ cm}^{-2}$. The quality of the transferred graphene can also be estimated from the field effect mobility μ_{FE} which is given as $\mu_{\text{FE}} = (1/C) \cdot d(1/R)/dV$. Here $d(1/R)/dV$ is the derivative of the reciprocal sheet resistance with respect to the gate voltage V . The sheet resistance for a geometry of an infinite sheet is determined by $R = (2\pi/\ln 2) \cdot V_x/I_x$, where V_x/I_x is the measured four point resistance shown in Figure 5a for the four probe geometry on a square.^[40] A maximum carrier mobility of $\mu_{\text{FE}} = 675 \text{ cm}^2 \text{ V}^{-1} \text{ s}^{-1}$ was obtained from this procedure. Importantly, this is a lower bound for μ_{FE} because our actual geometry is much closer to a “greek cross” geometry, albeit with round contacts. Versnel et al.^[41] show that for a ratio of contact to sample perimeter less than approximately 0.3, there is negligible correction to the ideal van der Pauw formula. For this situation one would use $R = (\pi/\ln 2) \cdot V_x/I_x$ yielding $\mu_{\text{FE}} = 1350 \text{ cm}^2 \text{ V}^{-1} \text{ s}^{-1}$. This compares well to the mobilities of graphene transferred from Ir(111) obtained by other groups. For example Miniussi et al. found a $\mu_{\text{FE}} = 400 \text{ cm}^2 \text{ V}^{-1} \text{ s}^{-1}$. Figure 5d shows the doping of Gr/SiO_2 by Cs atoms evaporated from a commercial getter (SAES) at UHV conditions. Hereby the 4-point resistance changes from above $\approx 2500 \Omega$ to below 10Ω over a time of approximately 700 s. We used a very low evaporation rate that is below the detection limit of a standard quartz microbalance. Nevertheless one can clearly see the dramatic decrease of the 4-point resistance when the getter is switched on, while plateaus in the resistance versus time trace correspond to the situation wherein the getter is switched off.

7. Conclusions and Outlook

In conclusion we have shown a complete characterization of large area graphene before the transfer (by XPS, NEXAFS, LEED, ARPES, and Raman) and after the transfer (by LEED, Raman, and electrical transport). For the transfer we have employed a combination of water intercalation and bubbling transfer. This approach efficiently tackles the increased adhesion of graphene to the Ir substrate. Graphene layers prepared in such a way can be a platform for further investigation by combined spectroscopic and transport measurements inside UHV. As an example we performed alkali metal doping by Cs atoms showing the dramatically decrease

of the 4-point resistance inside UHV. The show case example leads directly to experiments where graphene is pushed in the superconducting state. In such an experiment, the charge carrier concentration for low alkali doping could be conveniently read off from the Dirac point position in the gate sweep and at high doping from the Raman G band shift. In a related experiment where alkali doping of Gr/Ir(111) has been performed in the setup shown here, a strong renormalization of the phonon energies and an unusual Fano asymmetry were observed.^[9] The experimental setup shown here would thus allow to perform alkali metal doping of graphene in a device geometry. Another interesting application of UHV compatible transport would be to perform gating during ARPES measurements inside UHV. This would allow *in-operandi* characterization of graphene devices.

Acknowledgements

MH, NE, BVS, and AG acknowledge the ERC grant no. 648589 ‘SUPER-2D’, funding from DFG projects CRC 1238 (project A1) and GR 3708/2-1. A.G. acknowledges INST 216/808-1 FUGG and support from the “Quantum Matter and Materials” (QM2) initiative. T.S. acknowledges support from QM2 for his stay in Köln. The research leading to these results has received funding from the European Community’s Seventh Framework Programme (FP7/2007-2013) under grant agreement n.312284 (CALIPSO). The authors thank HZB BESSY II and the Russian-German Laboratory (RGLB) for the beamtime allocation. This work has been supported by the University of Cologne through the Institutional Strategy of the University of Cologne within the German Excellence Initiative.

Conflict of Interest

The authors declare no conflict of interest.

Keywords

bubbling transfer, field-effect transistors, graphene, Ir(111), polymethylmethacrylate, transfer of graphene, ultra-high vacuum Raman

Received: September 2, 2018

Revised: November 3, 2018

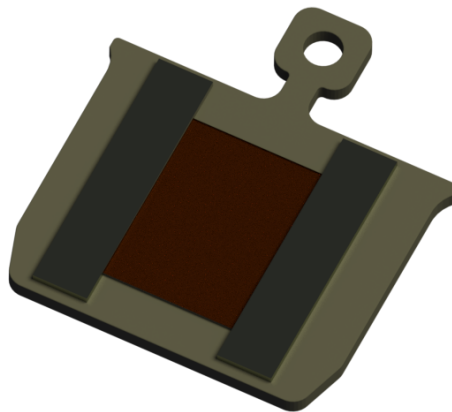
Published online: November 27, 2018

- [1] S. Ichinokura, K. Sugawara, A. Takayama, T. Takahashi, S. Hasegawa, *ACS Nano* **2016**, *10*, 2761.
- [2] J. Chapman, Y. Su, C. A. Howard, D. Kundys, A. N. Grigorenko, F. Guinea, A. K. Geim, I. V. Grigorieva, R. R. Nair, *Sci. Rep.* **2016**, *6*, 23254.
- [3] M. Bianchi, E. D. L. Rienks, S. Lizzit, A. Baraldi, R. Balog, L. Hornekær, P. Hofmann, *Phys. Rev. B* **2010**, *81*, 041403(R).
- [4] D. Haberer, L. Petaccia, A. V. Fedorov, C. S. Praveen, S. Fabris, S. Piccinin, O. Vilkov, D. V. Vyalikh, A. Preobrazhenskiy, N. I. Verbitskiy, H. Shiozawa, J. Fink, M. Knupfer, B. Büchner, A. Grüneis, *Phys. Rev. B* **2013**, *88*.
- [5] A. V. Fedorov, N. I. Verbitskiy, D. Haberer, C. Struzzi, L. Petaccia, D. Usachov, O. Y. Vilkov, D. V. Vyalikh, J. Fink, M. Knupfer, B. Büchner, A. Grüneis, *Nat. Commun.* **2014**, *5*, 1-2,5-6.
- [6] N. I. Verbitskiy, A. V. Fedorov, C. Tresca, G. Profeta, L. Petaccia, B. V. Senkovskiy, D. Y. Usachov, D. V. Vyalikh, L. V. Yashina, A. A. Eliseev, T. Pichler, A. Grüneis, *2D Mater.* **2016**, *3*, 045003.
- [7] J. Kleeman, K. Sugawara, T. Sato, T. Takahashi, *J. Phys.: Condens. Matter* **2016**, *28*, 204001.
- [8] D. Y. Usachov, A. V. Fedorov, O. Y. Vilkov, I. I. Ogorodnikov, M. V. Kuznetsov, A. Grüneis, C. Laubschat, D. V. Vyalikh, *Phys. Rev. B* **2018**, *97*, 085132.
- [9] M. Hell, N. Ehlen, B. V. Senkovskiy, H. Hasdeo, A. V. Fedorov, D. Dombrowski, C. Busse, T. Michely, G. Di Santo, L. Petaccia, R. Saito, A. Grüneis, *Nano Lett.* **2018**, *18*, 6045.
- [10] S. Bae, H. Kim, Y. Lee, X. Xu, J. S. Park, Y. Zheng, J. Balakrishnan, T. Lei, H. R. Kim, Y. I. Song, Y. J. Kim, K. S. Kim, B. Zyilmaz, J. H. Ahn, B. H. Hong, S. Iijima, *Nat. Nanotechnol.* **2010**, *5*, 574.
- [11] E. Miniussi, C. Bernard, H. Y. Cun, B. Probst, D. Leuenberger, G. Mette, W. D. Zabka, M. Weinl, M. Haluska, M. Schreck, J. Osterwalder, T. Greber, *J. Phys.: Condens. Matter* **2017**, *29*, 475001.
- [12] L. Gao, W. Ren, H. Xu, L. Jin, Z. Wang, T. Ma, L. P. Ma, Z. Zhang, Q. Fu, L. M. Peng, X. Bao, H.-M. Cheng, *Nat. Commun.* **2012**, *3*, 699.
- [13] T. Ciuk, I. Pasternak, A. Krajewska, J. Sobieski, P. Caban, J. Szmids, W. Strupinski, *J. Phys. Chem. C* **2013**, *117*, 20833.
- [14] V. Babenko, A. T. Murdock, A. A. Kóos, J. Britton, A. Crossley, P. Holdway, J. Moffat, J. Huang, J. A. Alexander-Webber, R. J. Nicholas, N. Grobert, *Nat. Commun.* **2015**, *6*, 7536.
- [15] J. Sun, S. Deng, W. Guo, Z. Zhan, J. Deng, C. Xu, X. Fan, K. Xu, W. Guo, Y. Huang, X. Liu, *J. Nanomater.* **2016**, *2016*, 1.
- [16] S. Koh, Y. Saito, H. Kodama, A. Sawabe, *Appl. Phys. Lett.* **2016**, *109*, 023105.
- [17] D. Ma, J. Shi, Q. Ji, K. Chen, J. Yin, Y. Lin, Y. Zhang, M. Liu, Q. Feng, X. Song, X. Guo, J. Zhang, Y. Zhang, Z. Liu, *Nano Res.* **2015**, *8*, 3662.
- [18] S. Y. Yang, J. G. Oh, D. Y. Jung, H. Choi, C. H. Yu, J. Shin, C. G. Choi, B. J. Cho, S. Y. Choi, *Small* **2014**, *11*, 175.
- [19] S. Unarunotai, Y. Murata, C. E. Chialvo, H. Sik Kim, S. MacLaren, N. Mason, I. Petrov, J. A. Rogers, *Appl. Phys. Lett.* **2009**, *95*, 202101.
- [20] J. H. Lee, E. K. Lee, W. J. Joo, Y. Jang, B. S. Kim, J. Y. Lim, S. H. Choi, S. J. Ahn, J. R. Ahn, M. H. Park, C. W. Yang, B. L. Choi, S. W. Hwang, D. Whang, *Science* **2014**, *344*, 286.
- [21] A. Castellanos-Gomez, M. Buscema, R. Molenaar, V. Singh, L. Janssen, H. S. J. van der Zant, G. A. Steele, *2D Mater.* **2014**, *1*, 011002.
- [22] L. Banszerus, M. Schmitz, S. Engels, J. Dauber, M. Oellers, F. Haupt, K. Watanabe, T. Taniguchi, B. Beschoten, C. Stampfer, *Sci. Adv.* **2015**, *1*, e1500222.
- [23] F. Pizzocchero, L. Gammelgaard, B. S. Jessen, J. M. Caridad, L. Wang, J. Hone, P. Bggild, T. J. Booth, *Nat. Commun.* **2016**, *7*, 11894.
- [24] C. T. Cherian, F. Giustiniano, I. Martin-Fernandez, H. Andersen, J. Balakrishnan, B. Özyilmaz, *Small* **2014**, *11*, 189.
- [25] C. J. L. de la Rosa, N. Lindvall, M. T. Cole, Y. Nam, M. Löffler, E. Olsson, A. Yurgens, *Appl. Phys. Lett.* **2013**, *102*, 022101.
- [26] M. Petrović, I. Šrut Rakić, S. Runte, C. Busse, J. T. Sadowski, P. Lazić, I. Pletikosić, Z. H. Pan, M. Milun, P. Pervan, N. Atodiresel, R. Brako, D. Sokcevic, T. Valla, T. Michely, M. Kralj, *Nat. Commun.* **2013**, *4*, 2772.
- [27] A. T. N'Diaye, M. Engler, C. Busse, D. Wall, N. Buckanie, F. J. M. zu Heringdorf, R. van Gastel, B. Poelsema, T. Michely, *New J. Phys.* **2009**, *11*, 023006.
- [28] M. Kralj, I. Pletikosić, M. Petrović, P. Pervan, M. Milun, A. T. N'Diaye, C. Busse, T. Michely, J. Fujii, I. Vobornik, *Phys. Rev. B* **2011**, *84*, 075427.
- [29] H. Hattab, A. T. N'Diaye, D. Wall, C. Klein, G. Jnawali, J. Coraux, C. Busse, R. van Gastel, B. Poelsema, T. Michely, F. J. M. zu Heringdorf, M. H. von Hoegen, *Nano Lett.* **2012**, *12*, 678.
- [30] A. Grüneis, B. Senkovskiy, A. Fedorov, M. Hell, S. Michel, in *Encyclopedia of Interfacial Chemistry – Surface Science and Electrochemistry* (Ed: K. Wandelt), ISBN 978-0-12-409547-2, Elsevier, Amsterdam, The Netherlands **2018**, pp. 367–374.
- [31] D. Y. Usachov, V. Y. Davydov, V. S. Levitskii, V. O. Shevelev, D. Marchenko, B. V. Senkovskiy, O. Y. Vilkov, A. G. Rybkin, L. V. Yashina, E. V. Chulkov, I. Y. Sklyadneva, R. Heid, K. P. Bohnen, C. Laubschat, D. V. Vyalikh, *ACS Nano* **2017**, *11*, 6336.
- [32] I. Calizo, I. Bejenari, M. Rahman, G. Liu, A. A. Balandin, *J. Appl. Phys.* **2009**, *106*, 043509.
- [33] H. L. Liu, S. Siregar, E. H. Hasdeo, Y. Kumamoto, C. C. Shen, C. C. Cheng, L. J. Li, R. Saito, S. Kawata, *Carbon* **2015**, *81*, 807.
- [34] E. Grånäs, J. Knudsen, U. A. Schröder, T. Gerber, C. Busse, M. A. Arman, K. Schulte, J. N. Andersen, T. Michely, *ACS Nano* **2012**, *6*, 9951.
- [35] E. Starodub, A. Bostwick, L. Moreschini, S. Nie, F. E. Gabaly, K. F. McCarty, E. Rotenberg, *Phys. Rev. B* **2011**, *83*, 125428.
- [36] K. Verguts, K. Schouteden, C. H. Wu, L. Peters, N. Vrancken, X. Wu, Z. Li, M. Erkens, C. Porret, C. Huyghebaert, et al. *ACS Appl. Mater. Interfaces* **2017**, *9*, 37484.
- [37] B. V. Senkovskiy, M. Pfeiffer, S. K. Alavi, A. Bliesener, J. Zhu, S. Michel, A. V. Fedorov, R. German, D. Hertel, D. Haberer, L. Petaccia, F. R. Fischer, K. Meerholz, P. H. M. van Loosdrecht, K. Lindfors, A. Grüneis, *Nano Lett.* **2017**, *7*, 4029.
- [38] M. Lafkoti, B. Krauss, T. Lohmann, U. Zschieschang, H. Klauk, K. v. Klitzing, J. H. Smet, *Nano Lett.* **2010**, *10*, 1149.
- [39] Z. Li, I. A. Kinloch, R. J. Young, K. S. Novoselov, G. Anagnostopoulos, J. Parthenios, C. Galiotis, K. Papagelis, C. Y. Lu, L. Britnell, *ACS Nano* **2015**, *9*, 3917.
- [40] I. Miccoli, F. Edler, H. Pfner, C. Tegenkamp, *J. Phys.: Condens. Matter* **2015**, *27*, 223201.
- [41] W. Versnel, *Solid-State Electron.* **1979**, *22*, 911.

Chapter 3

Further publications

3.1 Facile preparation of $\text{Au}(111)$ /mica substrates for high-quality graphene nanoribbon synthesis



Phys. Status Solidi B 253, No. 12, 2362–2365 (2016) / DOI 10.1002/pssb.201600254



Facile preparation of Au(111)/mica substrates for high-quality graphene nanoribbon synthesis

M. G. Hell,^{*,1} B. V. Senkovskiy¹, A. V. Fedorov¹, A. Nefedov², C. Wöll², and A. Grüneis¹

¹ II. Physikalisches Institut, Universität zu Köln, Zùlpicher Str. 77, 50937 Köln, Germany

² Institut für Funktionelle Grenzflächen, Karlsruher Institut für Technologie, Hermann-von-Helmholtz-Platz 1, 76344 Eggenstein-Leopoldshafen, Germany

Received 22 April 2016, revised 26 June 2016, accepted 12 July 2016
Published online 8 August 2016

Keywords graphene nanoribbons, DBBA, Au(111), XPS, NEXAFS, Raman

* Corresponding author: e-mail hell@ph2.uni-koeln.de, Phone: +49-221-4707078, Fax: +49-221-4705178

A setup for the preparation of oriented Au(111)/mica thin films of ~ 100 nm thickness as an active substrate for graphene nanoribbon growth is shown. Low-energy electron diffraction shows that the Au(111) thin films have a single crystallographic orientation over the whole surface area. Graphene nanoribbons are synthesized by the bottom-up approach via surface polymerization of precursor molecules that are evaporated onto the catalytically active Au(111)/mica substrate. The graphene nanoribbons are investigated by a combination of resonance Raman,

X-ray photoemission spectroscopy, and near-edge X-ray absorption fine structure spectroscopy confirming a nanoribbon quality equal to nanoribbons grown on commercially available single-crystal Au(111) substrates. The present work, therefore, establishes the *insitu* preparation of Au(111)/mica as an inexpensive and simple method to prepare substrates of desired shape and thickness for surface polymerization reactions which are of interest to a growing community of researchers working on graphene nanoribbons.

© 2016 WILEY-VCH Verlag GmbH & Co. KGaA, Weinheim

1 Introduction Carbon nanomaterials have been in the focus of condensed matter physics for a long time already. Following fullerenes, nanotubes, and graphene the latest member of this materials' family are graphene nanoribbons which are receiving lots of attention [1–4]. Ultranarrow graphene nanoribbons (GNRs) are ~ 1 nm wide stripes of graphene with defined edges (zig-zag or armchair). They can be produced in high-quality by bottom-up nanotechnology [2]. A large variety in structures can be engineered by simply varying the precursor molecule. Probably, the best studied is the surface polymerization of 10,10-dibromo-9,9-bianthryl (DBBA) molecules which yields armchair graphene nanoribbons with a width of 7 atoms (7-AGNRs) [2, 5]. Modifications of the precursor molecule has successfully allowed for the bottom up synthesis of boron [6, 7] and sulfur-doped nanoribbons [8]. Moreover, varying the width of the precursor molecules changes the nanoribbon width and hence allows for band-gap engineering. For any of the precursors, surface polymerization can be obtained on atomically flat Au(111), Ag(111), or Cu(111) surfaces [2, 9, 10] (or their vicinal cuts such as Au(788) [11]). Single crystals have

been used extensively for nanoribbon synthesis; however, their high cost is prohibitive for high-yield and scalable growth on an industrial scale. Nevertheless, an atomically flat metal surface is needed to achieve reproducible and high-quality nanoribbon synthesis. The present manuscript addresses these needs. Here, we show that the application of a well-known recipe for growth of Au(111) on muscovite mica [12] provides surfaces that can be synthesized in-situ and are inexpensive and easy-to-prepare.

2 Synthesis The Au(111)/mica synthesis was performed in a small growth chamber under high vacuum conditions with the base pressure $p < 10^{-6}$ mbar. After Au(111) growth these substrates have been transferred in air into an ultra-high-vacuum (UHV) preparation chamber where the in-situ GNR synthesis and spectroscopy was performed. Prior to the GNR growth the Au(111) surfaces were gently annealed at 200 °C to remove contaminants from the air exposure.

In Fig. 1a, we show the core of the setup for preparation of Au(111)/mica. It is a homebuilt sample manipulator which consists of a sample pocket, thermocouple, and a

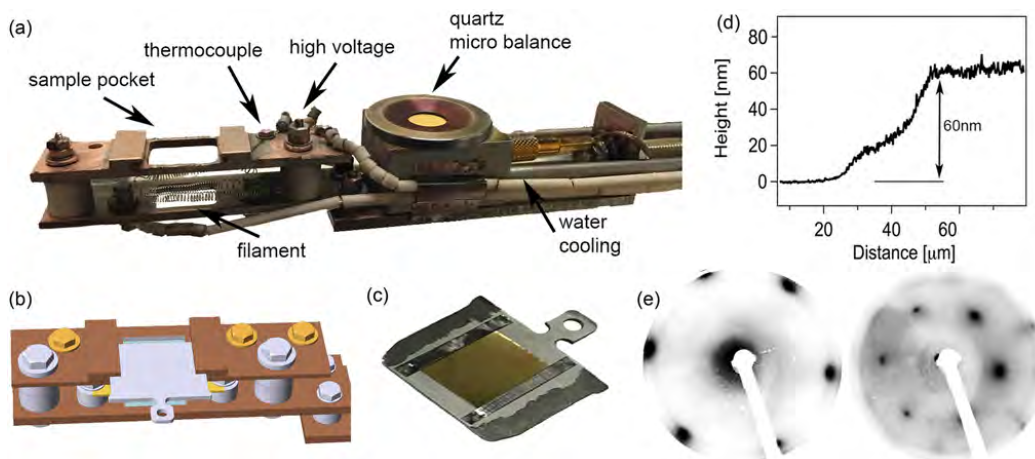


Figure 1 (a) Homebuilt sample manipulator with empty sample pocket, filament, and high voltage for e-beam heating, thermocouple, and water cooled quartz microbalance, (b) schematics of a sample inserted into the sample pocket, (c) mica after deposition of Au, (d) AFM measurement of Au(111) height on mica across the location of the Ta stripe, (e) LEED diffraction pattern of Au(111)/mica at 50 and 70 eV.

water cooled quartz microbalance. Figure 1b depicts a sketch of how the sample plate (an Omicron type plate made out of Mo) can be inserted into the sample pocket. To prepare an Au(111) film we first mount a freshly ex-situ cleaved mica on the sample plate using Ta stripes, place into the sample pocket and evacuate it to a pressure lower than 10^{-6} mbar. We then clean and degas the sample by annealing to 300°C for at least 12 h. Hereafter, the mica is annealed to 500°C for ~ 1 min in order to remove contaminants. To obtain thick Au layer, the evaporator was placed close (about 5 cm) in front of the sample manipulator. The Au atom flux is calibrated conveniently just before deposition by a quartz microbalance and mounted above the sample pocket (see Fig. 1a). It is known [12] that for crystalline Au growth the mica must be kept at 300°C during deposition. We found that the Au deposition rate must be at least 0.5 \AA s^{-1} in order to obtain low energy electron diffraction (LEED) spots. After Au deposition the sample is annealed for 12 h at 300°C . Figure 1c depicts a photograph of an Au/mica film. Atomic force microscopy (AFM) enables precise thickness measurements and we have used AFM in order to calibrate the quartz microbalance tooling factor.

Figure 1d shows an atomic force microscopy (AFM) scan across the edge of the Au film [13]. The edge was defined by the Ta stripe and, therefore, not perfectly sharp as some Au can grow underneath the stripe close to its edge. AFM allows to measure the thickness of the Au film which is defined by the height difference of the region under the Ta stripe to the maximum. An Au film prepared in such a way does not show a sharp pattern in low-energy electron diffraction (LEED). Hence, such films are not ordered. In order to obtain a sharp LEED, a second annealing step at a temperature of 600°C is needed. This will cause the structuring of the Au(111)

sample. The duration of the last annealing step is depending on the thickness of the sample. For a regular sample of 50–100 nm, a duration of 30 min is sufficient. Hereafter, we were able to identify a sharp LEED pattern with a sixfold rotational symmetry which we ascribe to the Au(111) surface structure. Two typical LEED patterns for electron energies of 50 and 70 eV taken prior to molecular deposition are shown in Fig. 1e, correspondingly. By scanning the sample across the LEED spot, we could verify that the LEED pattern does not change. This indicates that all domains have the same orientation in the topmost atom layers.

The synthesis of GNRs was performed by evaporation of DBBA molecules onto a freshly prepared Au(111) surface, followed by annealing steps. The DBBA was evaporated from a quartz crucible using a homebuilt organics evaporator with a thermocouple attached to the molecule reservoir. The deposition rate was controlled using a quartz microbalance. About 10 \AA of precursor molecules (using the graphite density and Z-factor) were evaporated onto the Au surface which was kept at room-temperature. Effectively only a part of the DBBA will form ribbons and the remainder will simply sublime. This is due to a weaker bonding between molecules to each other with respect to the molecule-substrate bond. In order to carry out DBBA debromination and cyclodehydrogenation reactions, the temperatures must be known quite precisely (to an accuracy better than 5°C) and annealing has to be carried out slowly. We have therefore calibrated this curve not with the thermocouple shown in Fig. 2a, instead we have spot-welded a thermocouple onto an empty sample holder and recorded the temperature directly where usually the mica is located. Figure 2a shows the curve of temperature versus time we have used to synthesize graphene nanorib-



2364

M. Hell et al.: Facile preparation of Au(111)/mica substrates for high-quality GNR synthesis

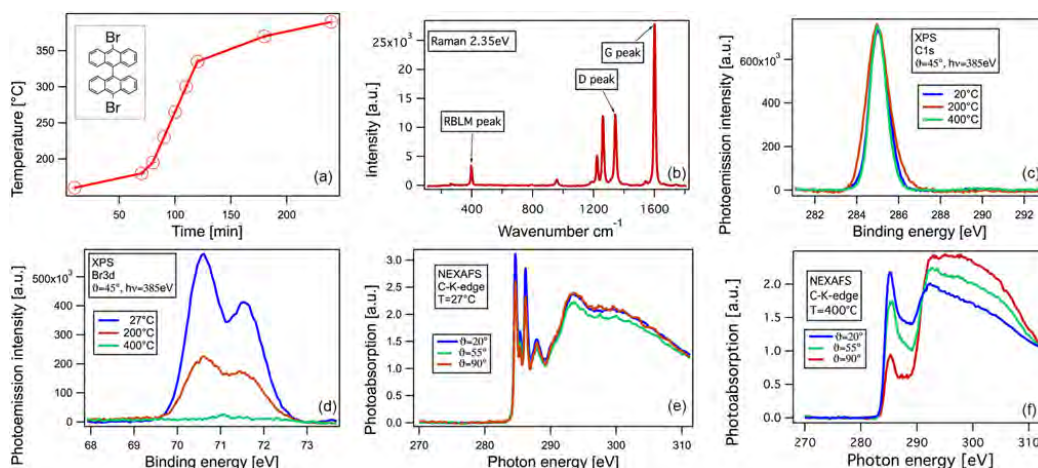


Figure 2 (a) Temperature programmed GNR synthesis performed with a programmable power supply, (b) Raman spectrum of 7-AGNRs on Au(111) measured with a 2.35 eV laser, (c,d) XPS spectra of C1s and Br3d core levels, (e,f) NEXAFS spectra of deposited DBBA molecules immediately after deposition and after annealing to 400 °C.

bons from a 10 Å thick DBBA film/Au(111)/mica. The inset to Fig. 2a depicts a sketch of the DBBA molecule.

3 Results The straightforward way to proof the formation of GNRs is resonance Raman spectroscopy. GNRs have a radial-breathing like mode at low energies (397 cm^{-1}) for 7-AGNR [2]) which is their fingerprint. Due to the high resonance enhancement that occurs if the laser energy used matches the separation of van-Hove-singularities in the density of electronic states, very strong Raman spectra from sub-monolayer coverages of ribbons can be obtained easily. The E_{22} resonance transition for 7-AGNRs can be excited by a 2.35 eV laser [14]. Figure 2b depicts the Raman spectra obtained. It can be seen that all GNR related modes appear. In particular, the defect induced D band is even lower than of most GNRs synthesized on single crystal substrates [2].

Then, we turn to the X-ray photoemission spectroscopy (XPS) measurements on C and Br core levels which have been carried out at the HESGM beamline of the BESSY II synchrotron (Helmholtz-Zentrum Berlin, Germany). Figures 2c and d depict the C1s and Br3d core levels during three annealing steps (room temperature, 200 and 400 °C). The photon energy used was set to $h\nu = 385\text{ eV}$. It can be seen that the intensity for C1s is not changing during polymerization and a lot of the Br3d intensity vanishes after the first annealing step of 200 °C. Further annealing to 400 °C causes all Br3d intensity to disappear, indicating that the Br has left the Au surface and that all the molecules are now either in their radical form with dangling C atoms or already polymerized.

After that near edge X-ray absorption fine structure (NEXAFS) spectroscopy have been performed in partial

yield mode. Figure 2e depicts the C K-edge NEXAFS spectra measured at three different incidence angles on DBBA molecules deposited on Au before annealing. The sharp features at the photon energy range 284–290 eV are related to transitions from the C1s core levels to the unoccupied π^* molecular orbitals. Since a significant angle dependence is absent, we can conclude that the precursor molecules are disordered or partially twisted with a small tendency to planar orientation. After annealing up to 400 °C, a drastic change in the electronic structure takes place. The corresponding NEXAFS spectra are shown in Fig. 2f. Firstly, the sharp peaks in the π^* resonance at 285 eV disappear and a rather broad peak appears. Secondly, the angle dependence of this new peak as well as of σ^* resonances now much stronger. In particular the π^* related peak around 285 eV has a minimum and σ^* related peaks at the photon energy range 290–310 eV have a maximum for normal incidence (90°, the electric field vector is parallel to the ribbon plane). This angle dependence indicates that the GNRs are lying planar on the surface after cyclodehydrogenation.

4 Conclusions In summary, we have shown an inexpensive and simple method to prepare high quality disposable Au(111)/mica substrates for the surface polymerization of graphene nanoribbons using a molecular precursor. The spectroscopic investigation of GNR samples grown on this substrate indicates that the GNRs have spectra identical to those obtained from single crystal substrates. This has been checked using Raman spectroscopy, XPS, and NEXAFS. The Au(111)/mica substrates are much cheaper than the single crystals, and, thus, can be used for experiments, that are harmful for substrates (e.g., chemical treatment and

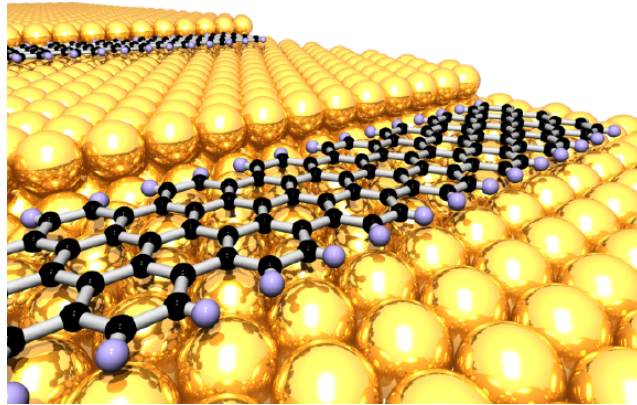
functionalization or transferring the GNRs on to the insulators/semiconductors). The method introduced here is important for the growing GNRs community which wishes to synthesize GNRs on purpose made substrates.

Acknowledgements M.H., B.S., and A.G. acknowledge the ERC grant no. 648589 “SUPER-2D”, funding from Quantum Matter and Materials and DFG project GR 3708/2-1. A.N. and C.W. acknowledge funding from the Science and Technology of Nanosystems program. We also thank Helmholtz Zentrum Berlin for the beamtime allocation.

References

- [1] L. Grill, M. Dyer, L. Lafferentz, M. Persson, M. V. Peters, and S. Hecht, *Nature Nanotechnol.* **2**, 687–691 (2007).
- [2] J. Cai, P. Ruffieux, R. Jaafar, M. Bieri, T. Braun, S. Blankenburg, M. Muoth, A. P. Seitsonen, M. Saleh, X. Feng, K. Müllen, and R. Fasel, *Nature* **466**(7305), 470–473 (2010).
- [3] Z. Chen, Y. M. Lin, M. J. Rooks, and P. Avouris, *Physica E: Low-dimens. Syst. Nanostruct.* **40**(2), 228–232 (2007), International Symposium on Nanometer-Scale Quantum Physics.
- [4] P. Ruffieux, J. Cai, N. C. Plumb, L. Patthey, D. Prezzi, A. Ferretti, E. Molinari, X. Feng, K. Müllen, C. A. Pignedoli, and R. Fasel, *ACS Nano* **6**(8), 6930–6935 (2012).
- [5] A. Narita, X. Feng, and K. Müllen, *Chem. Rec.* **15**(1), 295–309 (2014).
- [6] S. Kawai, S. Saito, S. Osumi, S. Yamaguchi, A. S. Foster, P. Spijker, and E. Meyer, *Nature Commun.* **6**, 8098 (2015).
- [7] R. R. Cloke, T. Marangoni, G. D. Nguyen, T. Joshi, D. J. Rizzo, C. Bronner, T. Cao, S. G. Louie, M. F. Crommie, and F. R. Fischer, *J. Am. Chem. Soc.* **137**(28), 8872–8875 (2015).
- [8] G. D. Nguyen, F. M. Toma, T. Cao, Z. Pedramrazi, C. Chen, D. J. Rizzo, T. Joshi, C. Bronner, Y. C. Chen, M. Favaro, S. G. Louie, F. R. Fischer, and M. F. Crommie, *J. Phys. Chem. C* **120**(5), 2684–2687 (2016).
- [9] K. A. Simonov, N. A. Vinogradov, A. S. Vinogradov, A. V. Generalov, E. M. Zagrebina, N. Mårtensson, A. A. Cafolla, T. Carpy, J. P. Cunniffe, and A. B. Preobrajenski, Growth and structure of graphene nanoribbons on substrates with different reactivity, www.maxlab.se
- [10] K. A. Simonov, N. A. Vinogradov, A. S. Vinogradov, A. V. Generalov, E. M. Zagrebina, G. I. Svirskiy, A. A. Cafolla, T. Carpy, J. P. Cunniffe, T. Taketsugu, A. Lyalin, N. Mårtensson, and A. B. Preobrajenski, *ACS Nano* **9**(9), 8997–9011 (2015).
- [11] S. Linden, D. Zhong, A. Timmer, N. Aghdassi, J. H. Franke, H. Zhang, X. Feng, K. Müllen, H. Fuchs, L. Chi, and H. Zacharias, *Phys. Rev. Lett.* **108**(21) (2012).
- [12] R. Colton, W. Ebeling, J. Frommer, H. Gaub, A. Gewirth, R. Guckenberger, and J. Rabe, *Procedures in Scanning Probe Microscopies* (Wiley, New York, 1998), ISBN-13: 978-0471959120.
- [13] W. B. Caldwell, K. Chen, B. R. Herr, C. A. Mirkin, J. C. Hulst, and R. P. V. Duyne, *Langmuir* **10**(11), 4109–4115 (1994).
- [14] F. Krakau, Synthesis and electronic properties of graphene nanoribbons, Bachelor thesis, University of Cologne, 2014.

3.2 Semiconductor-to-Metal Transition and Quasi-particle Renormalization in Doped Graphene Nanoribbons



Semiconductor-to-Metal Transition and Quasiparticle Renormalization in Doped Graphene Nanoribbons

Boris V. Senkovskiy, Alexander V. Fedorov, Danny Haberer, Mani Farjam, Konstantin A. Simonov, Alexei B. Preobrajenski, Niels Mårtensson, Nicolae Atodiresei, Vasile Caciuc, Stefan Blügel, Achim Rosch, Nikolay I. Verbitskiy, Martin Hell, Daniil V. Evtushinsky, Raphael German, Tomas Marangoni, Paul H. M. van Loosdrecht, Felix R. Fischer,* and Alexander Grüneis**

A semiconductor-to-metal transition in $N = 7$ armchair graphene nanoribbons causes drastic changes in its electron and phonon system. By using angle-resolved photoemission spectroscopy of lithium-doped graphene nanoribbons, a quasiparticle band gap renormalization from 2.4 to 2.1 eV is observed. Reaching high doping levels (0.05 electrons per atom), it is found that the effective mass of the conduction band carriers increases to a value equal to the free electron mass. This giant increase in the effective mass by doping is a means to enhance the density of states at the Fermi level which can have palpable impact on the transport and optical properties. Electron doping also reduces the Raman intensity by one order of magnitude, and results in relatively small (4 cm^{-1}) hardening of the G phonon and softening of the D phonon. This suggests the importance of both lattice expansion and dynamic effects. The present work highlights that doping of a semiconducting 1D system is strikingly different from its 2D or 3D counterparts and introduces doped graphene nanoribbons as a new tunable quantum material with high potential for basic research and applications.

Graphene nanoribbons (GNRs) are promising materials for the production of nanoscale devices.^[1–5] In contrast to graphene, GNRs can be metallic or semiconducting with a tunable band gap that depends on the ribbon width and the edge configuration.^[6–10] Carbon nanotubes are a similar 1D material but despite a 20 year history, the large-area synthesis of monochiral carbon nanotubes remains challenging.^[11] On the other hand, nanoribbons can be fabricated with atomically controlled precision thanks to the bottom-up nanofabrication techniques.^[12–20] Thus, GNRs combine the best attributes of the nanotube and graphene worlds.

Engineering of GNR-based optoelectronic devices requires an understanding of the charge transfer effect on the

Dr. B. V. Senkovskiy, Dr. A. V. Fedorov, Dr. N. I. Verbitskiy,
M. Hell, R. German, Prof. P. H. M. van Loosdrecht, Prof. A. Grüneis
II. Physikalisches Institut
Universität zu Köln
Zùlpicher Strasse 77, Köln 50937, Germany
E-mail: senkovskiy@ph2.uni-koeln.de; grüneis@ph2.uni-koeln.de

Dr. A. V. Fedorov
St. Petersburg State University
Ulyanovskaya ul. 1, St. Petersburg 198504, Russia

Dr. A. V. Fedorov
IFW-Dresden
Dresden
Helmholtzstraße 20, 01069, Germany

Dr. D. Haberer, Dr. T. Marangoni, Prof. F. R. Fischer
University of California at Berkeley
699, Tan Hall, Berkeley, CA 94720, USA
E-mail: ffisher@berkeley.edu

Dr. M. Farjam
School of Nano Science
Institute for Research in Fundamental Sciences (IPM)
P.O. Box 19395-5531, Tehran, Iran

Dr. K. A. Simonov, Prof. N. Mårtensson
Department of Physics and Astronomy
Uppsala University
Box 516, Uppsala 75120, Sweden

DOI: 10.1002/aeml.201600490

Dr. K. A. Simonov, Dr. A. B. Preobrajenski
MAX IV
Lund University
Box 118, Lund 22100, Sweden

Dr. N. Atodiresei, Dr. V. Caciuc, Prof. S. Blügel
Peter Grünberg Institut (PGI-1) and Institute
for Advanced Simulation (IAS-1)
Forschungszentrum Jülich and JARA
Jülich D-52425, Germany

Prof. A. Rosch
Institute for Theoretical Physics
Universität zu Köln
Zùlpicher Strasse 77, Köln 50937, Germany

Dr. N. I. Verbitskiy
Faculty of Physics
University of Vienna
Strudlhofgasse 4, Vienna A-1090, Austria

Dr. N. I. Verbitskiy
Department of Materials Science
Moscow State University
Leninskiye Gory 1/3, Moscow 119992, Russia

Dr. D. V. Evtushinsky
Helmholtz-Zentrum Berlin für Materialien und Energie
Elektronenspeicherring BESSY II
Albert-Einstein-Strasse 15, Berlin 12489, Germany



electronic and optical properties of GNRs. This effect could be large taking into account the importance of many-body physics for low-dimensional materials. For example, charge transfer induced many-body interactions have been theoretically predicted for semiconducting quantum wells,^[21] carbon nanotubes,^[22] and 2D layers.^[23] The inclusion of electron–electron interactions in GNRs in the framework of the “GW” approximation leads to a larger QP band gap,^[7,24,25] which can be significantly reduced by screening from a metallic substrate.^[26] Similarly, as the charge carrier density is increased, one might expect stronger screening of the Coulomb interactions and as a consequence a smaller band gap. Thus, charge doping of GNRs could be an efficient tool to manipulate many-body interaction and to control their optical and electronic properties. Indeed, for carbon nanotubes there is experimental evidence for a band gap renormalization upon charge doping.^[27–30] Moreover, it has been put forward by theory that the dynamical screening due to acoustic charge carrier plasmons, which have a unique contribution in a 1D system, also leads to the effective mass renormalization in semiconducting nanotubes upon a transition to the metallic state.^[22] The band gap and the charge-carrier effective mass determine the optical, electronic, and thermal properties of the material. However, the full picture of the quasiparticle (QP) renormalization in a 1D material caused by charge doping has not been experimentally proven.

To shed light on this issue we perform electron doping of aligned $N=7$ armchair graphene nanoribbons (7-AGNRs) using lithium atoms as a charge donor. A multitechnique approach is a key that allows us to gather a complete picture of the physical properties of doped GNRs. First, we apply angle-resolved photoemission spectroscopy (ARPES) to directly observe the renormalization of their electronic band structure upon doping. Second, by X-ray photoemission spectroscopy (XPS) and near edge X-ray absorption fine structure (NEXAFS) spectroscopy we show that lithium does not distort the ribbon's structure and that the antibonding π^* states are filled with electrons. Then, the experimental data are compared against density functional theory (DFT) calculations of the electron energy band structure without explicit inclusion of many-body interactions. Finally, we apply ultrahigh vacuum (UHV) Raman spectroscopy and

show a transition from resonance to off-resonance Raman and phonon energy renormalization in Li-doped GNRs.

The unprecedented structural quality of massively parallel 7-AGNRs uniformly aligned on the vicinal surface of Au(788) single crystal and their flatness opens up the use of powerful spectroscopic methods such as ARPES.^[26,31] Figure 1 shows the second derivative of the ARPES intensity maps (raw data are shown in the Supporting Information) measured in the direction parallel to the axis of the 7-AGNRs. The second derivative method is used to enhance the band features. Three parabola-like electronic valence sub-bands of pristine 7-AGNRs can be clearly seen in Figure 1a. Using parabolic fits of the raw ARPES data at the band maxima we determined the position of the valence band maximum (VBM) $E_{V1} = 0.88$ eV and the effective mass at the VBM $m_{V1}^* = -0.23 m_e$ (here m_e indicates the free electron mass and V_1 is the first valence sub-band). Our value for m_{V1}^* is in good agreement to the work of ref. [26] ($-0.21 m_e$). The values of the energies E_{V2} and E_{V3} and corresponding effective masses m_{V2}^* and m_{V3}^* are given in the caption of Figure 1.

Figure 1b shows that after in situ deposition of one monolayer (ML) of Li the valence band shifts down by 1.33 ± 0.05 eV and higher photoemission intensity appears at the Fermi level. This feature is assigned to the conduction band of Li-doped 7-AGNRs. The energy separation between valence and conduction bands was found to be about 2.1 eV. Interestingly, this value is significantly lower than the band gaps measured by STS for 7-AGNRs on Au(111): 2.7,^[32] 2.3,^[26] 2.5,^[14] and 2.37 eV.^[33] Our scanning tunneling spectroscopy (STS) data, shown in the Supporting Information, provide the same band gap for 7-AGNRs on Au(788) and on Au(111): 2.4 eV, which is in a good agreement with the previous works. It is important to point out that a precise STS measurement of Li-doped nanoribbons is hampered by the prohibitively high Li mobility. The difference between the band gaps obtained by ARPES and STS is equal to the self-energy corrections due to charge transfer doping and can directly be compared to the theoretical predictions. Our analysis relies on the fact that STS and ARPES reveal identical energy band dispersions which has been explicitly shown for GNRs.^[34] A similar approach of comparing STS derived QP band gap and the optical gap of MoSe₂ monolayers

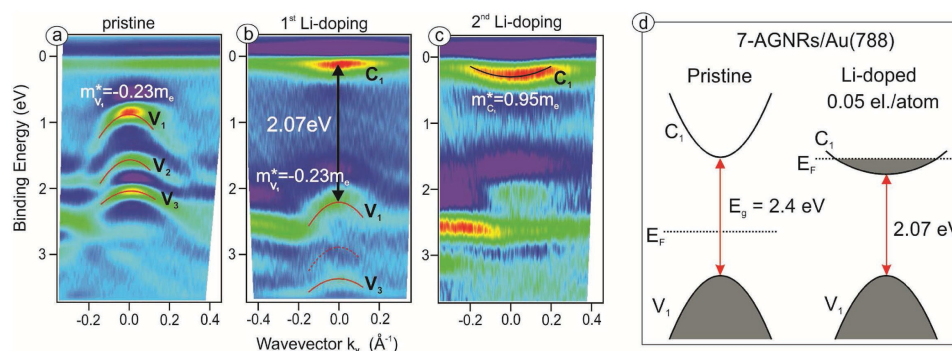


Figure 1. ARPES data (second derivative) of aligned 7-AGNRs on Au(788) accumulated along the k_y direction with respect to the second Brillouin zone. a) Pristine 7-AGNRs. The maximum energies (effective masses) of V_1 , V_2 , and V_3 sub-bands are 0.88 eV ($-0.23 m_e$), 1.56 eV ($-0.23 m_e$), and 2.04 eV ($-0.41 m_e$), respectively. b) After first Li-doping (about 1 ML). The dashed parabola indicates where the V_2 sub-band should be (it is not visible due to the overlap with Au 5d states). c) After second Li-doping (about 2 ML). d) Illustration of the observed electronic band renormalization in Li-doped 7-AGNRs.

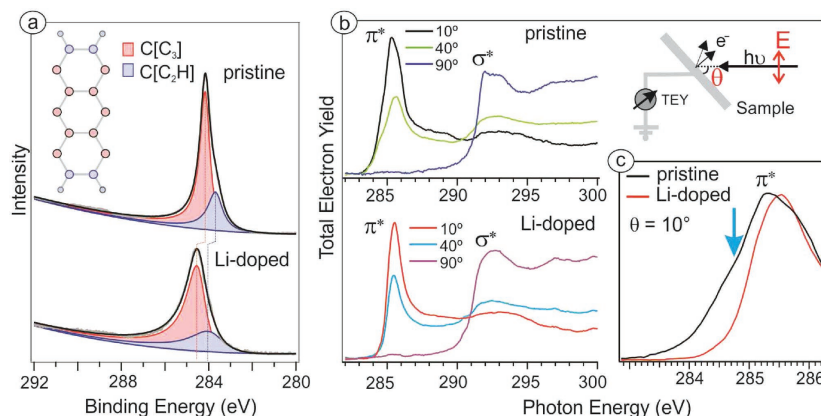


Figure 2. a) XPS spectra of the C1s core level of 7-AGNRs/Au(788) before and after deposition of 1 ML of Li, measured with 320 eV photon energy. b) Angle-dependent NEXAFS spectra of 7-AGNRs/Au(788) at the C K-edge probed by linearly polarized radiation before and after Li doping. A sketch of the experimental geometry is depicted in the inset. c) Close-up of the π^* resonance at grazing angle. The blue arrow indicates the disappearance of the low-energy shoulder after Li-doping.

has yielded the exciton binding energies directly.^[35] Thus, Li doping reduces the QP band gap by ≈ 300 meV.

In order to have a higher doping to reliably fit the effective mass of the conduction band, we have performed a second deposition of Li. Figure 1c shows the corresponding spectrum which clearly exhibits a parabola-like feature. This is the maximum doping level we achieved and the area of the 1D Brillouin zone (BZ), occupied by the conduction band below the Fermi level, suggests that the doping level is about 1.7 ± 0.1 electrons nm^{-1} or 0.05 electrons per carbon atom. The parabola-like dispersion of the conduction sub-band C_1 has a strikingly large value of the effective mass of $0.95 \pm 0.05 m_e$. From zone-folding we expect approximate electron-hole symmetry in the electronic structure of 7-AGNRs. Therefore, the absolute values of the effective masses of valence and conduction bands should be close to one another. This is also consistent with DFT results^[6,36,37] for undoped ribbons and with STS data.^[33] Recently, by means of Fourier transformed STS, the effective electron masses of V_1 and C_1 were also estimated for isolated 7-AGNRs on NaCl as 0.32 and 0.35 m_e , correspondingly.^[38] The value of the electron mass for the unoccupied conduction band is thus just slightly larger than the mass for the valence band. The experimentally observed mass renormalization approximately by a factor of four induced by electron doping is thus related to the strong electronic correlations that are present in 1D systems.^[22,29] Our observations regarding the electronic band renormalization in GNRs induced by Li doping are summarized in Figure 1d.

The observed QP renormalization in doped GNRs demands additional experimental confirmation. First, one has to be sure that the structure of GNRs does not suffer by chemical functionalization and we have the same material before and after the Li deposition. Second, the filling of the conduction band has to be proved.

We performed XPS studies of the C1s core level to analyze the chemical composition of Li-doped 7-AGNRs. Figure 2a depicts the C1s spectra of 7-AGNRs before and after Li doping.

Here, the C[C₃] component belongs to the carbon atoms having three neighboring carbons and C[C₂H] denotes the edge carbons with two carbon bonds and one hydrogen bond.^[39] After Li deposition, both components shift to higher binding energies by the same amount due to charge transfer. The intensity ratio of the two components before and after the doping is 5:2 as expected from the structure. This indicates a structural quality with no or very few missing hydrogen atoms along the edges.

To investigate possible corrugations of the 7-AGNRs as a result of Li adsorption we performed a NEXAFS spectroscopy study of pristine and doped samples. Moreover, NEXAFS measurements are sensitive to the occupation of the conduction band. The series of C K-edge absorption spectra of 7-AGNRs are shown in Figure 2b. The angle-dependent behavior of the π^* and σ^* resonances suggests a planar structure of ribbons before and after Li deposition. Figure 2c shows a zoom of the π^* region of the NEXAFS spectrum. The low-energy shoulder of the π^* resonance is clearly visible in the NEXAFS spectrum of pristine GNRs. However, after Li deposition it disappears. This is because the transition from the C1s core level to the lowest conduction band states is blocked after electron doping. Due to the element-specific nature of the NEXAFS method, this gives a proof of the occupation of the carbon derived π^* levels.

Here, by means of DFT, we investigate the impact of charge transfer and the presence of Li ions on the electronic band structure of 7-AGNRs. The calculations do not include many-body effects (such as electron-plasmon and electron-electron Coulomb interactions). Figure 3 depicts the DFT calculated 1D electron energy bands of pristine and Li-doped 7-AGNRs in the ground-state geometries together with the related structure configurations.

The configuration we consider in Figure 3b is one where the Li is placed above the center benzene ring of an anthracene unit. The second configuration shown in Figure 3c is one where two Li atoms are placed above the edge benzene rings

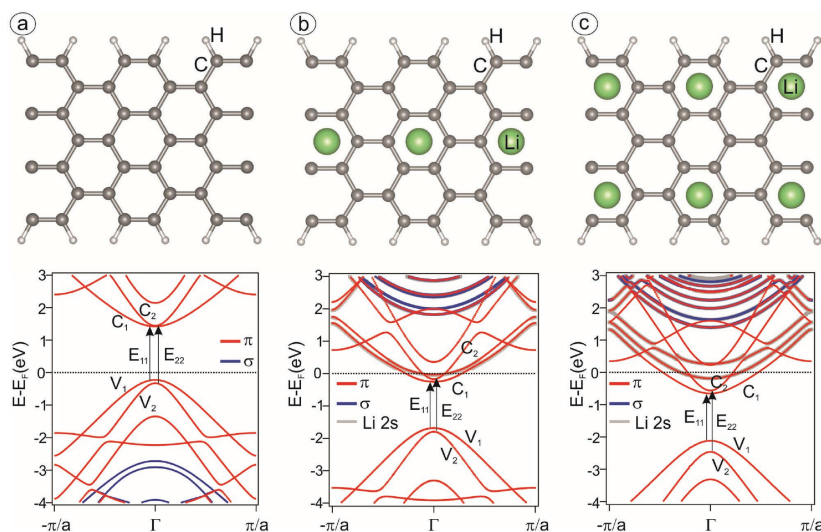


Figure 3. Electronic energy band structure and atomic structure of a) pristine and the ground state for b) one Li- and c) two Li-doped 7-AGNRs. The labels V_1 (V_2) and C_1 (C_2) depict the first (second) valence and conduction sub-bands, respectively. The red (blue) color indicates a π (σ) character of the respective band, the electronic bands with Li character are marked with gray. First and second transition energies between symmetric sub-bands with respect to the Fermi level E_F are labeled as E_{11} and E_{22} .

of the anthracene unit. In the Supporting Information we also show other possible configurations.

The interaction of Li with the 7-AGNR leads to a complete electron transfer from Li to the nanoribbon. The experimentally observed doping level suggests that there are about 0.7 electrons per unit cell (one anthracene unit). Taking into account charge leakage to the metallic substrate commonly observed for graphene on metals,^[40] we can assume that the configuration with one Li atom per 7-AGNR unit cell is the most relevant to our experimental data. Moreover, Li atoms should be placed in the center with respect to long edges of the ribbon, otherwise the minimum of the conduction band is not located at the Γ -point of the BZ (see the Supporting Information), which is not observed in the experiment. The effective masses at the conduction band minima and valence band maxima for the configuration shown in Figure 3 are listed in Table 1. Let us compare the DFT results for the configurations with one Li atom in the center of the 7-AGNR unit cell (Figure 3b) to the ARPES data. Calculations show that the E_{11} and E_{22} transition energies follow opposite trends with doping: E_{11} decreases (by 0.19 eV) and E_{22} slightly

increases (by 0.05 eV). Qualitatively, the ARPES data are in agreement with the DFT results in that the Li doping is reducing the VB-CB separation. DFT calculations demonstrate electron–hole asymmetry in the effective masses: $m_{C_1}^*$ is 34% larger than m_{V_1} . This difference is increased by doping up to 55% in configuration with one Li atom. However, the experimentally observed difference is $\approx 400\%$ which is not captured by the DFT model. This leads to the partial occupation of the second C_2 sub-band in the DFT calculations, while in experiment all transferred charge is accepted by the heavier C_1 sub-band.

The experimentally observed large charge carrier mass can be attributed to many-body effects beyond the DFT approach. Indeed, the effective mass renormalization is determined by the energy and momentum dependence of the electron self-energy,^[41] which include many-body interactions such as electron–phonon and electron–electron coupling. Alkali-metal doping of graphene induces large electron–phonon coupling, which manifests itself by kinks in the linear band dispersion.^[42] In our case, the conduction band of doped GNRs is very shallow and does not allow us to make a statement regarding the degree of electron–phonon induced renormalization. Inclusion of the Coulomb interaction and its dynamical screening in the GW approach leads to an increase of the Fermi velocity in graphene^[43] and smaller (10%) effective electron masses for undoped 7-AGNRs.^[38] Thus, one can assume an increase of the effective mass due to the screened electron–electron interaction by the extra charge carriers in Li-doped system. Another contribution can be expected from the dynamical screening due to acoustic plasmons, which in theory can cause large effective mass renormalization in degenerately doped 1D semiconducting materials, as it was shown for carbon nanotubes.^[22] Since the electronic structure of nanotubes and nanoribbons is very similar to each other (both are obtained by zone folding

Table 1. DFT results for pristine and Li-doped 7-AGNRs with different amount of Li atoms per unit cell for configurations shown in Figure 3: effective masses of the first valence (V_1) and conduction (C_1) sub-bands, energies of E_{11} and E_{22} transitions.

	Pristine	With one Li atom	With two Li atoms
$m_{V_1}^* [m_e]^a$	0.41	0.4	0.39
$m_{C_1}^* [m_e]$	0.55	0.62	0.55
E_{11} [eV]	1.64	1.43	1.47
E_{22} [eV]	1.75	1.8	1.9

^{a)} m_e is the free electron mass.

of graphene), it is natural to expect that the quasiparticle renormalization of the band gap and effective mass due to the plasmon peaks in the loss function is leading to the same final result, that is, a reduced band gap and increased effective mass.

The semiconductor-to-metal transition should also affect the vibrational spectrum of 7-AGNRs. To investigate this effect we performed in situ Raman measurements of Li-doped GNRs in a specially built UHV Raman chamber. A commercially available Raman system was combined with an UHV setup where the GNR synthesis and Li doping have been performed as shown in a sketch in Figure 4a. The E_{22} optical transition energy for 7-AGNRs/Au(788) was experimentally found to be equal to 2.3 eV.^[44] We have taken advantage of the large optical response at the van Hove singularities to perform resonance Raman spectroscopy measurements with a 532 nm (≈ 2.33 eV) laser. The UHV Raman spectra of 7-AGNRs on Au(111) and Au(788) before and after deposition of Li are shown in Figure 4b. The amount of deposited Li was close to the maximum doping level in ARPES (Figure 1c). After Li doping, a reduction in the Raman intensity by a factor of ≈ 20 is observed. The unique combination of UHV Raman and ARPES measurements on identical samples allows us to elucidate the reason of the

observed Raman intensity loss. Looking to the ARPES spectrum of Figure 2b,c it is clear that the C_2 sub-band is not occupied and therefore the E_{22} transition is not blocked by the Pauli exclusion principle. Thus, there could be two reasons for the renormalization of the E_{22} optical transition energy. The first is a change in the QP band energies and the second is a reduction of the exciton binding energy. It was theoretically predicted that the dynamical screening effects induced in carbon nanotubes by a semiconductor-to-metal-transition substantially reduce the QP energy gap associated with the E_{22} transition; however, the decrease of the exciton binding energy is larger than the reduction of the QP gap making the effective optical gap larger.^[22] Since the excitonic effect is intrinsically large for ultra-narrow graphene nanoribbon of only several carbon atoms width,^[44] we expect a large renormalization of the optical transitions upon charge doping.

We note that the Raman modes of pristine ribbons on Au(788) are upshifted relative to the ribbons on Au(111) as a result of the higher density and hence larger inter-ribbon interaction (see STM data and assignment of the Raman modes in the Supporting Information). This situation is analogous to the upshift of the radial breathing mode in carbon nanotube bundles compared to isolated carbon nanotubes.^[45] Li doping seems to decrease the inter-ribbon interaction and results in Raman peaks for ribbons on Au(111) and Au(788) substrates that are very close to one another. Thus, to discuss the doping-induced phonon energy renormalization it is better to consider the system on Au(111).

For 7-AGNRs on Au(111) we observe the energy upshift for the G peak ≈ 4 cm^{-1} after Li doping while the D peak and the peak at 1260 cm^{-1} are downshifted by 3 cm^{-1} (the intensity of the peak at 1221 cm^{-1} is too weak to make a statement regarding its shift). Graphene at doping levels of 5×10^{13} electrons cm^{-2} or 0.013 electrons/atom (≈ 4 times smaller than in our case) exhibits much larger upshift of the G mode by ≈ 20 cm^{-1} .^[46,47] The reason is that graphene in its pristine state is a semimetal and the Kohn anomaly in the phonon dispersion at wavevector $q = \Gamma$ disappears with doping.^[46] Unlike graphene, ribbons are intrinsically semiconductors and do not exhibit a Kohn anomaly prior to doping. Upon doping we expect that a Kohn anomaly appears at $q_y = 2k_F$ (where k_F is the Fermi wavevector). Since for GNRs the mass renormalization is so strong, the conduction band becomes flat and the Fermi wavevector k_F rapidly moves away from the apex of the conduction band parabola. This shifts the $q_y = 2k_F$ phonon away from the BZ center and the Kohn anomaly does not affect Γ point phonons.

The present experimental Raman data are best rationalized using a similar reasoning as for doped semiconducting nanotubes. In semiconducting carbon nanotubes the total change in the phonon frequency of the G mode was rationalized in terms of dynamic and static contributions^[48]

$$\Delta\omega = \Delta\omega^{\text{static}} + \Delta\omega^{\text{dyn}} \quad (1)$$

The static term reflects the increase of the lattice constant resulting from the filling of antibonding states. This term is negative for electron doping and positive for hole doping.^[48,49] The dynamic contribution is always positive and occurs as a result of the reduced screening of the lattice vibration by the

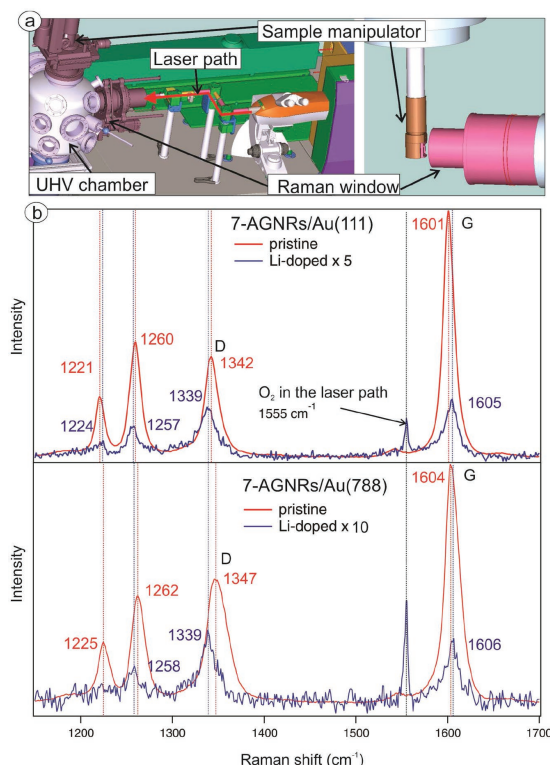


Figure 4. a) The UHV Raman system consists of a specially designed optical flange that connects a commercial Raman setup with an UHV system. The sample is mounted on a motorized manipulator. b) UHV Raman spectra of 7-AGNRs on Au(111) and on Au(788) measured before and after Li deposition with a 532 nm laser.

charge carriers. The dynamic effects describe changes beyond the adiabatic Born–Oppenheimer approximation.^[48,50–52] It depends on the electronic structure of the sp^2 carbon material, the phonon branch, and wavevector, and the doping level on which these competing factors prevail. In electron-doped semiconducting carbon nanotubes these two contributions balance each other, resulting in only a slight upshift of the G mode.^[48,52] Based on the structural similarity of nanotubes and nanoribbons we suppose the same for our system. In the Supporting Information we also estimated the Raman shift for the G mode of 7-AGNRs based on theory for graphene and nanotubes. A full quantitative agreement cannot be expected, since the C–C bond lengths in doped 7-AGNR are affected in an inhomogeneous manner. However, according to our DFT calculations the bond lengths of nanoribbons fall within less than 2% of the graphene bond length. We obtained that both contributions are the same order of magnitude and that the dynamic effects prevail. In regards to the downshift of the other phonon modes we ascribe this to the dominance of lattice expansion.

As a result of the relatively small phonon energy shifts upon electron doping (compared to graphene) we propose that for application of GNRs it is better not to use the Raman shifts but the intensity changes as an indicator of doping level. It can also be noted that one can expect much larger shift of the Raman modes of semiconducting GNRs for the hole doping as the dynamic and static terms have a positive sign. Thus, the electron/hole doping asymmetry in the Raman shifts for GNRs can be proposed to the future experimental studies.

In conclusion, we demonstrate that ultranarrow graphene nanoribbons are a new functional nanomaterial which can be effectively transformed from a wide-gap semiconductor into a metal via controlled lithium doping. We observe changes in the electron and phonon systems in 7-AGNRs upon lithium deposition using ARPES and UHV–Raman techniques. Electron transfer from lithium allows us to reach heavily doped regime (0.05 electrons/atom) and obtain the first direct proof of a combined band gap reduction by ≈ 0.3 eV and giant (supposed by a factor of four) effective mass renormalization in 1D system. These effects will be important for future graphene nanoelectronic devices utilizing the transport and optical properties of graphene nanoribbons. The combined investigation of the electron and phonon structures allowed us to explain the Raman shifts in electron-doped GNRs by the setting impact of the lattice relaxation and dynamic effects. The observed Raman intensity decrease upon doping is attributed to the changes in the quasiparticle dispersion and exciton binding energy. We propose GNRs as a unique platform for combined experimental and theoretical studies embracing many-body interactions. Our findings have relevance for the large 1D materials community and it lays the foundations for further studies of doped graphene nanoribbons.

Experimental Section

Experimental Details: 7-AGNRs were synthesized by surface polymerization of 10,10-dibromo-9,9-bianthryl (DBBA) molecules^[13] on Au(111) and Au(788) surfaces. Au substrates were cleaned by three cycles of Ar⁺ sputtering (800 V) and subsequent annealing at 500 °C. The clean surface of Au(788) is shown in the Supporting Information. DBBA

molecules were evaporated from a quartz crucible using a homebuilt evaporator with a thermocouple attached to the molecule reservoir. The deposition rate was controlled using a quartz microbalance. About 8 Å of precursor molecules (using the graphite density and Z-factor) were evaporated onto the Au surface which was kept at room temperature. Hereafter, a two-step polymerization reaction was performed: a 200 °C annealing step followed by a 400 °C annealing step, which induce debromination and cyclodehydrogenation reactions, respectively. The annealing was carried out using a computer controlled ramp that increased temperature over several hours. Lithium deposition (from 1 to 3 monolayers) was performed separately for ARPES, NEXAFS, and UHV Raman measurements using commercial SAES getters, calibrated with quartz microbalance. The maximum Li coverage was identical for all methods. The sample was kept at 80 K for ARPES measurements and at room temperature for other studies.

ARPES was carried out at the I3 beamline of the MAX IV synchrotron radiation facility (Lund, Sweden) using a Scienta R-4000 hemispherical electron analyser. The ARPES spectra were measured using photon energy of 32 eV in the second BZ of the GNRs and shifted back by application of the reciprocal lattice vector to the first BZ. The samples for ARPES measurements were synthesized and checked in the UHV Raman chamber and then transferred under UHV conditions into a special container which was filled then to a slight overpressure (1.1 bar) by high-purity Ar gas. Samples in UHV tight vacuum suitcases filled with an Ar were transported to the load-lock chamber of the ARPES beamline endstation and later gently annealed (at 200 °C) under UHV conditions. This method allowed us to achieve reproducible experimental results. For determination of the parabola maxima and the effective masses we performed a parabolic fit to the experimental energy distribution curve (EDC) maxima. The fits were performed within a region of sufficient signal/background ratio and hence have different wavevector limits. The physical origins for the wavevector dependence of the photoemission signal are the matrix elements and the overlap with Au states.

The STM data of clean Au(788) and 7-AGNRs/Au(788) are shown in the Supporting Information. STM measurements were performed using an Omicron LT-STM with the samples held at 4.5 K in UHV. A tungsten tip was used for topography and spectroscopic measurements. Prior to performing STS on the fully GNR covered Au(788), we prepared the tip on a clean Au(111) surface until we obtained pristine Au background spectra. This tip was then used for measurements on Au(788) and afterward checked again on clean Au(111) to ensure the tip did not change during measurements. Topographic images were acquired in constant current mode. dI/dV spectra were obtained using the lock-in technique where the tip bias was modulated by a 457 Hz, 10 mV (rms) sinusoidal voltage under open-feedback conditions. All STM images were processed with WSxM.^[53]

UHV–Raman was performed in the back-scattering geometry using commercial Raman systems (Renishaw and OceanOptics) integrated in a homebuilt optical chamber where the exciting and Raman scattered light were coupled into the vacuum using a long-working distance microscope objective with an NA of ≈ 0.4 . The laser power on the sample was kept below 1 mW. The analysis chamber of the UHV–Raman was attached to another chamber for sample preparation where the 7-AGNR synthesis, LEED characterization, and Li deposition were performed. Raman spectra were calibrated using Si peak at 520.5 cm^{-1} as well as oxygen peak at 1555 cm^{-1} .

XPS and NEXAFS experiments were performed at the German-Russian beamline (RGL) of the HZB BESSY II synchrotron radiation facility (Berlin, Germany). XPS spectra were measured with photon energy of 320 eV and pass energy of 10 eV in the normal emission geometry. Samples were synthesized in the UHV Raman system and transferred to the synchrotron in the same manner as described for ARPES measurements. XPS data indicated no trace of oxygen as confirmed by the absence of an O1s peak (see survey spectrum in the Supporting Information). All XPS spectra were calibrated using the Au 4f_{7/2} core level at a binding energy 84.0 eV. NEXAFS data were obtained in total electron yield mode with an energy resolution of 50 meV close to the C K-edge.

Computational Details: Our first-principles calculations have been performed in the framework of the density functional theory^[54] by using pseudopotentials obtained by the projector augmented wave method^[55] and the Perdew–Burke–Ernzerhof exchange–correlation energy functional^[56] as implemented in the Vienna ab initio simulation package code.^[57,58] The ground-state adsorption geometry of Li on the C₁₄H₄ nanoribbon was obtained for an energy cutoff of 500 eV and by including the van der Waals interactions with the help of the nonlocal correlation energy functional vdW-DF2^[59] together with the exchange energy functional developed by Hamada.^[60]

Supporting Information

Supporting Information is available from the Wiley Online Library or from the author.

Acknowledgements

B.S., A.F., M.H., and A.G. acknowledge the ERC Grant No. 648589 “SUPER-2D,” support from the DFG through the CRC1238 (project A1) and DFG project GR 3708/2-1. N.I.V. acknowledges the Russian Science Foundation (No. 14-13-00747). This research was supported by the U.S. Department of Energy (DOE), Office of Science, Basic Energy Sciences (BES), under Award No. DE-SC0010409 (design, synthesis, and characterization of molecular building blocks) and the Center for Energy Efficient Electronics Science NSF Award No. 0939514 (SPM imaging and spectroscopy). K.S. and A.P. acknowledge support from the Swedish Research Council and the ERC Grant No. 321319.

Received: November 11, 2016

Revised: December 23, 2016

Published online: March 10, 2017

- [1] X. Li, X. Wang, L. Zhang, S. Lee, H. Dai, *Science* **2008**, 319, 1229.
- [2] F. Schwierz, *Nat. Nanotechnol.* **2010**, 5, 487496.
- [3] Z. Chen, Y.-M. Lin, M. J. Rooks, P. Avouris, *Physica E* **2007**, 40, 228.
- [4] X. Wang, Y. Ouyang, X. Li, H. Wang, J. Guo, H. Dai, *Phys. Rev. Lett.* **2008**, 100, 206803.
- [5] L. Liao, J. Bai, R. Cheng, Y.-C. Lin, S. Jiang, Y. Huang, X. Duan, *Nano Lett.* **2010**, 10, 1917.
- [6] K. Nakada, M. Fujita, G. Dresselhaus, M. S. Dresselhaus, *Phys. Rev. B* **1996**, 54, 17954.
- [7] L. Yang, L. C.-H. Park, Y.-W. Son, M. L. Cohen, S. G. Louie, *Phys. Rev. Lett.* **2007**, 99, 186801.
- [8] M. Y. Han, B. Ozyilmaz, Y. Zhang, P. Kim, *Phys. Rev. Lett.* **2007**, 98, 206805.
- [9] V. Barone, O. Hod, G. E. Scuseria, *Nano Lett.* **2006**, 6, 2748.
- [10] K. Wakabayashi, K.-I. Sasaki, T. Nakanishi, T. Enoki, *Sci. Technol. Adv. Mater.* **2010**, 11, 054504.
- [11] J. R. Sanchez-Valencia, T. Dienel, O. Gröning, I. Shorubalko, A. Mueller, M. Jansen, K. Amsharov, P. Ruffieux, R. Fasel, *Nature* **2014**, 512, 61.
- [12] L. Grill, M. Dyer, L. Laffrentz, M. Persson, M. V. Peters, S. Hecht, *Nat. Nanotechnol.* **2007**, 2, 687.
- [13] J. Cai, P. Ruffieux, R. Jaafar, M. Bieri, T. Braun, S. Blankenburg, M. Muoth, A. P. Seitsonen, M. Saleh, X. Feng, K. Müllen, R. Fasel, *Nature* **2010**, 466, 470.
- [14] Y.-C. Chen, D. G. de Oteyza, Z. Pedramrazi, C. Chen, F. R. Fischer, M. F. Crommie, *ACS Nano* **2013**, 7, 6123.
- [15] Y.-C. Chen, T. Cao, C. Chen, Z. Pedramrazi, D. Haberer, D. G. de Oteyza, F. R. Fischer, M. Crommie, *Nat. Nanotechnol.* **2015**, 10, 156.
- [16] R. R. Cloke, T. Marangoni, G. D. Nguyen, T. Joshi, D. J. Rizzo, C. Bronner, T. Cao, S. G. Louie, M. F. Crommie, F. R. Fischer, *J. Am. Chem. Soc.* **2015**, 137, 8872.
- [17] S. Kawai, S. Saito, S. Osumi, S. Yamaguchi, A. S. Foster, P. Spijker, E. Meyer, *Nat. Commun.* **2015**, 6, 8098.
- [18] A. Kimouche, M. M. Ervasti, R. Drost, S. Halonen, A. Harju, P. M. Joensuu, J. Sainio, P. Liljeroth, *Nat. Commun.* **2015**, 6, 10177.
- [19] P. Ruffieux, S. Wang, B. Yang, C. Sánchez-Sánchez, J. Liu, T. Dienel, L. Talirz, P. Shinde, C. A. Pignedoli, D. Passerone, T. Dumsila, X. Feng, K. Müllen, R. Fasel, *Nature* **2016**, 531, 489492.
- [20] L. Talirz, P. Ruffieux, R. Fasel, *Adv. Mater.* **2016**, 28, 6222.
- [21] S. Das Sarma, D. W. Wang, *Phys. Rev. Lett.* **2000**, 84, 2010.
- [22] C. D. Spataru, F. Léonard, *Phys. Rev. Lett.* **2010**, 104, 177402.
- [23] S. Gao, Y. Liang, C. D. Spataru, L. Yang, *Nano Lett.* **2016**, 16, 5568.
- [24] D. Prezzi, D. Varsano, A. Ruini, A. Marini, E. Molinari, *Phys. Rev. B* **2008**, 77, 041404.
- [25] D. Prezzi, D. Varsano, A. Ruini, E. Molinari, *Phys. Rev. B* **2011**, 84, 041401.
- [26] P. Ruffieux, J. Cai, N. C. Plumb, L. Patthey, D. Prezzi, A. Ferretti, E. Molinari, X. Feng, K. Müllen, C. A. Pignedoli, R. Fasel, *ACS Nano* **2012**, 6, 6930.
- [27] J. U. Lee, *Phys. Rev. B* **2007**, 75, 075409.
- [28] M. Steiner, M. Freitag, V. Perebeinos, A. Naumov, J. P. Small, A. A. Bol, P. Avouris, *Nano Lett.* **2009**, 9, 3477.
- [29] H. Hartleb, F. Späth, T. Hertel, *ACS Nano* **2015**, 9, 10461.
- [30] Y. Miyauchi, Z. Zhang, M. Takekoshi, Y. Tomio, H. Suzuura, V. Perebeinos, V. V. Deshpande, C. Lu, S. Berciaud, P. Kim, J. Hone, T. F. Heinz, *Phys. Rev. B* **2015**, 92, 205407.
- [31] S. Linden, D. Zhong, A. Timmer, N. Aghdassi, J. H. Franke, H. Zhang, X. Feng, K. Müllen, H. Fuchs, L. Chi, H. Zacharias, *Phys. Rev. Lett.* **2012**, 108, 216801.
- [32] M. Koch, F. Ample, C. Joachim, L. Grill, *Nat. Nanotechnol.* **2012**, 7, 713.
- [33] H. Söde, L. Talirz, O. Gröning, C. A. Pignedoli, R. Berger, X. Feng, K. Müllen, R. Fasel, P. Ruffieux, *Phys. Rev. B* **2015**, 91, 045429.
- [34] G. Vasseur, Y. Fagot-Revurat, M. Sicot, B. Kierren, L. Moreau, D. Malterre, L. Gardenas, G. Galeotti, J. Lipton-Duffin, F. Rosei, M. Di Giovannantonio, G. Contini, P. Le Fevre, F. Bertran, L. Liang, V. Meunier, D. F. Perepichka, *Nat. Commun.* **2016**, 7, 10235.
- [35] M. M. Ugeda, A. J. Bradley, S.-F. Shi, F. H. da Jornada, Y. Zhang, D. Y. Qiu, W. Ruan, S.-K. Mo, Z. Hussain, Z.-X. Shen, F. Wang, S. G. Louie, M. F. Crommie, *Nat. Mater.* **2014**, 13, 1091.
- [36] M. Ezawa, *Phys. Rev. B* **2006**, 73, 045432.
- [37] Y.-W. Son, M. L. Cohen, S. G. Louie, *Phys. Rev. Lett.* **2006**, 97, 216803.
- [38] S. Wang, L. Talirz, C. A. Pignedoli, X. Feng, R. F. Klaus Müllen, P. Ruffieux, *Nat. Commun.* **2016**, 7, 11507.
- [39] K. A. Simonov, N. A. Vinogradov, A. S. Vinogradov, A. V. Generalov, E. M. Zagrebina, N. Mårtensson, A. A. Cafolla, T. Carpy, J. P. Cuniffe, A. B. Preobrajenski, *J. Phys. Chem. C* **2014**, 118, 12532.
- [40] N. I. Verbitskiy, A. V. Fedorov, C. Tresca, G. Profeta, L. Petaccia, B. V. Senkovskiy, D. Y. Usachov, D. V. Vyalikh, L. V. Yashina, A. A. Eliseev, T. Pichler, A. Grüneis, *2D Mater.* **2016**, 3, 045003.
- [41] J. W. Negele, H. Orland, *Quantum Many-Particle Systems*, Advanced Books Classics, Westview, Boulder, CO **1998**.
- [42] A. V. Fedorov, N. I. Verbitskiy, D. Haberer, C. Struzzi, L. Petaccia, D. Usachov, O. Y. Vilkov, D. V. Vyalikh, J. Fink, M. Knupfer, B. Büchner, A. Grüneis, *Nat. Commun.* **2014**, 5, 4257.
- [43] P. E. Trevisanuto, C. Giorgetti, L. Reining, M. Ladisa, V. Olevano, *Phys. Rev. Lett.* **2008**, 101, 226405.
- [44] R. Denk, M. Hohage, P. Zeppenfeld, J. Cai, C. A. Pignedoli, H. Söde, R. Fasel, X. Feng, K. Müllen, S. Wang, D. Prezzi, A. Ferretti, A. Ruini, E. Molinari, P. Ruffieux, *Nat. Commun.* **2014**, 5, 4253.

**ADVANCED
ELECTRONIC
MATERIALS**

www.advelectronicmat.de

**ADVANCED
SCIENCE NEWS**

www.advancedsciencenews.com

- [45] H. Kuzmany, W. Plank, M. Hulman, C. Kramberger, A. Grüneis, T. Pichler, H. Peterlik, H. Kataura, Y. Achiba, *Eur. Phys. J. B* **2001**, 22, 307.
- [46] A. Das, S. Pisana, B. Chakraborty, S. Piscanec, S. K. Saha, U. V. Waghmare, K. S. Novoselov, H. R. Krishnamurthy, A. K. Geim, A. C. Ferrari, A. K. Sood, *Nat. Nanotechnol.* **2008**, 3, 210.
- [47] J. Yan, Y. Zhang, P. Kim, A. Pinczuk, *Phys. Rev. Lett.* **2007**, 98, 166802.
- [48] A. Das, A. K. Sood, *Phys. Rev. B* **2009**, 79, 235429.
- [49] B. Chakraborty, A. Bera, D. V. S. Muthu, S. Bhowmick, U. V. Waghmare, A. K. Sood, *Phys. Rev. B* **2012**, 85, 161403.
- [50] S. Pisana, M. Lazzeri, C. Casiraghi, K. Novoselov, A. Geim, A. Ferrari, F. Mauri, *Nat. Mater.* **2007**, 6, 198.
- [51] N. Caudal, A. M. Saitta, M. Lazzeri, F. Mauri, *Phys. Rev. B* **2007**, 75, 115423.
- [52] J. C. Tsang, M. Freitag, V. Perebeinos, J. Liu, P. Avouris, *Nat. Nanotechnol.* **2007**, 2, 725.
- [53] I. Horcas, R. Fernandez, J. Gomez-Rodriguez, J. Colchero, J. Gomez-Herrero, A. Baro, *Rev. Sci. Instrum.* **2007**, 78, 013705.
- [54] W. Kohn, L. J. Sham, *Phys. Rev.* **1965**, 140, A1133.
- [55] P. E. Blöchl, *Phys. Rev. B* **1994**, 50, 17953.
- [56] J. Perdew, K. Burke, M. Ernzerhof, *Phys. Rev. Lett.* **1996**, 77, 3865.
- [57] G. Kresse, J. Hafner, *Phys. Rev. B* **1993**, 47, 558.
- [58] G. Kresse, J. Furthmüller, *Phys. Rev. B* **1996**, 54, 11169.
- [59] K. Lee, E. D. Murray, L. Kong, B. I. Lundqvist, D. C. Langreth, *Phys. Rev. B* **2010**, 82, 081101.
- [60] I. Hamada, *Phys. Rev. B* **2014**, 89, 121103.

Bibliography

- [1] J. Chapman, Y. Su, C. A. Howard, D. Kundys, A. N. Grigorenko, F. Guinea, A. K. Geim, I. V. Grigorieva, R. R. Nair, *Scientific Reports* **Mar. 2016**, *6*, DOI 10.1038/srep23254.
- [2] S. Ichinokura, K. Sugawara, A. Takayama, T. Takahashi, S. Hasegawa, *ACS Nano* **Jan. 2016**, *10*, 2761–2765.
- [3] G. Profeta, M. Calandra, F. Mauri, *Nature Physics* **Jan. 2012**, *8*, 131–134.
- [4] U. Fano, *Physical Review* **Dec. 1961**, *124*, 1866–1878.
- [5] S. Piscanec, M. Lazzeri, F. Mauri, A. C. Ferrari, J. Robertson, *Physical Review Letters* **Oct. 2004**, *93*, DOI 10.1103/physrevlett.93.185503.
- [6] M. Lazzeri, F. Mauri, *Physical Review Letters* **Dec. 2006**, *97*, DOI 10.1103/physrevlett.97.266407.
- [7] K. Verguts, K. Schouteden, C.-H. Wu, L. Peters, N. Vrancken, X. Wu, Z. Li, M. Erkens, C. Porret, C. Huyghebaert, et al., *ACS Applied Materials and Interfaces* **Oct. 2017**, *9*, 37484–37492.
- [8] A. H. C. Neto, F. Guinea, N. M. R. Peres, K. S. Novoselov, A. K. Geim, *Reviews of Modern Physics* **Jan. 2009**, *81*, 109–162.
- [9] J. L. McChesney, A. Bostwick, T. Ohta, T. Seyller, K. Horn, J. González, E. Rotenberg, *Phys. Rev. Lett.* **Apr. 2010**, *104*, 136803.
- [10] I. M. LIFSHITZ, *Soviet Physics Jetp* **Nov. 1960**, *11*.
- [11] A. Varlet, M. Mucha-Kruczyński, D. Bischoff, P. Simonet, T. Taniguchi, K. Watanabe, V. Fal’ko, T. Ihn, K. Ensslin, *Synthetic Metals* **Dec. 2015**, *210*, 19–31.

- [12] Y. Henmi, H. P. O. Collado, K. Nogajewski, M. R. Molas, G. Usaj, C. A. Balseiro, M. Orlita, M. Potemski, C. Faugeras, *Nano Letters* **May 2016**, *16*, 3710–3716.
- [13] D. Pierucci, H. Sediri, M. Hajlaoui, J.-C. Girard, T. Brumme, M. Calandra, E. Velez-Fort, G. Patriarche, M. G. Silly, G. Ferro, V. Soulière, M. Marangolo, F. Sirotti, F. Mauri, A. Ouerghi, *ACS Nano* **Apr. 2015**, *9*, 5432–5439.
- [14] B. Pamuk, J. Baima, F. Mauri, M. Calandra, *Physical Review B* **Feb. 2017**, *95*, DOI 10.1103/physrevb.95.075422.
- [15] H. Henck, J. Avila, Z. B. Aziza, D. Pierucci, J. Baima, B. Pamuk, J. Chaste, D. Utt, M. Bartos, K. Nogajewski, B. A. Piot, M. Orlita, M. Potemski, M. Calandra, M. C. Asensio, F. Mauri, C. Faugeras, A. Ouerghi, *Physical Review B* **June 2018**, *97*, DOI 10.1103/physrevb.97.245421.
- [16] Y. Cao, V. Fatemi, S. Fang, K. Watanabe, T. Taniguchi, E. Kaxiras, P. Jarillo-Herrero, *Nature* **Mar. 2018**, *556*, 43–50.
- [17] R. Bistritzer, A. H. MacDonald, *Proceedings of the National Academy of Sciences* **July 2011**, *108*, 12233–12237.
- [18] J. L. McChesney, A. Bostwick, T. Ohta, T. Seyller, K. Horn, J. González, E. Rotenberg, *Physical Review Letters* **Apr. 2010**, *104*, DOI 10.1103/physrevlett.104.136803.
- [19] M. S. Dresselhaus, G. Dresselhaus, *Advances in Physics* **Jan. 2002**, *51*, 1–186.
- [20] J. Kleeman, K. Sugawara, T. Sato, T. Takahashi, *Journal of Physics: Condensed Matter* **Apr. 2016**, *28*, 204001.
- [21] H. Hertz, *Annalen der Physik und Chemie* **1887**, *267*, 983–1000.
- [22] A. Einstein, *Annalen der Physik* **1905**, *322*, 132–148.
- [23] Saiht, *Wikipedia* **2009**.
- [24] A. Damascelli, *Physica Scripta* **2004**, *T109*, 61.
- [25] www.eucall.eu.

- [26] *Industrial Applications of Laser Remote Sensing*, (Eds.: T. Fukuchi, T. Shiina), BENTHAM, **Apr. 2012**.
- [27] R. Vidano, D. Fischbach, L. Willis, T. Loehr, *Solid State Communications* **July 1981**, *39*, 341–344.
- [28] F. Tuinstra, J. L. Koenig, *The Journal of Chemical Physics* **Aug. 1970**, *53*, 1126–1130.
- [29] L. M. Malard, J. Nilsson, D. C. Elias, J. C. Brant, F. Plentz, E. S. Alves, A. H. C. Neto, M. A. Pimenta, *Physical Review B* **Nov. 2007**, *76*, DOI 10.1103/physrevb.76.201401.
- [30] D. L. Mafra, G. Samsonidze, L. M. Malard, D. C. Elias, J. C. Brant, F. Plentz, E. S. Alves, M. A. Pimenta, *Physical Review B* **Dec. 2007**, *76*, DOI 10.1103/physrevb.76.233407.
- [31] M. Dresselhaus, A. Jorio, R. Saito, *Annual Review of Condensed Matter Physics* **Aug. 2010**, *1*, 89–108.
- [32] P. C. Eklund, K. R. Subbaswamy, *Physical Review B* **Dec. 1979**, *20*, 5157–5161.
- [33] S. D. M. Brown, A. Jorio, P. Corio, M. S. Dresselhaus, G. Dresselhaus, R. Saito, K. Kneipp, *Physical Review B* **Mar. 2001**, *63*, DOI 10.1103/physrevb.63.155414.
- [34] H. Farhat, S. Berciaud, M. Kalbac, R. Saito, T. F. Heinz, M. S. Dresselhaus, J. Kong, *Physical Review Letters* **Oct. 2011**, *107*, DOI 10.1103/physrevlett.107.157401.
- [35] I. Miccoli, F. Edler, H. Pfnür, C. Tegenkamp, *Journal of Physics: Condensed Matter* **May 2015**, *27*, 223201.
- [36] W. Versnel, *Solid-State Electronics* **Nov. 1979**, *22*, 911–914.
- [37] J. Robertson, *The European Physical Journal Applied Physics* **Dec. 2004**, *28*, 265–291.
- [38] M. G. Hell, N. Ehlen, B. V. Senkovskiy, E. H. Hasdeo, A. Fedorov, D. Dombrowski, C. Busse, T. Michely, G. di Santo, L. Petaccia, R. Saito, A. Grüneis, *Nano Letters* **Aug. 2018**, *18*, 6045–6056.

- [39] N. Ehlen, M. Hell, G. Marini, E. Hasdeo, R. Saito, Y. Falke, G. D. Santo, L. Petaccia, G. Profeta, A. Grüneis, *submitted* **May 2019**.
- [40] M. G. Hell, Y. Falke, A. Bliesener, N. Ehlen, B. V. Senkovskiy, T. Szkopek, A. Grüneis, *physica status solidi (b)* **Nov. 2018**, 255, 1800456.

Abstract

We used ultra-high vacuum (UHV) Raman spectroscopy in tandem with angle-resolved photoemission (ARPES) to investigate the doping-dependent Raman spectrum of epitaxially grown graphene. The evolution of the Raman spectra from pristine to heavily Cs doped graphene up to a carrier concentration of $4.4 \times 10^{14} \text{ cm}^{-2}$ was investigated [38]. Renormalization effects reduce the electronic bandwidth at this doping level when graphene is at the onset of the Lifshitz transition. Ultraviolet (UV) light allows to probe the optical transition at the saddle point in the Brillouin zone achieving resonance Raman conditions in close vicinity to the van Hove singularity in the joint density of states. The position of the Raman G band of fully doped graphene/Ir(111) shifted down by 60 cm^{-1} and the G band asymmetry of Cs doped epitaxial graphene on Ir(111) assumed an unusual strong Fano asymmetry [4] opposite to that of the G band of doped graphene on insulators. A fully experimental relation between energy shift and Fano asymmetry parameter of the Raman G band versus carrier concentration obtained by ARPES was found by using the sum of static (lattice expansion) and dynamic (electron-phonon coupling) effects [6].

By sandwiching a graphene monolayer in between two Cs layers with a 2×2 and $\sqrt{3} \times \sqrt{3}$ structures, a new method for inducing a flat band [18] in graphene was established. The obtained trilayer system was investigated by ARPES, revealing a flat electron energy dispersion at the Fermi level and a partially occupied alkali metal s band. The occurrence of these two features together has proven impossible to achieve so far despite their importance for achieving superconductivity in graphene. We could explain the origin of the doping induced flat band at the M point of the Brillouin zone by zone folding and

hybridization of the graphene bands with the partially filled alkali metal band [39].

Finally we performed a simultaneous sample characterization by Raman spectroscopy and electronic transport in ultra-high vacuum at low temperatures. The characterization prior to the transfer included electron diffraction, photoemission spectroscopy and Raman spectroscopy using ultraviolet excitation. The transfer of graphene was carried out using a water-promoted electrochemical bubbling technique [7] which was applied to graphene/Ir(111) for the first time. Following the transfer procedure, the graphene layer was electrically contacted and mounted onto a special sample carrier. This carrier allows for combined Raman and transport measurements inside the UHV system. UHV Raman mapping revealed a large area homogeneous graphene quality over several mm^2 . We probed UHV electronic transport during alkali metal deposition. Our work demonstrates high sensitivity towards sensing of alkali atoms and a giant decrease of the four-point resistance by three orders of magnitude upon Cs doping [40].

Zusammenfassung

Wir nutzen Raman-Spektroskopie im Ultrahochvakuum (UHV) gemeinsam mit winkelaufgelöster Photoelektronenspektroskopie (ARPES) um die Dotierungsabhängigkeit des Raman-Spektrums epitaktisch gewachsenen Graphens zu untersuchen. Die Entwicklung des Raman-Spektrums von pristinem, bis zu schwer mit Cd dotiertem Graphen mit einer Ladungsträgerkonzentration von $4.4 \times 10^{14} \text{ cm}^{-2}$ wurde beobachtet [38]. Renormalisierungseffekte reduzieren bei diesem Dotierungslevel die elektronische Bandweite, wenn sich Graphen am Anfang eines Lifshitz-Übergangs befindet. Ultraviolette (UV) Licht erlaubt die Untersuchung des optischen Übergangs am Sattelpunkt in der Brillouin-Zone, was zu resonanten Raman-Bedingungen in der Nähe der van Hove Singularität der Zustandsdichte führt. Die Position der Raman G Mode des vollständig dotierten Graphen/Ir(111) ändert sich um 60 cm^{-1} , wobei das G band des Cs dotiertem Graphens auf Ir(111) eine ungewöhnlich starke und umgekehrte Fano Asymmetrie [4] im Vergleich zum G Band von Graphen auf Nichtleitern aufweist. Wir fanden eine vollständige experimentelle Beschreibung der Relation zwischen der Energieverschiebung und der Fano Asymmetrie des Raman G Bandes gegenüber der Ladungsträgerkonzentration, die mit ARPES bestimmt wurde. Hierbei wurde die Summe aus statischen (Gitterexpansion) und dynamischen (Elektron-Phonon-Kopplung) Effekten berücksichtigt [6].

Die Einbettung einer Monolage Graphen zwischen zwei Schichten Cs mit 2×2 und $\sqrt{3} \times \sqrt{3}$ Struktur, stellt eine neuartige Methode dar, um ein flaches Band [18] in Graphen herbeizuführen. Die vorliegende Trilage wies bei der Untersuchung mit ARPES eine flache Energie-Dispersion an der Fermikante und

ein teilweise gefülltes Alkalimetall s-Band auf. Die Beobachtung dieser beiden Merkmale zugleich war bislang nicht gelungen, trotz deren Bedeutung für die Realisierung von Supraleitung in Graphen. Wir konnten die Ursache, des durch Dotierung erzeugten flachen Bandes am M Punkt der Brillouin-zone, durch Zonenfaltung und Hybridisierung von Graphenbändern mit einem teilweise gefüllten Alkalimetallband erklären [39].

Letzlich führten wir simultane Charakterisierungen mit Raman-Spektroskopie und elektrischen Transportmessungen im Ultrahochvakuum bei niedrigen Temperaturen aus. Die Untersuchungen vor dem Transfer von Graphen beinhalteten niederenergetische Elektronenbeugung, Photoemissionsspektroskopie und Raman-Spektroskopie mit ultravioletttem Licht. Der Transfer von Graphen wurde mit einer wasserunterstützten "bubbling"-Methode [7] durchgeführt, die zum ersten Mal Anwendung bezüglich Graphene auf Ir(111) fand. Nach dem Transfer wurde das Graphen mit elektrischen Kontakten versehen und auf einen speziellen Probenhalter aufgebracht. Der Probenhalter erlaubt die kombinierte Untersuchung mit Raman-Spektroskopie und elektrischen Transport innerhalb der Ultrahochvakuumkammer. Flächendeckende UHV Raman Messungen zeigten eine hohe Homogenität über mehrere mm^2 . Die elektrischen Transportmessungen wurden auch unter Einfluss Alkalimetallen durchgeführt. Unsere Arbeit zeigt hierbei die hohe Sensitivität bezüglich des Einflusses von Alkalimetallatomen und einen enormen Abfall des Vier-Punkt-Widerstandes im Bereich von drei Größenordnungen bei Dotierung mit Cs [40].

Own contributions to publications

The following lists the experimental contribution of the author to the publication.

RESONANCE RAMAN SPECTRUM OF DOPED EPITAXIAL GRAPHENE AT THE LIFSHITZ TRANSITION

In "Resonance Raman spectrum of doped epitaxial graphene at the Lifshitz transition" the author was responsible for the synthesis and functionalization of the graphene samples. For UHV Raman measurements he implemented a UV laser in UHV and took over the complete Raman measurements including the data evaluation. ARPES measurements and the corresponding data evaluation was taken out with assistance.

ORIGIN OF THE FLAT BAND IN HEAVILY CS DOPED GRAPHENE

For the publication "Joint occurrence of a flat band and a partially filled interlayer band in graphene doped beyond the Lifshitz transition" the author created the graphene samples and guaranteed the desired functionalization. Raman measurements and the required data evaluation was taken out by the author. ARPES measurements and the corresponding data evaluation was taken out with assistance.

COMBINED ULTRA HIGH VACUUM RAMAN AND ELECTRONIC TRANSPORT CHARACTERIZATION OF LARGE-AREA GRAPHENE ON SiO₂

The publication "Combined ultra high vacuum Raman and electronic transport characterization of large-area graphene on SiO₂" describes a long term period of the authors work. He was responsible for the sample production

from the synthesis of graphene on Ir(111) to a working transistor including the bubbling transfer and the assembly of contacts to graphene on SiO₂. Therefore he designed a unique spring pin supported UHV tool for electric transport measurements. The software for controlling the electric measurements was designed with assistance. Raman, LEED, XPS, NEXAFS and electric measurements including the data evaluation were taken out by the author.

FACILE PREPARATION OF AU(111)/MICA SUBSTRATES FOR HIGH-QUALITY GRAPHENE NANORIBBON SYNTHESIS

All the experiments in "Facile preparation of au(111)/mica substrates for high-quality graphene nanoribbon synthesis" were already conducted in the authors Diploma thesis. The author was responsible the the construction of the growth setup including the design and assembling. He was also in charge of the sample production which implicated the concept of a working receipt for Au(111) substrate growth and the synthesis of GNR. The measurements of LEED, XPS, NEXAFS and Raman were taken out independent in Cologne and at the HESGM beamline of Bessy II Berlin.

Selbständigkeitserklärung

Ich versichere, dass ich die von mir vorgelegte Dissertation selbständig angefertigt, die benutzten Quellen und Hilfsmittel vollständig angegeben und die Stellen der Arbeit einschließlich Tabellen, Karten und Abbildungen, die anderen Werken im Wortlaut oder dem Sinn nach entnommen sind, in jedem Einzelfall als Entlehnung kenntlich gemacht habe; dass diese Dissertation noch keiner anderen Fakultät oder Universität zur Prüfung vorgelegen hat; dass sie abgesehen von unten angegebenen Teilpublikationen noch nicht veröffentlicht worden ist, sowie, dass ich eine solche Veröffentlichung vor Abschluss des Promotionsverfahrens nicht vornehmen werde. Die Bestimmungen der Promotionsordnung sind mir bekannt. Die von mir vorgelegte Dissertation ist von Prof. Dr. Alexander Grüneis betreut worden.

Köln 16.07.2019

Martin G. Hell

